UNIVERSITÀ
DEGLI STUDI
FIRENZE

Scuola di Scienze Matematiche Fisiche e Naturali

Corso di Laurea Magistrale in Scienze Fisiche e Astrofisiche (LM-17)

Sviluppo di tecniche di *Optical Tweezers* con deflettori acusto ottici per simulatori quantistici atomici.

Development of Optical Tweezer techniques with Acousto Optic Deflectors for atomic quantum simulators.

Relatore
Dr. **Giacomo Cappellini**

Correlatore
Prof. **Leonardo Fallani**

Candidato
Luca Guariento

Anno accademico 2020-2021

Contents

Chapter 1

Introduction to quantum simulation

Quantum simulators are special experimental platforms that are capable of reproducing a Hamiltonian, or a class of Hamiltonians that describe a particular physical system, in a controllable apparatus. Such devices offer the possibility to simulate in synthetic systems many-body physics problems that can be often very difficult to solve exactly and for which only approximate solutions, if any, exist. Difficulties arise in particular when systems composed of many interacting quantum objects are considered and a prediction of the evolution of the system based on microscopical properties is almost impossible. Since the dimensionality of the Hilbert space describing a many-body system increases exponentially as a function of the number of quantum objects, a simulation of the evolution of the system shows non-manageable computational complexity. The problem can be tackled using a quantum simulator where the desired problem is mapped onto. This realizes the idea of R. Feynman of a quantum simulator [1], a quantum system that is used to simulate the evolution of another physical system. The advantage of synthetic simulators is that they offer a high degree of control of the experimental parameters which is not accessible in a real system, paving the way to a more complete study of phenomena of interest. In this context, plenty of different platforms showed up in the past decades [2, 3].

Among these platforms, two quantum simulators were particularly successful in the last years: degenerate quantum gases in optical lattices [4, 5] and trapped ions [6, 7]. Degenerate quantum gases trapped in optical lattices constitute a very suitable platform for the study of many-body systems. Typically, samples composed of up to a few million atoms can be prepared and manipulated. The advantage of this kind of platform is indeed its scalability on the number of particles which allows for the investigation of many-body interacting systems and collective properties, and for the study of the behaviour of quantum matter under extreme quantum degeneracy regimes, that are described by the Bose-Einstein and Fermi-Dirac statistics. Moreover, fully optical techniques can be exploited for trapping the atoms, thus resulting in a high manageability of the atomic sample. On the other hand, the control of single atoms is very challenging and the experimental cycle to produce a degenerate gas typically requires tens of seconds. Many fundamental results were achieved on degenerate quantum gases machines in the last years, ranging from the superfluid to Mott insulator trans-

ition [8] and Anderson localization [9] to fermionic superfluid pairing [10].

Platforms based on arrays of trapped ions, instead, offer great control on a single atom's degrees of freedom and fast experimental cycles (typically below one second), which allow for a larger statistics, but are difficult to scale up above a few tens of particles due to the strong Coulomb interaction between the electrically charged ions. Some of the most important results obtained exploiting this kind of platform falls in the range of simulation of spin models [11] and the implementation of qubit systems [12].

More recently, a new kind of platform has been introduced, which benefits from most of the advantages of the previously cited schemes, while minimizing some of their weaknesses. This platform consists in arrays of individual neutral atoms trapped in micron-scale optical traps, called optical tweezers, obtained by tightly focusing individual laser beams through a high-resolution microscope. This approach combines the high degree of quantum control and the fast experimental cycles of trapped ion arrays with the versatility of a fully optical trapping technique, which allows the number of particles to be upscaled more easily than in the case of trapped ions, up to hundreds of particles. With the adoption of opportune atom-sorting methods, it is possible to realize defect-free atomic arrays with zero configurational entropy and arbitrary geometries, allowing for the implementation of quantum simulators with different topologies, that can be probed via high-fidelity imaging with single-atom resolution performed through the same high-resolution objective used to generate the optical tweezers. The realization of such optical trapping potentials requires the use of peculiar devices, the acousto-optic deflectors (AODs). Such devices, driven by a RF signal, can deflect an incoming beam at different angles whose values depend on the frequency components of the RF signal. AODs are very flexible devices that can be exploited both for the direct generation of an array of optical tweezers, and also for the rearrangement of the arrays generated by exploiting different devices, for example a spatial light modulator (SLM).

In this thesis I develop and characterize the techniques for generating and manipulating an array of optical tweezers employing a pair of AODs, in the context of the realization of a quantum simulation platform based on Rydberg Strontium atoms trapped in optical tweezers arrays. In particular, in chapter 2 I introduce some important concepts underlying the experimental platform. Among these concepts, a few different techniques that allow for the generation of reconfigurable arrays of neutral atoms with arbitrary geometry are developed. Then, I will introduce some important notions regarding Rydberg atoms and their properties, and the employment of Strontium atoms, pointing out the advantages of implementing them in the experiments. The first part of chapter 3 is dedicated to the discussion of the light-matter interaction theory, with particular attention to the optical dipole potential. In the second part of chapter 3 the effect of a time-dependent optical dipole potential over a Strontium atom is simulated. Two kinds of simulations are considered in these sections. The first one allows us to investigate the heating of an atom that is transported from one position in the array to a different one. This simulation fits into the context of the rearrangement procedures that allow for the creation of a defect-free array of optical tweezers.

Next, I analyze a trapping technique based on the time-averaging of the dipole potential over all the sites of the array. The effect of this time-dependent potential onto a trapped atom is investigated through a set of simulations too. In chapter 4 a full characterization of AOD's features is reported. In particular, both the static and the dynamic properties of the AODs are explored, regarding in particular the diffraction efficiency and the time-scales typical of the AODs dynamics. To conclude, chapter 5 is dedicated to the realization of optical tweezers pattern exploiting a pair of crossed AODs and a microscope objective. The tweezers patterns presented are obtained both using the pair of AODs in a static way and implementing the time-averaged technique. In this context I present a few patterns of optical tweezers realized exploiting both a static configuration of the AODs and the time-averaged one. Finally, transient effects that rise up as a consequence of the time-averaged potential are analyzed and characterized.

Chapter 2

Atom-by-atom assembler of many-body systems with Strontium atoms

In recent years a new promising platform is emerging in the landscape of of quantum simulation. This platform is based on tightly focused laser beams, called optical tweezers, that are used to trap individual neutral atoms of a laser cooled sample. By exploiting opportune techniques that will be described in this chapter, in this platform it is possible to manipulate and move the tweezers and the atoms trapped within them in such a way to create ordered, defect-free arrays of individual atoms with arbitrary geometry, thus allowing for an atom by atom assembly of a quantum system.

Single neutral atoms trapped in arrays of optical tweezers represent a middle ground between well established quantum simulation platforms like degenerate quantum gases and trapped ions platforms, combining desirable features of these platforms while minimizing some of their weaknesses. Degenerate quantum gases can employ hundreds of thousands of quantum neutral objects, thus allowing for a high accuracy of the measurements: the standard quantum limit on measurement accuracy, valid for non-entangled systems, scales as $1/\sqrt{N}$, where N is the number of atoms in this case. Moreover, many well known techniques can be carried out to manipulate ensembles of neutral atoms. In ion-based platforms, instead, the control and trapping of charged ions is a much harder task, and typically only a few tens of atoms at most can be trapped simultaneously. On the other hand, in this platforms the distance between individual ions is large enough to allow for single atom detection, which is instead typically not possible in quantum simulators based on degenerate gases, with the exception of extremely complex quantum gas microscopes. These two platforms also differ for another fundamental feature, that is the typical duty cycle: while degenerate quantum gases need a long process of cooling in order to trap the atoms, resulting in duty cycles of tens of seconds, experiments with trapped ions are typically realized in less than one second.

The platform based on neutral atoms trapped in optical tweezers combines qualities of these two architectures. On the one hand, it provides for the single-

atom resolution and the fast duty cycle typical of ion-based platforms. On the other hand, it offers the possibility to scale the number of atoms up to mesoscopic scales, above 100 atoms, and the neutral atoms optical trapping techniques can be leveraged to obtain completely arbitrary atomic configurations.

The first step in the realization of an optical tweezers platform is the development of the optical trapping system. In this thesis I will characterize and develop techniques based on Acousto-Optic Deflectors (AODs) for the generation of optical tweezers. Acousto-optic deflectors are very flexible devices that can be used both for generating directly arrays of optical tweezers, both in combination with other devices such as Spatial Light Modulators (SLMs) to produce arbitrary and complex pattern geometries for the array.

2.1 Generation of optical tweezers array

In this section the use of two kind of devices for the creation of arrays of optical tweezers, namely Spatial Light Modulators (SLMs) and Acousto Optic Deflectors (AODs), is discussed. As mentioned above, an optical tweezer is an optical dipole trap that is tightly focused, on a lengthscale of around 1 μm, by a high numerical aperture (NA) objective. Thanks to light-assisted collisions that rapidly expel pairs of atoms, it's possible to trap in the optical tweezer at most one single atom, thus making the tweezer a perfect tool to control and address single atoms [13, 14]. Pair losses are the consequence of the interaction of a pair of atoms trapped in the optical dipole potential with a properly detuned laser beam. This collisional blockade mechanism results in either zero or one atom loaded in an optical tweezer, with probability $p \sim 0.5$. The light-matter interaction describing the trapping technique is presented in the next chapter, in section 3.1.

The idea of trapping individual atoms can be extended to several optical tweezers, that can be assembled together to form an *array of OTs*. The assembly of several optical tweezers can be accomplished making use of mainly two devices to arrange the tweezers to form complex patterns, the above mentioned AODs and SLMs [15, 16]. Although these devices exploit completely different technologies, they can both produce multiple beams, that will then be focused to create multiple OTs, starting from one single laser beam. Arrays of hundreds of tweezers, and so hundreds of atoms, were recently realized by means of these two techniques [17, 18], as showed in figure 2.1.

Acousto optic deflectors are devices that use the acousto-optic effect to deflect a laser beam. Like acousto optic modulators (AOMs), AODs are composed of a piezoelectric transducer, that is guided by a RF signal, and a crystal that vibrates under the effect of the transducer. A more precise description of the acousto optic devices' apparatus can be found in chapter 4. The difference between AODs and AOMs is that the first are more suitable for the deflection of multiple beams at different angles. An AOD working with multiple frequency components produce a 1D array of deflected beams that, once projected by a high numerical aperture objective, form an array of optical traps in which atoms are trapped individually. Two dimensional arrays can be achieved by considering a pair of AODs oriented

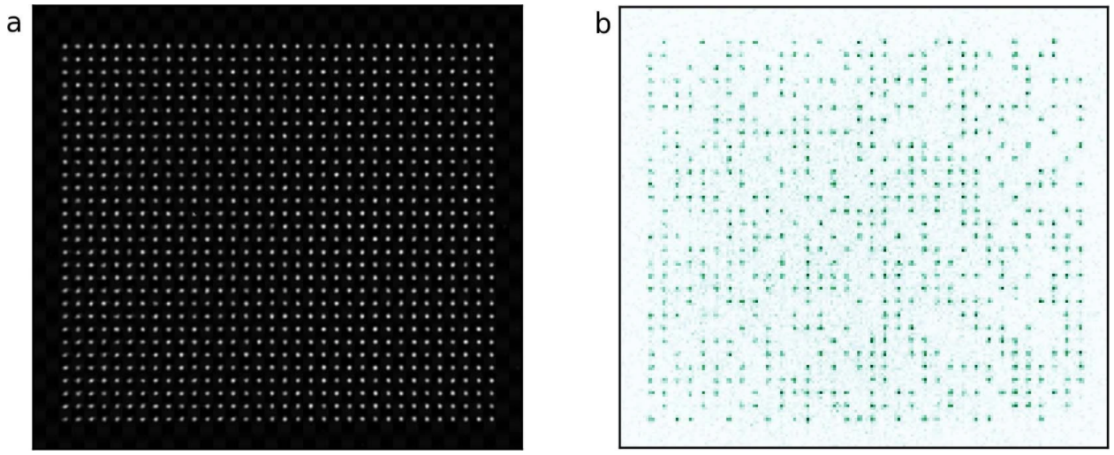

Figure 2.1: Experimental realization of a 34x30 array and sample image of a random loading. Each spot is the imaging fluorescence of one single atom. Image taken from [17].

perpendicularly, as shown in figure 2.2.

This simple scheme for the realization of a 2D array presents anyway some limitations, because it can only provide square or rectangular arrays. In fact, the presence of a perpendicular AOD can only copy the linear 1D patter in multiple lines/columns but is constrained by the pattern of the first 1D array. Nevertheless, more complex experimental schemes can be implemented to produce arbitrary geometry patterns both in a static and in a dynamic way. The static scheme makes use of SLMs, while the dynamic creation of arrays showing arbitrary geometry relies on a time-averaged potential technique that can be carried out by means of the AODs alone.

SLMs are based on liquid crystals, a completely different technology with respect to AODs. These devices work with holographic techniques and imprint a phase pattern on the input beam that hits the SLM's screen in order to obtain a certain spatial pattern in the conjugate plane. Liquid crystals are oriented with electric fields and behave as a diffraction grating for the light beam. According to the phase pattern imprinted on the screen of the device, the beam is deflected and the desired spatial pattern is reproduced onto the Fourier plane conjugated with the plane of the screen. SLMs allow for the realization of any kind of static pattern geometry. Moreover, these devices produce, in general, a higher number of spots, and so OTs, with respect to the AODs scheme.

A second way of producing an array of optical tweezers arranged in a pattern of arbitrary geometry relies on a time-averaged potential technique. This technique is currently used in many fields and applications but its implementation for the creation of array of optical tweezers is still under investigation. During my thesis work I carried out measurements and characterizations to study the feasibility of employing two crossed AODs to generate time-averaged optical potentials consisting in arbitrary patterns of OTs, which are shown in chapter 5. The basic idea of this technique consists in using one single deflected beam at

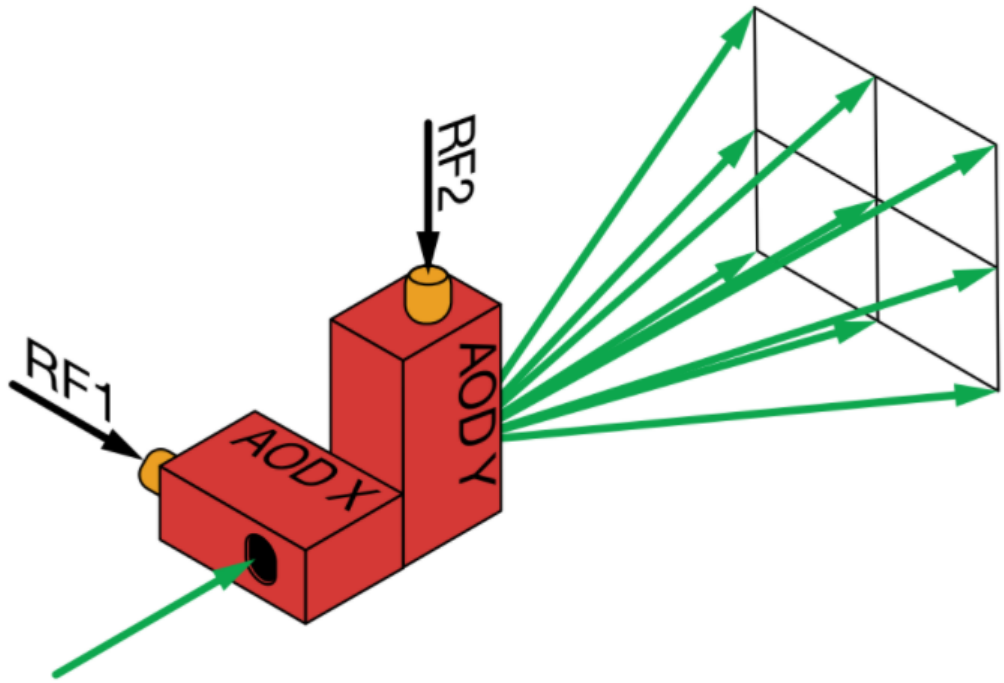

Figure 2.2: Creation of a 2D pattern using crossed AODs. Image taken from [19]

once and making it jump periodically over all the positions that we want to include in our array. During one cycle the beam spends a fraction of the period over each position. If one atom is initially trapped in one of these sites, it will feel a trapping potential as long as the deflected beam stays onto that site, while it falls down under the effect of gravity during the rest of the period. To trap the atoms with high fidelity, each atom has to be recaptured before it falls out of the action range of the optical tweezer trap, so the rate at which the potential is switched must be very high. In section 3.2 we characterize the optimal frequency for the switching. The methods described above satisfy only one of the two conditions that a good array of optical tweezers should have, that is the possibility of creating an arbitrary pattern both in one and two dimensions. Because of the light assisted collisions mentioned above, that produce the loss of pairs of atoms when they occupy the same site, an optical tweezer can be loaded with either zero or one atom. Typically, the probability of loading one atom per tweezer is $p \simeq 0.5$. This means that in every experimental cycle the stochastical loading of the atoms in the array will populate approximately the 50% of the sites. Hence, generating an arbitrary geometry array is not sufficient, and a feedback system that allows for the rearrangement of the atoms is necessary to prepare the ensemble of atoms in the array in the desired configuration.

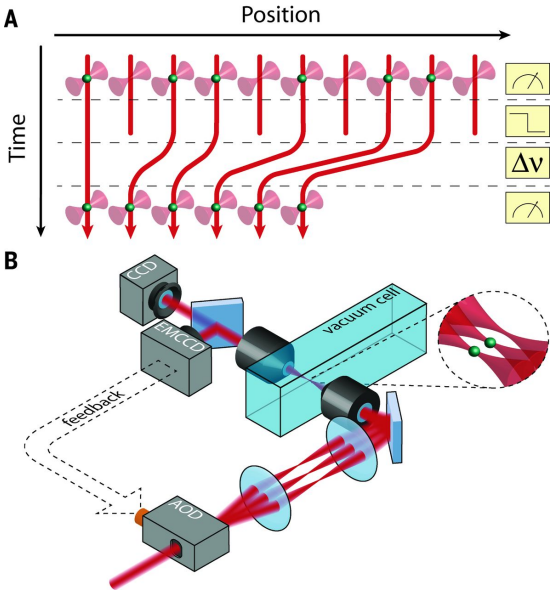

(a) 1D array created using only one AOD. Image taken from [15]

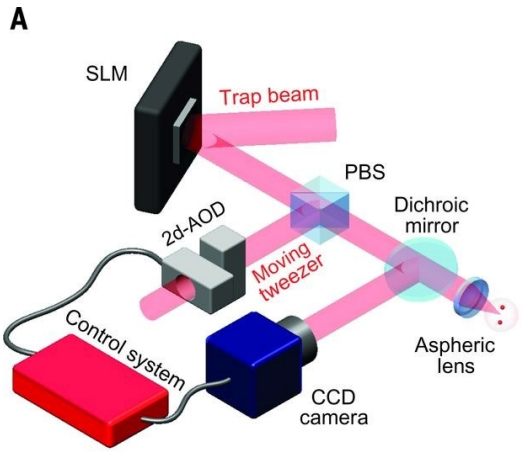

(b) 2D array created with a SLM. Image adapted from [16]

Figure 2.3: Realization of OT arrays by means of AODs and SLMs.

2.1.1 Rearrangement and feedback

The probability of having a defect free array made of N single atoms each trapped in one OT of the array is $P_{d.f.} = p^N$, where p is the single-site loading probability. Since p is less than 1, the chance of obtaining a defect free array is much less than 1 and it becomes smaller and smaller at increasing number of particles. In other words, even if it were possible to engineer light-assisted collisions that guarantee a single tweezer loading probability $p \simeq 1$, the power scaling with the number of sites would still give the probability to obtain a defect free array much less than 1.

Thanks to AODs it is possible to overcome this issue and rearrange the pattern of the atoms in the array. In most of the rearrangement protocols used in current experiments a camera captures an image of a randomly loaded array at a certain time. A computer elaborates the image determining which sites are loaded and which are not and calculate a sequence of *moves* to perform in order to create a defect-free array. After every sequence of moves the camera takes a new picture to observe if the moves were successful.

AODs represent the crucial tool for the rearrangement protocols. For 1D arrays (apparatus in figure 2.3a) the same AOD that creates the original pattern can perform the rearrangement too, as shown in figure 2.4a. An array initially composed of tens of randomly loaded tweezers is imaged by a camera and the image is processed by a computer to determine which sites are empty. The frequency components corresponding to these spots can be switched off and the remaining loaded tweezers are rearranged in a desired position. To move the loaded tweezers towards a desired position (for example in order to have equally

(a) Defect free 1D array rearranged using one AOD. Image taken from [15]

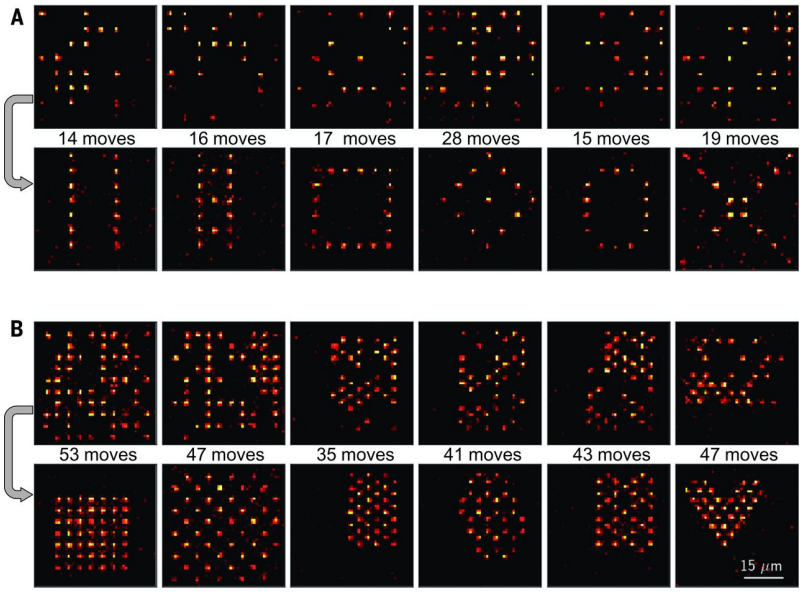

(b) Defect free 2D arrays rearranged using a couple of crossed AODs. Image adapted from [16]

Figure 2.4: Rearrangement of arrays of optical tweezers in arbitrary patterns.

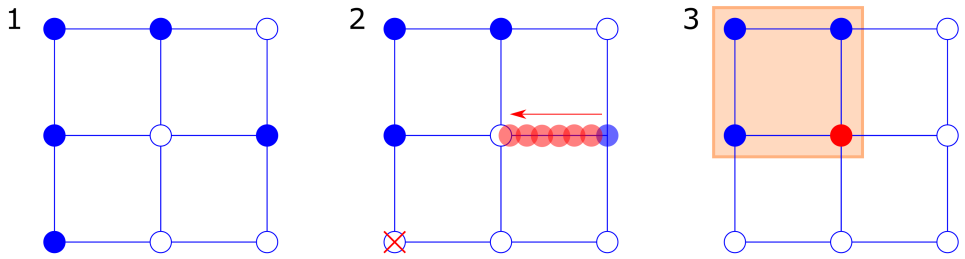

Figure 2.5: Example of a time-average trapping and reconfiguration of the array.

spaced tweezers) it is sufficient to sweep slowly the corresponding RF frequency components up to the final desired value.

The rearrangement in the 2D case is more complex: the array is typically generated by means of a SLM, and a pair of crossed AODs is used to generate a single tweezer that can be moved across the array by changing the RF frequencies driving the devices and can perform the rearrangement. An example of such apparatus is the one in figure 2.3b, where a moving tweezer generated by the AODs is superimposed to the static pattern produced by a SLM. The single tweezer produced by the AODs is deeper and picks up one atom from the static tweezer to move it towards a target tweezer. There, the depth of the moving tweezer is decreased to release the atom. A sequence of tens of such moves can produce the arbitrary patterns presented in figure 2.4b, starting from the randomly loaded configurations that are shown above.

In this context, the time-averaged technique can prove useful for the rearrangement too. The deflected beam in this case is just one, so the operations on each tweezers are all decoupled. To perform rearrangement of the pattern, the total shift of the tweezer positions have to be decomposed in infinitesimal moves performed every time that the tweezer passes through each site of the array that requires to be moved. The translation of the atoms must be quasi adiabatic in such a way that the atom has enough time to adapt its position and follow the moving potential without getting lost. Figure 2.5 contains a pictorial representation of the time-averaged rearranging. A randomly loaded array with probability for each tweezer of $p \sim 0.5$ is imaged by the camera. The goal is to obtain a fully ordered cluster, for example the square at the top left that misses just one atom. Since the time-averaged deflected beam passes through all the sites, it is convenient to drop the unnecessary atoms. The missing atom is transported to the target site of the array via a series of gradual moves, performed in several periods in such a way that each move changes slightly the position of the atom.

The typical timescale that come out in the context of the rearrangement is the time over which the atom is moved from a starting site to the target one: the motion should be done in such a way to minimize the chances that the atom escapes the tweezer because of heating. In chapter 3 the optimal parameters for the motion equation of the tweezer are investigated. In the case of time-averaged arrays, another relevant timescale is the period over which a single deflected beam is

averaged over all the sites of the desired array. Simulations in chapter 3 will help the discussion of the optimal parameters for such dynamic potential.

Finally, an additional feature that the array of tweezers should comply is the uniformity of the trap depths over all the sites. Inhomogeneities across the array result in non-uniform trapping parameters, hence every atom has different trapping frequencies instead of having all the same one. In experimental realizations, especially for array generated through AODs, the initial array is not uniform as we will point out in the characterization in chapter 4. Several techniques have been developed to overcome the non uniformity, both for 1D and 2D arrays.

2.2 Rydberg atoms in optical tweezer arrays

The problem of how to build arrays of optical tweezers has been introduced so far. There are many ways of exploiting the optical tweezers array platform to study different physical problems, that differ for the kind of manipulation, the kind of quantum object analyzed and the physical properties observed. To cite just a few, it is possible to trap molecules in arrays of optical tweezers [20], implement quantum metrological systems producing arrays of atomic clocks [21] and the study of mesoscopic fermionic model systems, based on spin-exchange interactions between different orbitals [22]. Moreover, Rydberg excitation of neutral atoms can be exploited to produce strong dipole-dipole couplings [23].

In our platform we will leverage the Rydberg excitation for the simulation of quantum spin models, like Ising models or planar XY models. Moreover, the strong coupling will allow for the creation of multi particle entangled states that are fundamental in many fields of quantum science and technology, from quantum simulation of spin systems to digital quantum operation on quantum gates registers.

A Rydberg atom is an atom in which one core electron is excited to a high principal quantum number (n) energetic level. One possible scheme for obtaining a Rydberg atom relies on the excitation of the core electron via a laser coupling. If the atom considered is a neutral atom, it has no net charge and does not interact via Coulomb interaction. Nevertheless, in the Rydberg excitation regime the atom acquires a very large induced electric dipole moment. Many important properties of a Rydberg atom differ from those of a ground state atom, because they depend on the principal quantum number n. In table 2.1 we see for ex-

Properties of Rydberg states

Property	n-scaling	Value for $80S_{1/2}$ of Rb
Binding energy E_n	n^{-2}	-500 GHz
Level spacing $E_{n+1} - E_n$	n^{-3}	13 GHz
Size of the wavefunction $\langle r \rangle$	n^2	500 nm
Lifetime τ	n^3	200 μs
van der Waals coefficient C_6	n^{11}	4 THz$\cdot\mu$m^6

Table 2.1: Scaling depending on the principal quantum number of some important atomic properties.

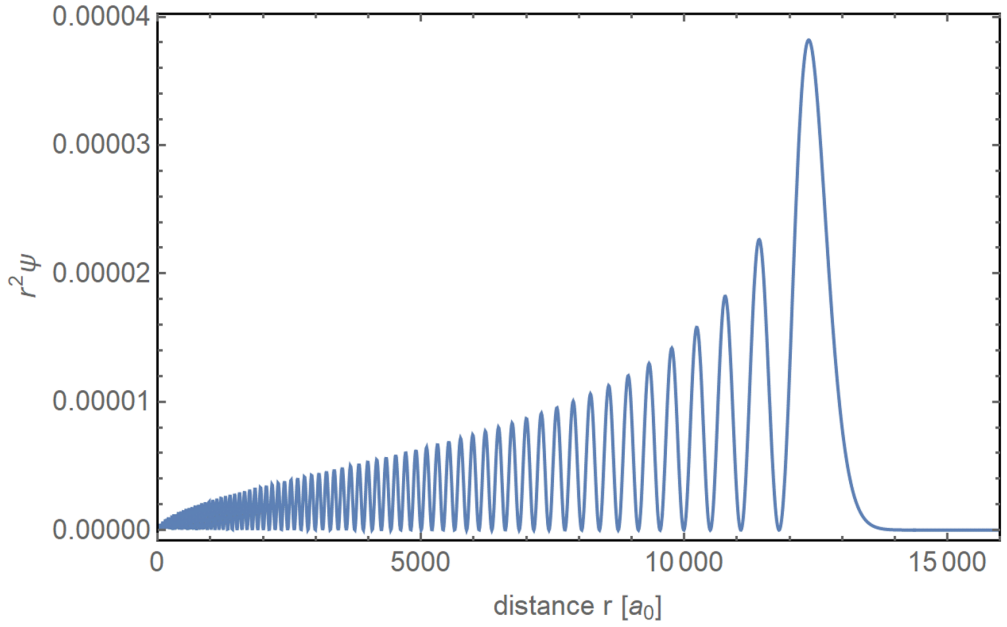

Figure 2.6: Simulated wavefunction for the $80S_{1/2}$ level

ample that the size of the wavefunction scales up as the square of n and can reach dimensions of a few μm. Figure 2.6 shows the simulation of the spatial wavefunction of a Rubidium Rydberg atom in the $80S_{1/2}$ state, which has an extension of the order of 1 μm. This aspect is fundamental for generating interaction between the atoms in the array of optical tweezers. Neutral ground state atoms do not interact via Coulomb interaction, since they have no net charge, but they can interact via van der Waals or dipole-dipole couplings. Anyway, the spatial extension of a ground state wavefunction, on the lengthscale of the Borh radius a_0, is so small that a couple of ground state atoms interact via contact interaction only. Since in optical tweezers each site is loaded with one atom, ground state atoms are not interacting at all in the array. In the Rydberg regime the spread of the wavefunction is instead 10^4 times higher and there is a non-zero overlap between neighbouring atoms in the array, that are typically separated by 5-10 μm. The atoms interact via strong induced dipole-dipole interaction. The interaction between a couple of atoms both excited to the same Rydberg level can be huge, as a consequence of the scaling of the van der Waals coefficient with the eleventh power of n, as pointed out in table 2.1. Actually, the van der Waals interaction is not the only regime in which atoms can interconnect, since they can also show dipolar interaction. These two interaction regimes differ on whether both the atoms are excited to the same Rydberg level or not. As shown in the next lines, dipolar and van der Waals interaction regimes have different scaling on the principal quantum number n and on the spatial separation R. Anyway, both the interaction regimes produce strongly interacting couples or ensembles of atoms.

Suppose that one core electron of the first atom is excited to the Rydberg state $|n,S\rangle$, where the labels n and s stand for the principal quantum number and the angular momentum of the target level. The second atom could be excited to the

same Rydberg level, but also to a different one $|n,P\rangle$ (we assume that the Rydberg levels differ just for the projection of the angular momentum, in such a way that the energy of $|n,P\rangle$ is the closest possible to that of $|n,S\rangle$ level. If the two atoms are separated at distance R, the interaction Hamiltonian describing the couple is an electric dipole-dipole interaction operator:

$$\hat{V}_{dd} \sim \frac{\hat{d}_1 \hat{d}_2}{4\pi\varepsilon_0 R^3} \tag{2.1}$$

The simplest case is that of two atoms excited to the same level, for example $|n,S\rangle$. The first order energy correction in perturbation theory, given by the expectation value of the Hamiltonian in equation (2.1) between the states $|n,S\rangle$, is zero because of parity. The first energy contribution is then of second order, where the interaction Hamiltonian connects the state of the couple of atoms $|n,S,n,S\rangle$ to other pair states that have different parity. The second order correction is given by the sum over all the possible final states, but the main contribution comes from the closest energy level (the one with same n but different angular momentum, for example P states). The resulting energy shift is proportional to V^2/Δ, where Δ is the detuning from the target level, and V is the matrix element $V \propto d_1 d_2/R^3$. On the other hand, two atoms excited to different Rydberg states, for instance $|n,S\rangle$ and $|n,P\rangle$ which differ only in the angular momentum quantum number so that there is still a sizeable overlap of the two wavefunctions, have nonzero expectation value at the first order in perturbation theory. In this context, the pair state $|n,S,n,P\rangle$ is directly coupled via a spin "flip-flop" to the complementary pair state $|n,P,n,S\rangle$. The energy correction in this case is proportional to $V \propto d_1 d_2/R^3$.

The n-scaling of the interaction coefficients can now be understood. Since the electric dipoles matrix elements scale as $d \sim n^2$ and the separation between next levels as $\Delta \sim n^3$ (see table 2.1), the energy correction for the van der Waals interaction and for the electric dipole interaction scale respectively as:

$$\Delta E_{vdW} \propto \frac{d^4}{\Delta}\frac{1}{R^6} \propto \frac{n^{11}}{R^6} \tag{2.2}$$

$$\Delta E_{dipolar} \propto \frac{d^2}{R^3} \propto \frac{n^4}{R^3} \tag{2.3}$$

The coupling can be extremely strong, especially the van der Waals interaction that can reach tens of MHz even for atomic separation of several micrometers [23].

Another important property of Rydberg atoms is that they can have quite long lifetimes, since the lifetime scales as n^3 too, as pointed out in table 2.1. To understand why lifetime of Rydberg states is large I recall the expression for the spontaneous emission rate:

$$\gamma \sim \omega^3 |\mu|^2 \tag{2.4}$$

where ω is the frequency separation between the initial and final states regarding the spontaneous emission and $\mu = \langle r|\hat{r}|t\rangle$ is the expectation value of the position

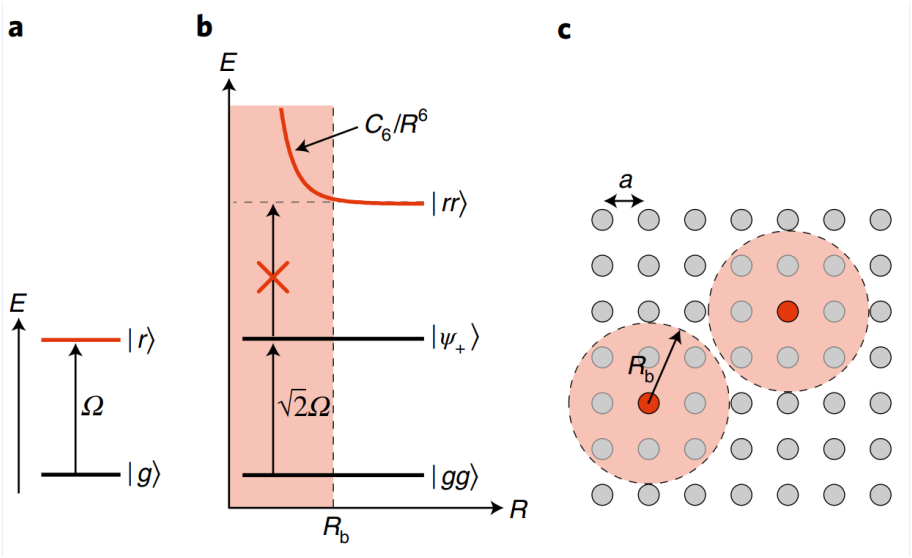

Figure 2.7: Rydberg blockade mechanism. Image adapted from [23]

operator between the Rydberg and a target eigenstates. In case of decay from the initial Rydberg state to another Rydberg state, the energy separation Δ is very small since it goes as n^{-3}, and the same does the frequency separation ω. The principal contribution to the scattering rate will then be the spontaneous emission towards the ground state, for which ω is large. In this case, however, the expectation value between Rydberg and ground states $\mu = \langle r|\hat{r}|g\rangle$ is small because the overlap between the wavefunctions is very little. The result is that the scattering rate for spontaneous emission from the Rydberg state is moderately small, hence its reciprocal, the lifetime of the level, is quite large and consistent with the scaling as n^3 showed in the table 2.1. The typical lifetime for an electron in a Rydberg state can reach hundreds of microseconds, a time long enough to observe the dynamics guided by interaction whose coupling is on the MHz scale, thus corresponding to 1 μs dynamics timescale.

Rydberg blockade

One of the straightforward consequences of the strong interaction between neighbouring atoms in the array of optical tweezers is the so-called Rydberg blockade mechanism. This is a conditional-logic effect that basically prevents the excitation of one atom to a Rydberg state if this is in the vicinity of an already present Rydberg atom. For a better understanding of the problem, figure 2.7 shows a 2D square array randomly loaded with atoms. Neglecting the presence of all the other states, we consider the atom as a two level system, that are coupled by a laser beam. The two levels are the ground $|g\rangle$ and the Rydberg $|r\rangle$, and the Rabi frequency that indicate the strength of the coupling is labelled as Ω. Consider two atoms loaded randomly in the square array depicted in the right side of figure 2.7, characterized by a lattice spacing a. The couple of atoms approximated to a two level systems have four possible pair states: $|gg\rangle$, $|rr\rangle$, $|rg\rangle$ and $|gr\rangle$, where

the last two are degenerate. While the $|gg\rangle$ state is almost non interacting, the $|rr\rangle$ state can be strongly interacting via van der Waals coupling which depends on the spatial separation. The second order energy correction associated to the van der Waals interaction can be strong enough to give a non-negligible energy shift (suppose that it is a positive energy shift) that takes the $|rr\rangle$ level out of the resonance of the laser coupling resonant with the unperturbed Rydberg transition of a single atom, if the atoms are close enough. A transition whose frequency is out of the finite bandwidth of the excitation laser is prevented. In the case of the Rydberg excitation, the energy of the pair of atoms ends up out of the bandwidth of the laser providing for the double excitation, making the transition to the $|rr\rangle$ state blockaded. This effect depends on the interatomic distance R, as represented in the central plot of the figure 2.7. In this plot the distance below which the van der Waals energy shift becomes a dominant effect is called Rydberg blockade radius (R_b).

Note that the energy shift to $|rg\rangle$ and $|gr\rangle$ states due to van der Waals interaction is negligible since one atom of the pair is in the ground state. These states are degenerate to the energy level labelled as $|\psi_+\rangle$ The state $|\psi_+\rangle$ is actually an entangled state given by the superposition of the states $|rg\rangle$ and $|gr\rangle$. Indeed, since the atoms are quite close, it is not possible to know which of the two atoms have been excited to the Rydberg level, and the correct way of describing the pair state is an entangled state of the pair where only one atom at once is in the Rydberg state. The state indicated with $|\psi_+\rangle$ is then:

$$|\psi_+\rangle = \frac{|rg\rangle + |gr\rangle}{\sqrt{2}} \tag{2.5}$$

This means that whenever two atoms have interatomic distance below the Rydberg blockade radius, the Rydberg excitation generates an entangled state between them. With similar considerations the blockade mechanism can be extended to multiple particles that form in turn a multi-particle entangled state when many of them are all among the blockade radius. It is interesting to note that the Rabi frequency of the coupling between $|gg\rangle$ and $|\psi_+\rangle$, compared to the Rabi frequency of the coupling of single atom ground state to single atom Rydberg state is enhanced by a factor $\sqrt{2}$, as pointed out in figure 2.7. The Rabi frequency of the coupling between the N particle ground state $|g...g\rangle$ and its corresponding entangled excited state $\frac{|rg...g\rangle + ... + |g...gr\rangle}{\sqrt{N}}$ is instead enhanced by a factor $\sqrt{N}$. The simple measurement of the Rabi frequency during Rabi oscillation dynamics is thus a clear signature for the presence of strongly correlated particles, as it was demonstrated and measured in [24].

An expression for the R_b radius can be determined observing that the atoms are blockaded as far as the van der Waals energy dominates over the Rabi coupling:

$$\frac{C_6}{R^6} \gg \hbar\Omega \implies R^6 \ll \frac{C_6}{\hbar\Omega} = \left(R_b^6\right) \tag{2.6}$$

The blockade radius is proportional to the C_6 coefficient of the van der Waals in-

teraction that depends on the Rydberg states chosen as target state for the excitation and it is then an experimental accessible parameter. The possibility to create entangled states is fundamental in many experimental applications. Entangling operation are basic for gates operation on qubit systems that can be implemented on this kind of platform [25]. Metrological applications as well take advantage of entanglement between subsystems to enhance the sensitivity in interferometric measurements [26, 27].

Rydberg atoms trapped in arrays of optical tweezers are not the only kind of platform that provide easy access to entangled states. The advantage of this platform is surely the flexibility and manageability both of the interaction and the geometry of the system. In other words, the proportions between the interatomic separation R and the blockade radius R_b can be tuned both by changing the spacing between optical tweezers implementing a different pattern on the SLM/AODs, and also by changing directly the strength of the van der Waals interaction and its action range R_b.

Simulation of quantum spin Hamiltonians

The two types of interactions described above, van der Waals and dipolar, that occur between a couple of Rydberg atoms, are associated with different spin models that are mapped onto the optical tweezers' platform.

The Hamiltonians that describe quantum spin models are called quantum Heisenberg Hamiltonians and can be used to describe quantum mechanically magnetic systems and their phase transitions [28, 29]. Actually, the class of problems that can be resolved with a spin Hamiltonian model is very rich and regards problems far away from magnetic systems too, for example combinatorial optimization problems [23]. The flexibility of Heisenberg Hamiltonians is due to its simplicity. In equation (2.7) a standard form for the Heisenberg Hamiltonian is reported [29].

$$H = -\sum_{ij} J_{ij}\mathbf{S}_i \cdot \mathbf{S}_j + g\mu_B \sum_j \mathbf{S}_j \cdot \mathbf{B} \tag{2.7}$$

In the expression above the first term is the interaction (or coupling) term between pairs of spins $\mathbf{S}_i$ whose strength is the coupling amplitude J_{ij}, and the second is the Zeeman term that is related to the interaction of the spin $\mathbf{S}_i$ with an external magnetic field $\mathbf{B}$. In case the spin variable is a scalar variable, the Hamiltonian in equation (2.7) is called Ising Hamiltonian. If the spin is instead constrained to a plane, the corresponding spin model is called a planar spin model or Heisenberg model. The importance of the Heisenberg Hamiltonians is that the same Hamiltonian can describe the physics of whatever variable can be associated to a spin variable.

In the case of the van der Waals interaction, we identify the eigenstates of the atom approximated to a two level system, the ground $|g\rangle$ and the Rydberg $|r\rangle$ with the spin basis for a spin 1/2 system in the following way: $|g\rangle = |\downarrow\rangle$ and $|r\rangle = |\uparrow\rangle$. Thanks to this identification, the Hamiltonian of an ensemble of atoms trapped

in an array of OTs can be written as [30]:

$$H = \frac{\hbar\Omega}{2}\sum_i \sigma_x^i - \hbar\delta\sum_i n_i + \sum_{i<j} V_{ij} n_i n_j \text{ , where } V_{ij} = \frac{C_6}{R_{ij}^6} \tag{2.8}$$

The atoms of the ensemble are subject to a coherent laser coupling characterized by a Rabi frequency Ω and detuning δ, and the van der Waals potential depends on the separation between atoms in site i and j R_{ij}. In the expression above σ_x^i is the Pauli matrix and n_i is the occupational number of the Rydberg/spin up state. The Hamiltonian in equation (2.8) is that of an Ising spin model since for a spin 1/2 system the relation $n_i = (\sigma_z^i + 1)/2$ holds. The first two terms of the Hamiltonian represent the interaction with a fictituous external magnetic field, whose longitudinal and transverse components are proportional to the detuning δ and the Rabi frequency Ω, respectively. The Ising coupling in the third term of the Hamiltonian (2.8) is proportional to the van der Waals potential and is hence distance-dependent.

As for the dipolar interaction between pairs of atoms, we deal with two different Rydberg states, for example $|nS\rangle$ and $|nP\rangle$ (we suppose that the states differ only for the angular momentum). The spin basis is here identified with the two Rydberg states, having $|nS\rangle = |\downarrow\rangle$ and $|nP\rangle = |\uparrow\rangle$. In this case the electric dipole-dipole interaction is responsible for the coherent coupling of the internal Rydberg states $|nS\rangle$ and $|nP\rangle$ that are typically separated by a few GHz. The coherent coupling between states can be here provided by a microwave field, unlike the Ising Hamiltonian in equation (2.8) for which a laser beam provides for the coherent coupling. Considerations similar to the previous ones lead to the identification of the Hamiltonian of an ensemble of atoms subject to the dipole-dipole interaction with the following XY Hamiltonian:

$$H = \frac{\hbar\Omega_{\mu w}}{2}\sum_i \sigma_x^i - \frac{\hbar\delta_{\mu w}}{2}\sum_i \sigma_z^i + \sum_{i\neq j}\frac{C_3}{R_{ij}^3}\left(\sigma_+^i\sigma_-^j + \sigma_-^i\sigma_+^j\right) \tag{2.9}$$

In the above expression the magnetic field components are represented by the Rabi frequency and the detuning of the microwave coupling that connects the Rydberg states, while the interaction term is given by the electric dipole interaction potential. While the van der Waals interaction is isotropic, the dipolar is stongly directional. Anisotropic coupling makes a system dominated by dipolar interaction unsuitable for the modeling of an Ising Hamiltonian. However, it was demonstrated [23] that such a system can be mapped onto a planar XY spin 1/2 Hamiltonian.

Most of the parameters of the Hamiltonians in equations (2.8) and (2.9) are experimentally accessible ones, making the simulation of these spin models extremely flexible and manageable. In both Hamiltonians the components of the fictituous external magnetic field are proportional to the parameters of the coupling between the states identified with the spin basis. Moreover, also the C_3 and C_6 interaction coefficients are experimentally tunable, since their strength depends on the target Rydberg states chosen for the excitation. Last but not least,

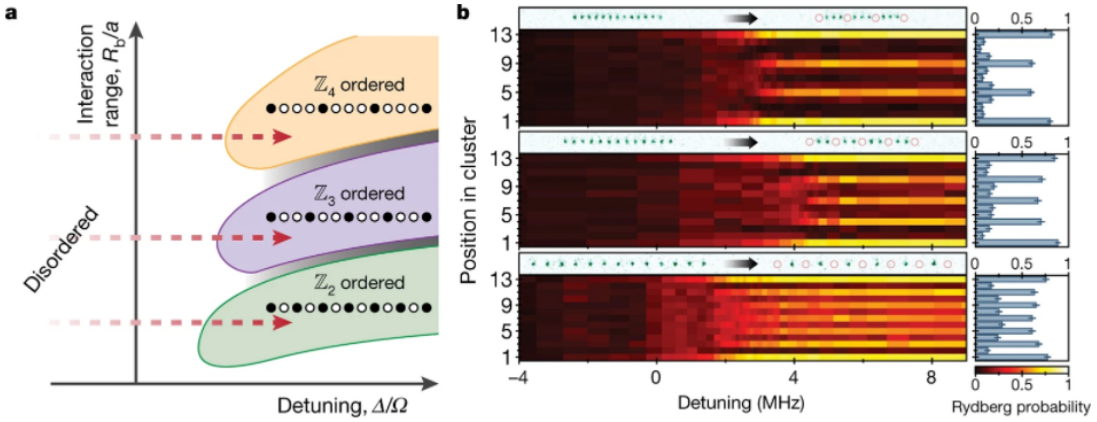

Figure 2.8: Phase diagram obtained as a function of the Hamiltonian parameters by the direct measurement of correlation functions. Image taken from [31]

the tweezers platform allows for the manipulation of the inter-site separation R_{ij} too, that can be found at the denominator of the coupling terms both in equation (2.8) and equation (2.9).

Ising and planar spin models have been studied in the past years and are generally well known quantum systems. The advantages offered by the Rydberg tweezers platforms are those pointed out in the last few lines: the high access to experimental parameters, even in regimes that are not available for other platforms, and the addressability and control of individual sites and quantum objects. The addressability of single atoms, guaranteed by the fact that optical tweezers are separated by several micrometers and trap at most one atom, allows for measurements with single site resolution. For example, in figure 2.8, a measurement of correlation functions with sensibility over the single atom is reported. This measurement, realized with an 1D array of Rydberg atoms in optical tweezers simulating an Ising spin model [31], can be exploited to draw a phase diagram as a function of the Ising Hamiltonian parameters R_b (Rydberg blockade radius), Δ (detuning) and Ω (Rabi frequency). The disordered phase goes through a quantum phase transition tuning the ratio Δ/Ω, parameters that represent the components of the external magnetic field in equation (2.8). Different ordered phases are encountered changing instead the interaction range R_b/a, where a is the spacing between next neighbours in the array. On the right side of figure 2.8 the cumulative probability (over the whole array) of finding one atom in the Rydberg state is plotted as a function of the detuning of the laser for different values of R_b/a. For negative values of the detuning the corresponding term in the Ising Hamiltonian (eq. (2.8)) is positive, hence it is energetically favoured to minimize n_i that is the number of Rydberg atoms. Oppositely, for large enough detuning, this term of the Hamiltonian becomes dominant and *aligns* upside as most spins as possible. The interaction term still constraints the configuration of atoms to be blockaded within the interaction regime R_b/a. The three plots on the right in figure 2.8 are realized for $R_b \sim a, 2a, 3a$, in such a way that one, two and three neighbours of the Rydberg atom are blockaded.

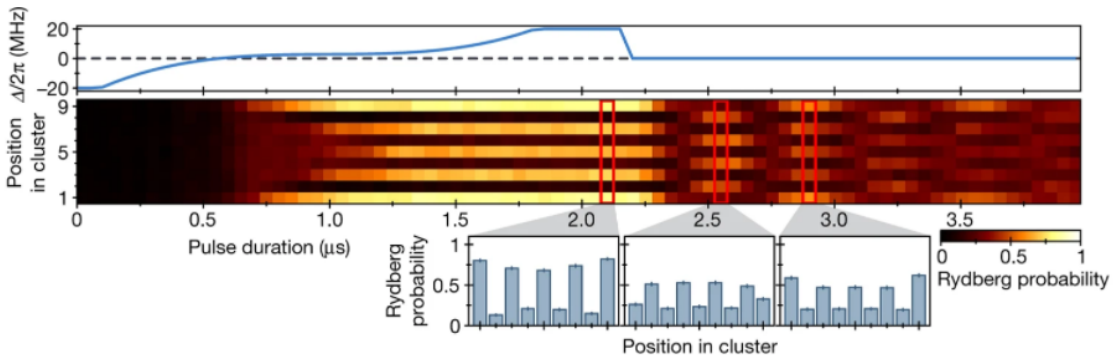

Figure 2.9: Out of equilibrium dynamics of the correlation function describing a linear array. Image adapted from [31]

Anyway, this platform is suitable not only for the realization of *steady state* measurements, like the phase diagram of a spin system, but it also allows for the study of out of equilibrium dynamics, since it offers the possibility to measure directly single atom properties in real time. The capability of the quantum simulator to give access to the investigation of out of equilibrium dynamics opens up promising and full of prospects field of research. In figure 2.9 the time evolution after the sudden quench of the detuning of the laser is shown. The system is first adiabatically prepared in an ordered phase that is an out of equilibrium condition for the system. When the detuning is suddenly quenched to 0 the laser is resonant with the atomic transition and interesting dynamics show up: the antiferromagnetic phase bounces back and forth between the initial configuration and the complementary one where all the spins are flipped (atoms in the ground finish in the Rydberg state and vice versa).

Perspectives of the platform

To conclude this section, the target experiments suitable for the Rydberg optical tweezers machine that we would like to investigate are mainly the simulation of out of equilibrium dynamics and the study of frustrated systems. Quantum spin models, both Ising and XY Hamiltonians, can be implemented in different geometry patterns indeed, paving the way towards the study of different topologies. For example, the well known physics of an Ising model in a square array is completely different from a frustrated system like an Ising model in a triangular array. The manageability of the array of optical tweezers makes it an easy task to rearrange the ensemble of Rydberg atoms into different array geometries.

The second development direction is a more general one, that is the realization of a quantum coprocessor. A quantum coprocessor is a device that helps a classical computer to perform some parts of algorithms in which the coprocessor offers quantum advantage, for example in terms of computational time. In figure 2.10 a schematic representation of the quantum coprocessor is shown [32]. The coprocessor can perform both analog operations and digital ones. The simulation of a quantum spin model is an example of an analog operation, where

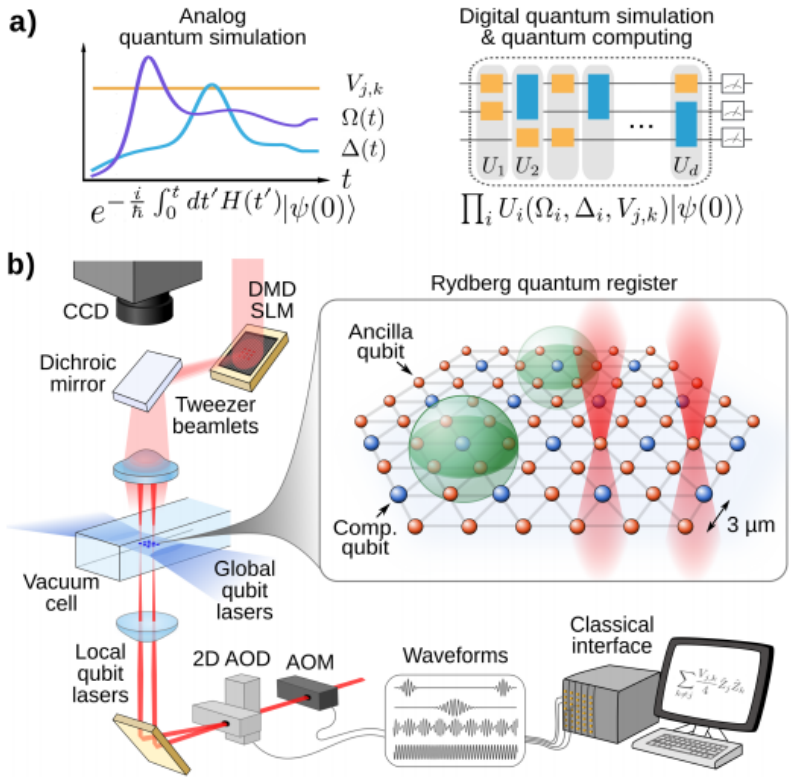

Figure 2.10: A quantum coprocessor operates with both analog and digital operation to elaborate sections of algorithms. Figure taken from [32]

interactions among the atoms are exploited to simulate the time evolution of the ensemble. All the problems that can be directly mapped onto a spin system are solved with analog operations. The atomic systems can be also be seen as qubits. The array of quibits represents the quantum register over which digital quantum operations can be performed. There are many possibilities for encoding the qubit states into a couple of eigenstates of the atom. The easiest encoding identifies the computational basis $|0\rangle$ and $|1\rangle$ with the ground and Rydberg states, but a few other possibilities have been proposed in current experiments, depending on which atomic species is used. The Rydberg excitation is anyway an useful tool that is leveraged to connect different qubits with a strong coupling at large distance and to create entanglement, thanks to the Rydberg blockade mechanism. Both single gate operations, such as rotations of the qubit, and multiple gate operations, exploiting the Rydberg excitation, can be performed on the quantum register, opening up the possibility to perform digital operations too.

2.3 Strontium Rydberg atoms

The choice of the atomic species to be used for the optical tweezers platform is as important as the type of interaction that is exploited. In particular, different atomic species have rather different internal structure and the techniques for both excitation and cooling of the atoms can be quite different. Up to now, most of the experiments based on Rydberg atoms in optical tweezers exploited alkali atoms such as Rubidium (for example [17, 24, 31]), but in recent years alkaline-earth atoms got implemented too [19, 27, 33]. In our experiment we will use Strontium Rydberg atoms. Strontium (Sr) is an alkaline-earth atom of atomic number Z=38 with a pair of valence electrons and electronic configuration $[Kr]5s^2$ for the ground state. Typically, a natural sample of Sr atoms contains many isotopes, among which the most common is a boson, ^{88}Sr, with abundance of approximately 82.6%. There is only one fermionic isotope among all, the ^{87}Sr with 7% abundance. Since the atoms in the array of optical tweezers are individually trapped, they are distinguishable and no particular differences stand between the bosonic and fermionic isotopes. A diagram showing a few relevant singlet and triplet states for a Strontium atom is reported in figure 2.11. Differently from alkali atoms, that have just one valence electron, two electron atoms have both singlet and triplet states that in first approximation are not connected by atomic transitions because of selection rules.

Alkaline-earth atoms present many advantages with respect to the alkalis, mainly because of the richness of the internal structure. Two electron atoms have two important features: the presence of intercombination transitions that, since they are forbidden by selection rules, have narrow and ultranarrow linewidths, and of metastable states characterized by long lifetimes. These aspects are relevant for the design of both cooling and excitation schemes. Moreover, the ultranarrow transition connecting the ground state $^1S_0$ to the metastable clock state $^3P_0$ are leveraged in most recent optical atomic clock experiments that reached out extreme accuracy and stability standards [34, 35].

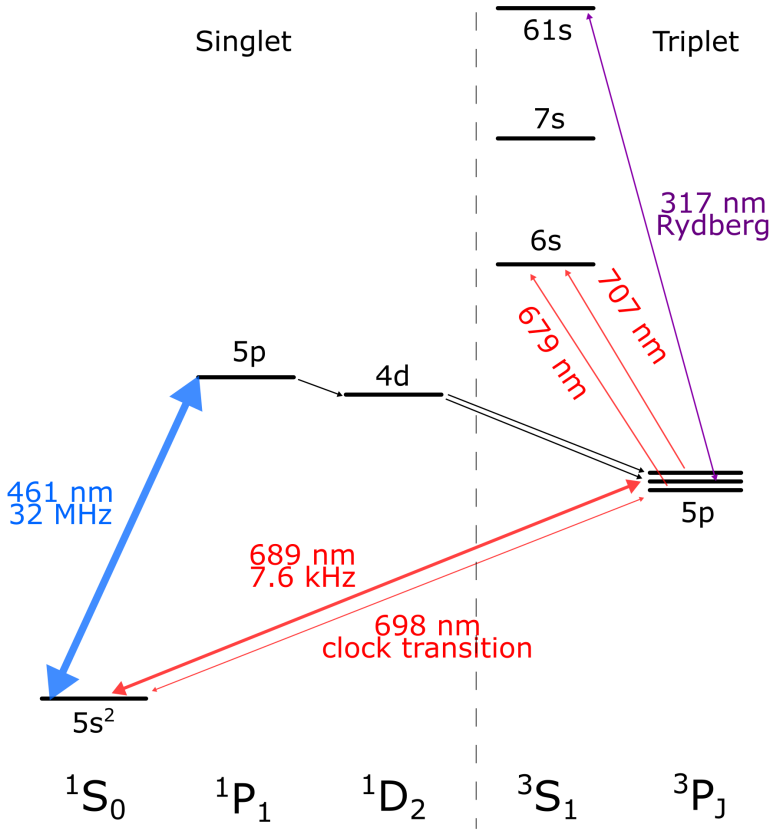

Figure 2.11: Relevant energy levels for a Strontium atom divided into singlet and triplet levels.

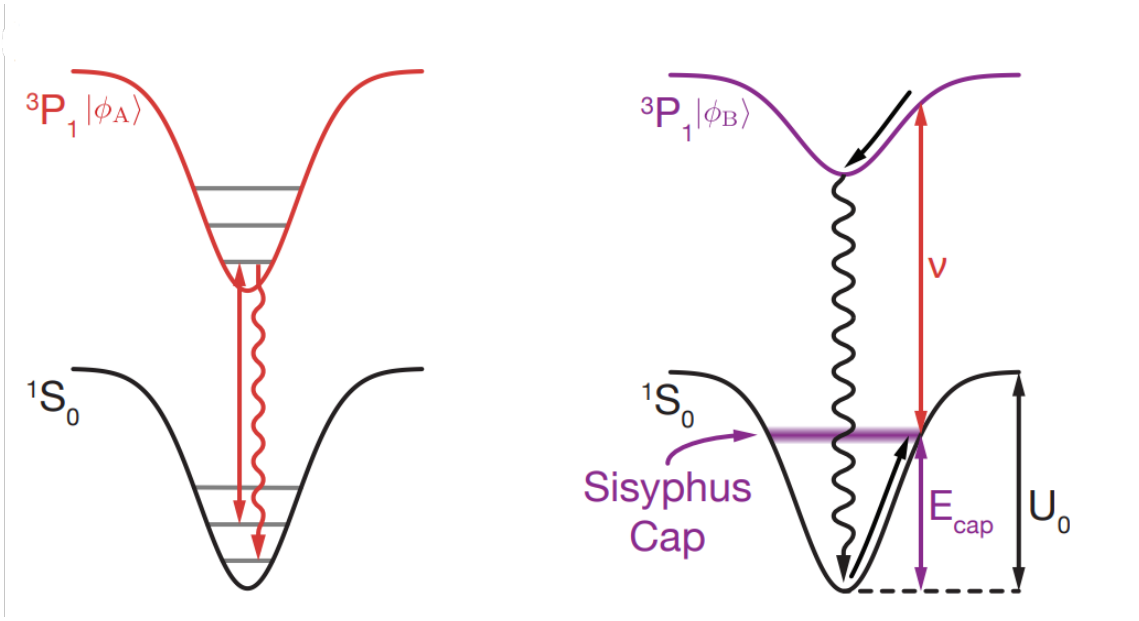

(a) Sideband cooling scheme for a two-electron atom trapped in an optical tweezer. Image adapted from [19]

(b) Sisyphus cooling scheme for a two-electron atom trapped in an optical tweezer. Image adapted from [19]

Figure 2.12: Sideband and Sisyphus cooling techniques.

The cooling stage can be performed with two stages of Magneto Optical Trap (MOT): the first one exploits the principal blue excitation line for Sr atoms, the $^1S_0 \rightarrow ^1P_1$ transition at 461 nm, then in the second stage the $^1S_0 \rightarrow ^3P_1$ red intercombination line (at 689 nm) is used. The linewidth of the intercombination line is $2\pi * 7.6$ kHz and it is small enough to cool the atoms down to a few hundreds of nK [36], a temperature much lower than that achievable for alkali atoms with the Doppler cooling only. The efficient Doppler cooling performed thanks to the red line is sufficient to trap the atoms in the optical tweezers, whose trap depth is on the order of 1 mK. Hence, an evaporative cooling procedure is not necessary for this application. This is important because it drops significantly the preparation time during a typical duty cycle. Although the temperature reached by the MOT is low enough to trap the atoms in the tweezers, there is still a nonzero probability of finding the atoms in excited vibrational states in the trap. It is then possible to implement cooling schemes directly in the tweezer that allow us to cool the atom down to the ground state of the trap. In the case of Sr atoms, two possible approaches can be exploited, depending on the wavelength of the tweezer traps.

The first cooling technique is a sideband cooling, that exploits red sideband trasitions to decrease the vibrational state of the atom in the trap. In the case of alkali atoms the natural linewidth of the atomic transitions is larger than the vibrational levels spacing, hence the technique used for cooling the atom in the trap is the Raman sideband cooling, that makes use of a two photon transition whose energy separation covers the energy gap between vibrational states. The sideband cooling used for two-electron atoms, such as strontium, is instead a *dir-*

ect scheme, based on a single photon transition and spontaneous decay. Let us consider the atom as a two level system, $|g\rangle$ and $|e\rangle$, trapped in an optical tweezer at magic wavelength, such that the two levels feel the same trapping potential due to identical light shifts. A schematic representation of the sideband cooling is shown in figure 2.12a: the frequency of the red transition is tuned in such a way to excite the atom from $|g\rangle$ state to the $|e\rangle$ state, but in a lower vibrational level. It was verified, for example in [19], that under certain experimental conditions the spontaneous emission decay maintains the vibrational state of the atom, hence the net result is a decrease in vibrational level. Such a cooling scheme is not possible for alkalis, because the bandwidth of the excitation laser is much larger than the separation between vibrational levels and a proper target level cannot be chosen. The sideband cooling scheme can be implemented for Sr atoms exploiting the intercombination line ${}^1S_0 \rightarrow {}^3P_1$ that has a natural linewidth of $2\pi 7.6$ kHz, smaller than the typical separation between vibrational levels that is of the order of tens of kHz.

A second cooling technique, called Sisyphus cooling, can be exploited to keep the atoms below a desired value of motional energy within the trap [19]. In this case a non magic wavelength trap is considered: for example the excited state $|e\rangle$ is less trapped than the ground $|g\rangle$. This mechanism is important especially during the imaging stage, where atoms continuously scatter the broad band blue light. The energy kicks of the imaging light heat up the atoms in the $|g\rangle$ state, increasing their vibrational state. Since the trapping potential is non magic, the photon of the Sysiphus cooling laser beam is resonant only for a restricted fraction of atoms that have the correct energy. Consider for example 2.12b, where a photon with frequency ν is resonant with the $|g\rangle \rightarrow |e\rangle$ transition at the side of the trap. If an atom acquires enough energy to reach the value for which the cooling photon is resonant, it will be excited to the $|e\rangle$ state. After spending some time in the excited trap, the atom decays preferably in the ground vibrational level of the electronic state $|g\rangle$. This mechanism keeps the atoms below the energy value for which the cooling photon is resonant. The cooling works because of the mismatch of the energy of the photons exchanged. In particular, the cooling photon is less energetic than the spontaneously emitted one.

Regarding the Rydberg excitation scheme, two-electron atoms offer two possible configurations. The first possible excitation scheme leverages a coherent two photon transition and can be performed both on single electron atoms and on two-electron atoms. In figure 2.11 a schematic representation of the two-photon Rydberg excitation is presented. In the case of Sr, an intercombination line is exploited for the first transition, typically the ${}^1S_0 \rightarrow {}^3P_1$ line, benefiting of the narrow linewidths that guarantee long coherence times. The second photon is instead an ultraviolet photon at ~ 317 nm, depending on which target Rydberg state is chosen. The overall transition couples coherently the ground with the Rydberg state and is characterized by a Rabi frequency Ω and a detuning δ. A second method for the excitation of a two-electron atom to the Rydberg state is described in detail in [36] and relies on the clock state ${}^3P_0$. Instead of treating this state as an intermediate state in the two photon transition, thanks to its long lifetime the clock state can be seen as a new ground state from which single photon

transitions excite the atom directly to the Rydberg state. While in the previous method one red photon and one ultraviolet photon excited simultaneously the atom, now the two transitions are performed in a sequence. The atom is first excited to the clock state that represents the new metastable ground state, then a second single-photon transitions excites the atom to the Rydberg state. The fact that the second mechanism is actually a single photon transition, instead of the two photon one that is exploited for the first method, offers a few advantages, for example larger Rabi frequencies and the absence of decays from the intermediate state.

To summarize, two-electron atoms take advantage of the intercombination lines for the excitation and cooling schemes with respect to alkali atoms for which these narrow and ultranarrow transitions are not present. As for the Rydberg excitation in particular, these lines allow us to couple the ground and Rydberg state with high Rabi frequencies. The long lived or metastable ^3P_J levels can be exploited for the qubit encoding too, since they offer great coherence and long lifetimes. Identifying the computational basis with the ground and the Rydberg state is a common choice and the easiest one, because it offers quite long lifetimes and also the connection between distant qubits thanks to the strong Rydberg interaction (see table 2.1). A refinement of this scheme can be achieved by encoding the qubit states into a couple of stable/metastable states such as the ground $^1S_0$ and the clock $^3P_0$ in order to have extremely long lived levels and coherent coupling. The Rydberg excitation can be leveraged as an additional tool to link the quibits along the array of optical tweezers.

Chapter 3

Optical Tweezers

In this chapter I will present the theoretical approach to Optical Tweezers. In section 3.1, optical trapping equations are derived using a semiclassical approach, then advanced trapping methods are discussed in section 3.2. The results of quantum-mechanical simulations are reported at the end of the chapter, in section 3.3.

3.1 Dipole force and optical trapping

Let us discuss the mechanical effect of a coherent light source onto the atomic sample. In particular, we consider the effect of a monochromatic electromagnetic field applied to a Strontium atom [37, 38]. The total Hamiltonian of the open quantum system composed of the laser field (L), the atom approximated to a two level system (A) and the environment (E) is the following:

$$\hat{\mathrm{H}} = \frac{\hat{\mathrm{p}}^2}{2\mathrm{M}} + \hbar\omega_{\mathrm{g}}|\mathrm{g}\rangle\langle\mathrm{g}| + \hbar\omega_{\mathrm{e}}|\mathrm{e}\rangle\langle\mathrm{e}| + \hat{\mathrm{V}}_{\mathrm{AL}}(\hat{\mathrm{R}}) + \hat{\mathrm{V}}_{\mathrm{AE}}(\hat{\mathrm{R}}) \tag{3.1}$$

where the first term is the external motion energy of the atom, the second and the third term describe the energy of the internal state, and the last pair represents the atom-light interaction (both the laser and the vacuum). The energies of the internal states $|\mathrm{g}\rangle$ and $|\mathrm{e}\rangle$ are $\hbar\omega_{\mathrm{g}}$ and $\hbar\omega_{\mathrm{e}}$, respectively. M is the mass of the atom, while $\hat{\mathrm{p}}$ and $\hat{\mathrm{R}}$ are the momentum and position operators of the particle. The force felt by the atom can be written as the commutator between the Hamiltonian of the system and the momentum operator:

$$\hat{\mathbf{F}} \doteq \frac{\mathrm{d}\hat{\mathbf{p}}}{\mathrm{dt}} = \frac{i}{\hbar}\left[\hat{\mathrm{H}}, \hat{\mathbf{p}}\right] = -\boldsymbol{\nabla}_{\mathbf{R}}\hat{\mathrm{H}} \tag{3.2}$$

The only term in the Hamiltonian (3.1) showing spatial dependence are the atom-light interaction terms. The atom-laser interaction in electric dipole approximation is $\hat{\mathrm{H}}_{\mathrm{AL}} = -\hat{\mathbf{d}} \cdot \mathbf{E}$, where $\hat{\mathbf{d}}$ is the electric dipole operator.
$\mathbf{E} = \hat{\mathbf{e}}\varepsilon(\mathbf{R})\cos[\omega\mathrm{t} + \phi(\mathbf{R})]$ is the electric field associated with the laser beam. The electric field is characterized by polarization vector ê, amplitude $\varepsilon(\mathbf{R})$, frequency

ω and phase $\phi(\mathbf{R})$. We can now consider the expectation value of the force operator over the state of the system:

$$\mathbf{F} = \langle \hat{\mathbf{F}} \rangle = \langle \boldsymbol{\nabla} \Big(\hat{\mathbf{d}} \cdot \mathbf{E} \Big) \rangle - \langle \boldsymbol{\nabla} \hat{\mathrm{V}}_{\mathrm{AE}}(\hat{\mathbf{R}}) \rangle \tag{3.3}$$

In equation (3.3) the second term can be dropped because the atom-environment interaction, resulting in spontaneous emission, is isotropic and gives zero expectation value. Assuming now the adiabatic approximation, valid if the timescale for the external motion of the atom is much faster than the typical internal-state evolution, the center of mass variables $\mathbf{R}$ and $\mathbf{p}$ are treated classically and the internal state is described by the stationary Optical Bloch Equations (OBE) solutions. Applying these approximations the force expression becomes:

$$\mathbf{F} = \langle \hat{\mathbf{d}}_{\mathrm{i}} \boldsymbol{\nabla} \mathrm{E}_{\mathrm{i}}(\mathbf{R}) \rangle = \langle \hat{\mathbf{d}}_{\mathrm{i}} \rangle \boldsymbol{\nabla} \mathrm{E}_{\mathrm{i}}(\mathbf{R}) = \mathrm{d}_{\mathrm{i}}^{\mathrm{st}} \boldsymbol{\nabla} \mathrm{E}_{\mathrm{i}}(\mathbf{r}) \tag{3.4}$$

Calculating $\mathrm{d}_{\mathrm{i}}^{\mathrm{st}}$ with the stationary solution of the OBE one obtains that the electric field induces an electric dipole oscillating at the frequency of the laser radiation. The induced dipole is composed of two terms, one in phase with the electric field and one out of phase by 90°. Substituting the expression for $\mathrm{d}_{\mathrm{i}}^{\mathrm{st}}$ in equation (3.4) and averaging for long times the force becomes:

$$\mathbf{F} = -\frac{\hbar \boldsymbol{\nabla} \Omega}{2} \mathrm{u}^{\mathrm{stat}} - \frac{\hbar \Omega \boldsymbol{\nabla} \phi}{2} \mathrm{v}^{\mathrm{stat}} \tag{3.5}$$

where Ω is the Rabi frequency, ϕ is the phase of the electric field and $\mathrm{u}^{\mathrm{stat}}$, $\mathrm{v}^{\mathrm{stat}}$ are the components of the Bloch vector representing the internal state of the atom. In particular, we have:

$$\Omega = \frac{\mathrm{e} \boldsymbol{\mu}_{\mathrm{eg}} \cdot \hat{\mathbf{e}} \varepsilon(\mathbf{R})}{\hbar} \quad , \quad \boldsymbol{\mu}_{\mathrm{eg}} = \langle \mathrm{e} | \hat{\mathbf{r}} | \mathrm{g} \rangle \tag{3.6}$$

where $\hat{\mathbf{r}}$ is the electron's position operator,

$$\mathrm{u}^{\mathrm{stat}} = \frac{\Omega \delta}{\delta^2 + \frac{\gamma^2}{4} + \frac{\Omega^2}{2}} \quad , \quad \mathrm{v}^{\mathrm{stat}} = \frac{\Omega \gamma / 2}{\delta^2 + \frac{\gamma^2}{4} + \frac{\Omega^2}{2}} \tag{3.7}$$

In equation (3.7) δ is the detuning of the laser beam and γ is the linewidth of the atomic transition. The two terms in equation (3.5) are the dipole force and the radiation pressure, respectively. The dipole force is a conservative contribution that corresponds to the in-phase oscillation of the induced electric dipole moment, while the radiation pressure is the dissipative term that is used to slow down and cool the atoms. The dipole force, that guarantees the trapping of the atom, is dominant for large detunings, namely for $\delta \gg \gamma, \omega$:

$$\mathbf{F}_{\mathrm{dip}} = -\frac{\hbar \boldsymbol{\nabla} \Omega}{2} \frac{\Omega \delta}{\delta^2 + \frac{\gamma^2}{4} + \frac{\Omega^2}{2}} = -\boldsymbol{\nabla} \mathrm{U}_{\mathrm{dip}} \tag{3.8}$$

where $\mathrm{U}_{\mathrm{dip}}$ is the dipole potential

$$\mathrm{U}_{\mathrm{dip}} = \frac{\hbar \delta}{2} \log \left(1 + \frac{\frac{\Omega^2}{2}}{\delta^2 + \frac{\gamma^2}{4}} \right) \simeq \frac{\hbar \Omega^2}{4 \delta} \propto \frac{\mathrm{E}^2}{\delta} \propto \frac{\mathrm{I}}{\delta} \tag{3.9}$$

In equation (3.9) the logarithm can be expanded at the first order in Taylor series because we are considering the $\delta \gg \gamma, \omega$ regime. Moreover, we notice that the dipole potential is proportional to the square of the electric field over the detuning, and observing that the intensity I is proportional to the square of the electric field we obtain the last proportionality relation.

When the detuning becomes comparable to the energy difference between electronic levels, the two-level approximation breaks down and one has to resort to a more complete expression, taking into account the coupling of the ground state to different excited levels j:

$$U_{dip}(\mathbf{R}) = -\frac{3\pi c^2}{2\omega_0^3} \sum_j \left(\frac{\Gamma_j}{\omega_0 - \omega_j} + \frac{\Gamma_j}{\omega_0 + \omega_j} \right) \cdot I(\mathbf{R}) \tag{3.10}$$

where $I(\mathbf{R})$ is the spatial dependent intensity, ω_0 is the frequency of the laser beam, Γ_j and ω_i are the linewidths and the frequencies of all the considered transitions. The dipole potential can also be interpreted as a light-shift of the atomic levels that is induced by the non-resonant interaction.

The last step before obtaining an analytic expression for the dipole potential is to determine the intensity profile of the laser beam. It can be demonstrated that a Gaussian beam is a good description for a propagating laser beam [39]. The corresponding intensity profile is:

$$I(r,z) = \frac{2P}{\pi w^2(z)} \exp\left(-\frac{2r^2}{w^2(z)} \right) \tag{3.11}$$

where $r = \sqrt{x^2 + y^2}$ is the radial coordinate, z the axial coordinate, P is the power of the laser beam and w(z) is the beam size of the laser beam at coordinate z along the propagation axis. The beam size is a function of the beam waist w_0 and the Rayleigh length z_R that characterize uniquely the laser beam:

$$w(z) = w_0 \left(1 + \left(\frac{z}{z_R} \right)^2 \right)^{\frac{1}{2}} \quad , \quad z_R = \frac{\pi w_0^2}{\lambda} \tag{3.12}$$

The laser beam that we use for generating the optical tweezers is a Matisse Syrah manufactured by Spectra-Physics that is tuned to work around 813 nm, that is one of the magic wavelengths of Strontium atoms. This wavelength is one of the so-called *magic wavelengths* for the ultranarrow optical clock transition connecting the ground state $^1S_0$ and the metastable state $^3P_0$. For this specific wavelength the light shift is the same for both the levels, therefore the transition frequency is not shifted by the trapping light, which is highly beneficial for metrologic applications exploiting the $^1S_0 \rightarrow {}^3P_0$ transition. The laser beam coming out of its cavity is slightly elliptic, having the waists measured along the x and y axes $w_{0,x} = (1.024 \pm 0.009)$ mm and $w_{0,y} = (0.974 \pm 0.011)$ mm. The Rayleigh length is approximately $z_R = (4.15 \pm 0.07)$ m. The beam is deflected by the couple of acousto-optic deflectors in order to create multiple beams, and then is focused by a microscope objective to reduce the beam sizes to a micrometer lengthscale.

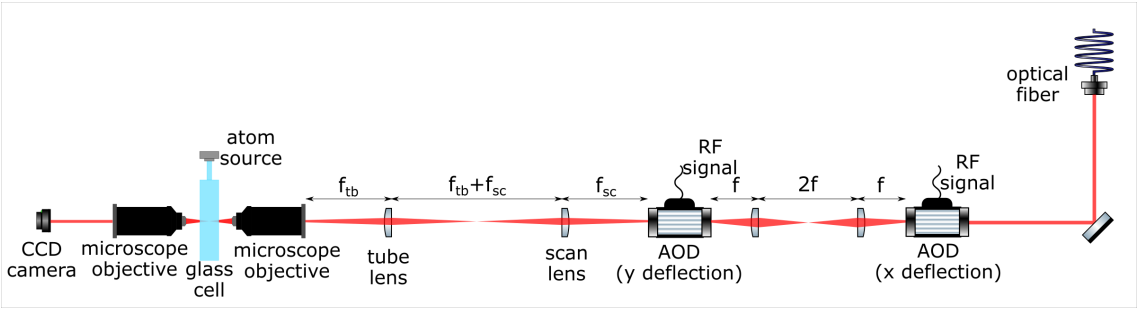

Figure 3.1: Schematic representation of the basic components of the apparatus for the creation of arrays of optical tweezers. A couple of crossed AODs can create several deflected beams covering the whole solid angle. The beams are focused via a microscope objective into a glass cell where the atoms are prepared in a MOT. A second microscope objective recollects the tweezers light.

The main components of the apparatus that will be used to create the OTs are presented in figure 3.1. The core of the apparatus is the glass cell, where atoms are trapped and cooled in a Magneto Optical Trap (MOT). The glass cell is engineered in such a way to provide the maximum optical access possible. The array of optical tweezers is superimposed to the MOT region in order to trap individual atoms. Given this optical setup, we can calculate the expected beam size of the tweezers and their separation after the microscope objective, in the glass cell. We can calculate these quantities as a function of the focal lengths f_{sc}, f_{tb} of scan and tube lenses (the pair of lenses before the objective in figure 3.1) and the effective focal length of the objective f_{obj}, also called working distance (WD). First of all, the divergence of a Gaussian beam with beam waist w_{in} has to be recalled:

$$\theta_0 = \frac{\lambda}{\pi w_{in}} \tag{3.13}$$

The beam size of the tweezer after being focused by the objective is then[1] [40]:

$$w_{tweez} = f_{obj} \cdot \theta_1 = f_{obj} \cdot \theta_0 \cdot \frac{f_{sc}}{f_{tb}} = \frac{\lambda f_{obj}}{\pi w_{in}} \frac{f_{sc}}{f_{tb}} \tag{3.14}$$

where θ_1 is the divergence of the Gaussian beam at the input of the objective that is expressed as a function of the divergence θ_0 before the scan-tube lenses system. Scan lens and tube lens focal lengths are used to calculate, in geometrical optics, the magnification/reduction of the divergence angle. The distance between a pair of tweezers generated at RF frequencies f_1 and f_2, such that the difference is Δf, is instead [40]:

$$d_{tweez} = 2f_{obj} \cdot \tan\left(\frac{\Delta\theta}{2}\right) = 2f_{obj} \cdot \tan\left(\frac{\Delta f \lambda}{2v_s} \cdot \frac{f_{sc}}{f_{tb}}\right) \tag{3.15}$$

[1] Equation (3.14) is valid in the case, always verified in our experimental conditions, that the Rayleigh length is much larger than the distance over which the beam propagates.

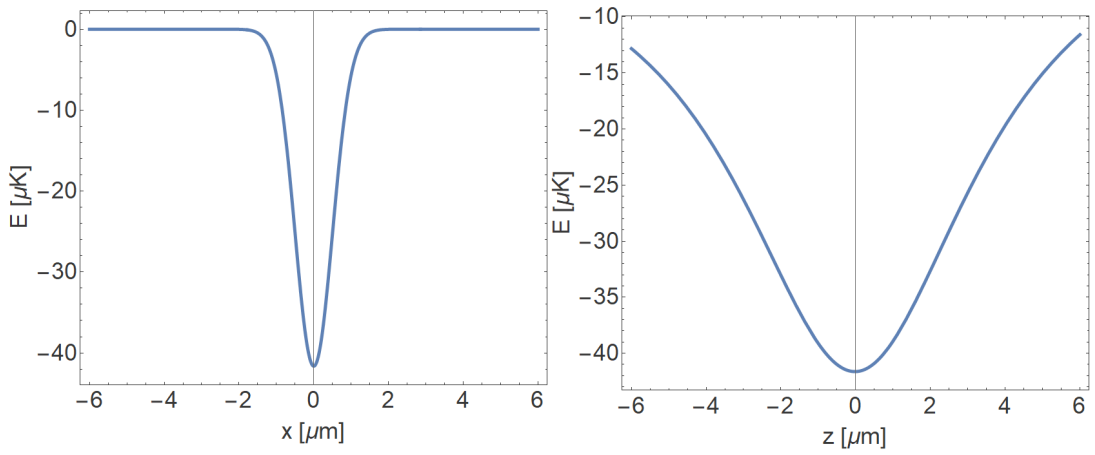

Figure 3.2: Example of the dipole potential plotted for the x and z directions.

In equation (3.15) $\Delta\theta$ is the angular separation of the pair of beams considered and it can be expressed as a function of Δf (see equation (4.6)) and of the scan-tube focal lengths ratio, while v_s is the sound velocity in the crystal medium of the AOD. The physical description of acousto-optic deflectors is treated in chapter 4.

Typical values for the optical systems are: λ=813 nm, w_{in}=1 mm, f_{obj}=5 mm, $f_{sc} = f_{tb}$=200 mm, Δf=1 MHz and v_s= 650 m/s. Substituting these values in the expressions above we obtain a tweezer size of w_{tweez}=1.3 μm and tweezers separation d_{tweez}=6.3μm. Feeding the w_{tweez} estimated value into equation (3.11), the intensity at the center of the trap, where the exponential factor is equal to 1, is I_0= $3.8{\cdot}10^8$ W/m^2 for a power P=1 mW. This huge intensity of the optical tweezers trap is the result of the tight focusing of the laser beams, and allows us to trap, with a little amount of laser power (for example 1 mW), atoms that have relatively high temperature of few μK. If 1 mW of laser power is enough for an optical tweezer that holds one atom, we may produce a few hundreds of traps within the same array, since the power is above 7 W right out of the laser cavity. In figure 3.2 the dipole potential in equation (3.10) is plotted along the x and z coordinates. The z direction denotes both the propagation axis of the beams that produce the optical tweezers and the gravity force direction. The y direction is not represented because it is equivalent to the x direction, being it perpendicular to the gravity force too. The parameters used to obtain this potential are P=1 mW, w_{tweez}=1 μm and λ= 813 nm. Only the two main transitions of Sr atoms were considered, the $^1S_0 \rightarrow ^1P_1$ and the $^1S_0 \rightarrow ^3P_1$, because they have the largest linewidths, and the trap depth is converted in a temperature scale (μK). Approximating the dipole potential to a harmonic trap, it is possible to calculate the harmonic trap frequencies. In table 3.1 we report a few values for the power depth of the trap P in mW, the dipole potential U in μK, and the corresponding trapping frequencies for the x (radial) and z (axial) directions in kHz. All the parameters are obtained for fixed λ=813 nm and w_{tweez}=1 μm.

P(mW)	U(μK)	ν_x(kHz)	ν_z(kHz)
0.1	-4.2	5.78	1.05
0.5	-20.8	12.9	2.36
1	-41.6	18.3	3.34
2	-83.3	25.8	4.73
5	-208.2	40.9	7.48
10	-416	57.8	10.6
20	-833	81.7	15.0

Table 3.1: Correspondence between the power of the tweezer P, its depth U and the trapping frequencies ν_x and ν_z

3.2 Advanced time-dependent trapping models

In this section I will describe two problems regarding the trapping and the transport of atoms. These two topics are relevant in the context of the rearrangement of the array that is performed to create a defect-free pattern. An array of static OTs can be created using the pair of crossed AODs by driving them with multiple frequency components RF signals. As the loading of this array with cold atoms will be non deterministic, we need to implement rearrangement techniques to obtain the desired pattern of trapped atoms, as discussed in subsection 2.1.1.

For 1D patterns the rearrangement consists in compacting only those tweezers that are filled to form a defect-free array of arbitrarily spaced OTs [15, 31]. To move one tweezer along the line, a frequency sweep is applied to the corresponding frequency component of the RF signal that drives the AOD. The sweep can be linear, resulting in a uniform rectilinear motion (URM) for the atom, but also more complicated equations for the tweezer's motion can be explored. The problem of finding the best equation for the transport of the atom is addressed in subsection 3.2.1.

For arbitrary 2D patterns this approach cannot be used, because only separable 2D patterns can be created with two orthogonal AODs, which forbid arbitrary movements of individual OTs. To overcome this limitation, one possible solution is the possibility of exploiting time-averaged potentials. This is the second time-dependent trapping model that we investigate in this chapter. In subsection 3.2.2 we consider a static tweezer whose amplitude is time-modulated to simulate the periodic switching ON/OFF of the trapping potential. In this case we study the constraints for the trapping of the atom as a function of the laser power generating the tweezer and the frequency at which the periodic switching of the potential is driven.

3.2.1 Simulation of moving Tweezers for the rearrangement

The transport of one atom in an optical tweezer is simulated on the software Mathematica. Since the tweezer is moved perpendicularly to the propagation axis z, that will correspond in the final experiment to the vertical direction, all the directions in the x-y plane are equivalent as they will not be affected by grav-

ity. This is a simplification because moving the tweezer along the x, y axis or any combination of them produces the same effects on the atom. The results obtained can thus be applied to the rearrangement in 2D patterns too, since in that case a single beam is deflected by the pair of crossed AODs and performs the rearrangement of the static array generated by an SLM. The transport can be decomposed in a series of moves along orthogonal x and y axes. The dynamic potential used in the simulation is derived from that in equation (3.10), considering a time-dependent intensity of the laser beam in equation (3.11) to get a time-dependent tweezer potential:

$$I_t(r,z,t) = \frac{2P}{\pi w^2(z)} \exp\left(-\frac{2\left[(x - x0(t))^2 + y^2\right]}{w^2(z)}\right) \tag{3.16}$$

Intensity depends on time via the time dependence of the coordinate x(t). The parameters describing the dipole potential are substituted with Strontium parameters taken from NIST and [41]. In particular, we consider just the two main transitions of Strontium atoms, the $^1S_0 \rightarrow ^1P_1$ line with λ=460.9 nm, $\Gamma \simeq 32.0$ MHz, and the $^1S_0 \rightarrow ^3P_1$ line with λ=689.4 nm, $\Gamma \simeq 2\pi * 7.6$ kHz. We then use the time dependent dipole potential

$$U_{dip,t}(r,z,t) = -\frac{3\pi c^2}{2\omega_0^3} \sum_j \left(\frac{\Gamma_j}{\omega_0 - \omega_j} + \frac{\Gamma_j}{\omega_0 + \omega_j}\right) \cdot I_t(r,z,t) \tag{3.17}$$

to define the force felt by the atom as minus the gradient of $U_{dip,t}(r,z,t)$ plus the gravitational potential:

$$\mathbf{F} = -\boldsymbol{\nabla} U_{dip,t}(r,z,t) - mg\hat{\mathbf{z}} = -\boldsymbol{\nabla} U(r,z,t) = (F_x, F_y, F_z) \tag{3.18}$$

The definition of the force components allows us to solve classically the motion of the atom along a radial (x) and axial (z) coordinates, while as for the y direction we consider the atom to be always at y=0. The equations to be solved are a pair of coupled differential equations, where m represents the mass of the Sr atom:

$$\begin{cases} m\ddot{z}(t) = F_z[x(t), 0, z(t)] \\ m\ddot{x}(t) = F_x[x(t), 0, z(t)] \end{cases} \tag{3.19}$$

In equation (3.16) we introduced a time-dependent redefinition of the center of the trap, x0(t). This expresses the tweezer position as a function of time. The simulations are performed for several x0(t), differing both in their mathematical function and boundary conditions, by solving classical coupled differential equations. Some tweezer-position functions x0(t) are shown in figure 3.3.

The distance between next-neighbouring tweezers in the array is typically of 5 up to 10 micrometers. The rearrangement procedure requires to transport atoms in the tweezers for a few sites, so we will consider the worst-case scenario where the atom has to be moved by 50 μm. In current experiments, the typical timescale for each transport is around 1 ms, so we assume this one as a target upper-bound value. In our simulations the total displacement is fixed to 50 μm, while

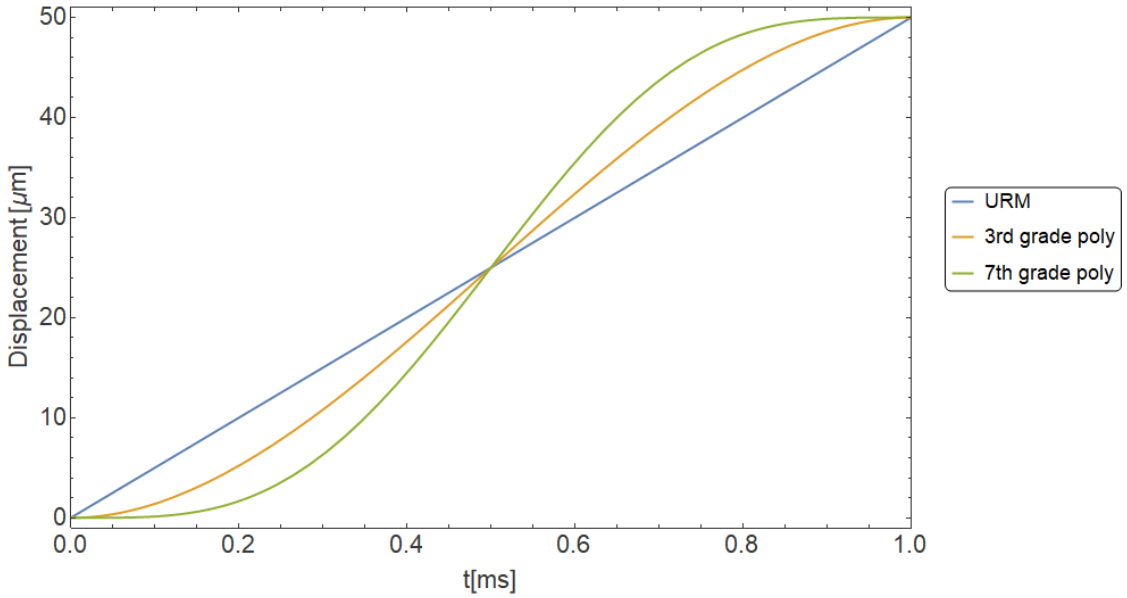

Figure 3.3: Three different tweezer-position function that produce in 1 ms a displacement of 50 μm. The blue curve represents a uniform rectilinear motion, while the yellow and green ones are a third-grade and a seventh-grade polynomials of t, respectively.

the time to perform the move is limited to be below 1 ms. This constraints the mean velocity of the motion of the tweezer position, that we will call v_{mean}, to be higher than 50 mm/s. For all the simulations, performed using several tweezer-position functions x0(t), we considered v_{mean} values in the range 50-200 mm/s. After solving numerically the differential equations (3.19) and obtaining the expressions for x(t) and z(t), we calculate their derivatives $\dot{x}(t)$ and $\dot{z}(t)$. Then we calculate the kinetic and potential energies during the transport by substituting x(t), z(t) and their derivatives in equations (3.20).

$$E_k(t) = \frac{1}{2}m\dot{x}^2(t) + \frac{1}{2}m\dot{z}^2(t) \qquad E_p(t) = U[x(t), 0, z(t)] \tag{3.20}$$

where U is the energy potential introduced in the force definition (3.18). The criterion that we used to quantify the goodness of the results is the value of the energy increase between the beginning and the end of the motion. The energy increase is a consequence of the work of non-inertial forces that are applied to the atom in the non-inertial frame of the moving trap.

$$\Delta E(t_i, t_f) = E_k(t_f) + E_p(t_f) - \left[E_k(t_i) + E_p(t_i)\right] \tag{3.21}$$

Solution for the atom at rest in the center of the trap

The first tweezer-position function considered for our simulations exploited an uniform rectilinear motion (blue plot in figure 3.3). The boundary conditions for the set of differential equations (3.19) are x(0)=z(0)=0 m and $\dot{x}(0) = \dot{z}(0) = 0$ m/s. The energy increase values are plotted as a function of the transport mean

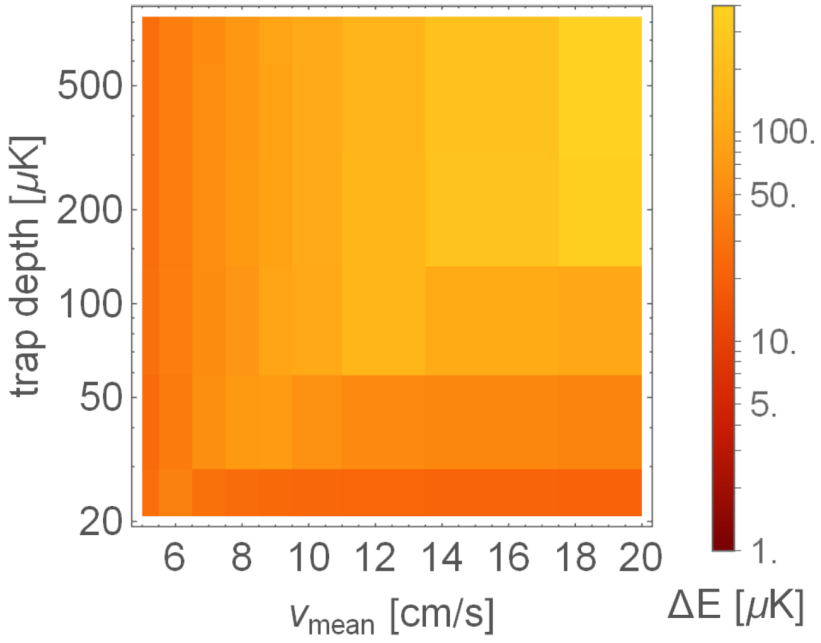

Figure 3.4: Energy increase calculated for the atom subject to a URM motion. The initial conditions are those of an atom at rest in the center of the trap.

velocity v_{mean} and the power of the tweezer P (see equation (3.16)) in the logarithmic colour plot in figure 3.4. As stated above, higher transport speeds for a fixed target distance means that the move is performed in a time smaller than 1 ms. Generally, figure 3.4 shows that the transport is better for small speeds because under these conditions the atom gets a small energy increase due to the motion. The value estimated for ΔE is quite independent on the power of the tweezer, except for the lower lines in the plot that seem to be good parameter values, even better than the ones obtained for low velocities. Actually, the atom is probably lost for those combination of parameters, since that the trap depth was too low (for example the depth of the 0.5 mW trap is just 20 μK) and the transport velocity too high, and the low energy increase obtained by the simulation may be caused just by an error in the numerical evaluation. Anyway, the smallest energy increase is above 26 μK and can be obtained for the smallest velocity available. Fixing a target distance and a maximum time of 1 ms to perform the transport results in a minimum mean velocity for the motion. The fact that also higher speed values are available, even though in general this provokes an higher increase of energy, tells us that we can both transport the atom further away in the same time (1 ms) and transport the atom in a smaller time to the same target distance (50 micrometers). This consideration is valid also for the following plots.

The uniform motion is of course the easiest transport that we can simulate, but this is probably not a good choice since the atom is subject, both at the beginning and the end of the motion, to strong impulsive inertial forces due to the sudden acceleration imposed by the motion of the tweezer.

The second tweezer-position function that we implemented in the simulation

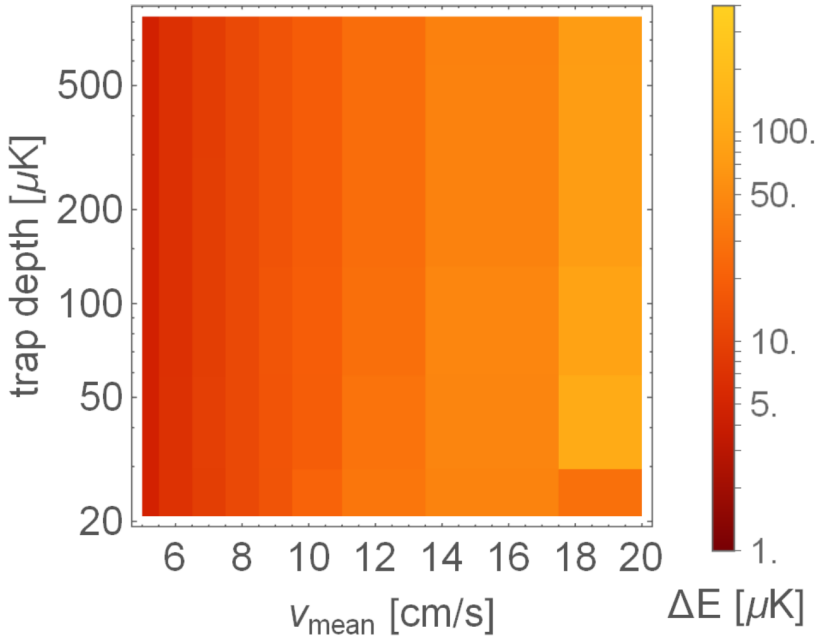

Figure 3.5: Energy increase calculated for the atom subject to a third grade polynomial motion. The initial conditions are those of an atom at rest in the center of the trap.

is a third-grade polynomial (yellow line in figure 3.3) that tries to take into account these physical observations.

$$x(t) = A\left(3\left(\frac{t}{t0}\right)^2 - 2\left(\frac{t}{t0}\right)^3\right) \tag{3.22}$$

where A=$50*10^{-6}$ m and t0=10^{-3} s are the normalizations needed to scale the equation between the desired space and time values. The above equation is derived in [42], imposing to have zero velocity at the initial and final times. This excludes the possibility to have first order power of t. Moreover, the boundary conditions x(0)=0 and $x(t_0 = 10^{-3}) = 50*10^{-6}$ m allow us to determine uniquely the third-grade solution reported in equation (3.22).

The results of the simulation that implemented equation (3.22) are reported in figure 3.5. This plot is similar to the one in figure 3.4. In particular, the time normalization t0 was tuned to values lower than the upper bound (1 ms) in order to obtain the same mean velocities that were used for the first simulation. Comparing the results, the second equation describing the motion of the tweezer gives smaller increases in the final energy, and the effect of the transport is almost independent on the trapping depth. The ΔE values on the left side of the histogram, converted in temperature values, are all below 5 μK, providing an improvement with respect to the URM simulations. The energy increase is limited also for large transport speeds ($\Delta E < 110$ μK) proving the validity of this transport method.

The problem of finding the best transport equation for an atom falls in the field of optimal control algorithms. Indeed, much more complicated equations have been developed finding the best parameters with variational algorithms. We tried to implement one last equation (the green plot in figure 3.3) that was

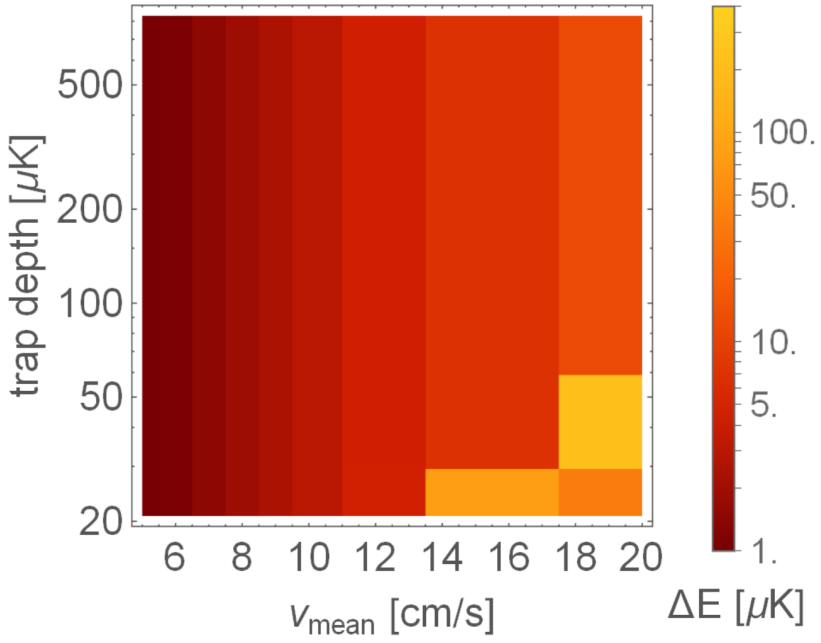

Figure 3.6: Energy increase calculated for the atom subject to a seventh grade polynomial motion. The initial conditions are those of an atom at rest in the center of the trap.

derived and optimized in [43]. This equation, smoother than the previous ones, is expressed in terms of the variationally optimized parameters as:

$$x(t) = A\left(35\left(\frac{t}{t0}\right)^4 - 84\left(\frac{t}{t0}\right)^5 + 70\left(\frac{t}{t0}\right)^6 - 20\left(\frac{t}{t0}\right)^7\right) \tag{3.23}$$

where A and t0 are the same normalization parameters introduced in equation (3.22). The time normalization t0 is tuned to values corresponding to different mean velocities in this case too. The plot showing the energy increase as a function of the power and mean velocity parameters is shown in figure 3.6. This method proves to be a further improvement with respect to the first two equations discussed. Neglecting the three boxes in the right bottom of the plot, for which probably computational errors in the simulations came up, the energy increase ranges from minimum values around 0.7 μK for small speeds to maximum values that are anyway limited below 12 μK for high speeds. This last method is thus the most effective because it only slightly changes the energy of the atoms.

Solution for the atom with thermal initial speed and position

We decided to repeat the simulations described above also in the case where the atom at the beginning of the transport process has already nonzero speed v0=0.03 m/s and it is away from the center of the trap for an amount $\delta = 0.5 * w_T$, where w_T is the tweezer's waist. In the Maxwell-Boltzmann thermal distribution for a MOT at 1 μK^2 the 97.7% of the atoms are contained below this v0 value, so

[2]This Doppler cooling temperature value was achieved in [36] for a Sr apparatus similar to the one described here.

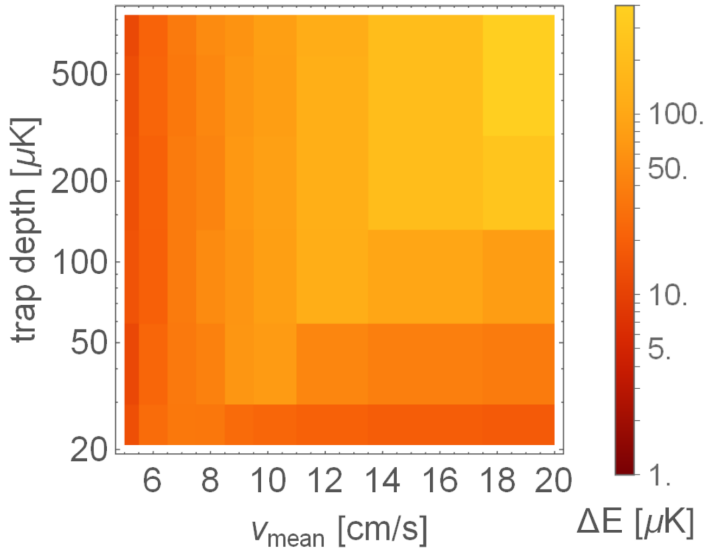

Figure 3.7: Energy increase calculated for the atom subject to a uniform motion. The initial conditions are v0=0.03 m/s and $\delta = 0.5 * w_T$.

this is a worst-case scenario. Furthermore, we introduce a consistent displacement of the atom with respect to the center of the tweezer of half its waist. In this second set of simulations we used again the energy increase as cost function (3.21). The difference is that now the atom has a nonzero initial energy, both kinetic and potential. Differently from the previous simulations, for which the total energy of the atom was equal to the energy increase, to get the total energy in this case we have to add to ΔE the initial energy, that is constant and equal to $E_c(t_i) + E_p(t_i) \simeq (4.7 + 60.7)$ μK=65.4 μK. The comparison between the first and the second set of simulations is important to find out if there is a clear advantage in cooling the atoms in the trap (see section 2.3) before or after the transport. The atom with nonzero initial position and velocity represents the case in which we first perform the rearrangement and then cool the atoms, although quantum mechanically even the ground state has nonzero energy, while the atom at rest represents an approximation for the latter case. In the case of the simulation implementing an uniform rectilinear motion, the energy increase is shown in figure 3.7. The plot is similar to the corresponding simulation performed considering the atom at rest (figure 3.4). Slower transports result in a small ΔE around 12 μK, while also in this case faster movements result in a higher energy increase. The third-grade polynomial used to obtain the results in figure 3.8 allows for an improvement with respect to the uniform rectilinear motion of the tweezer's position, like in the comparison between previous results in figures 3.4 and 3.5. Now the estimated values for ΔE range from 6 to 115 μK, from the left to the right side of figure 3.8. In figure 3.9 we see the high effectiveness of the equation (3.23). This technique, applied to an atom that is already moving, gives for many parameter values a ΔE smaller than 1 μK. The yellow areas for which the atom received a large energy increase at the end of the transport, differently from all the other combination of parameters, may be affected by errors during the simu-

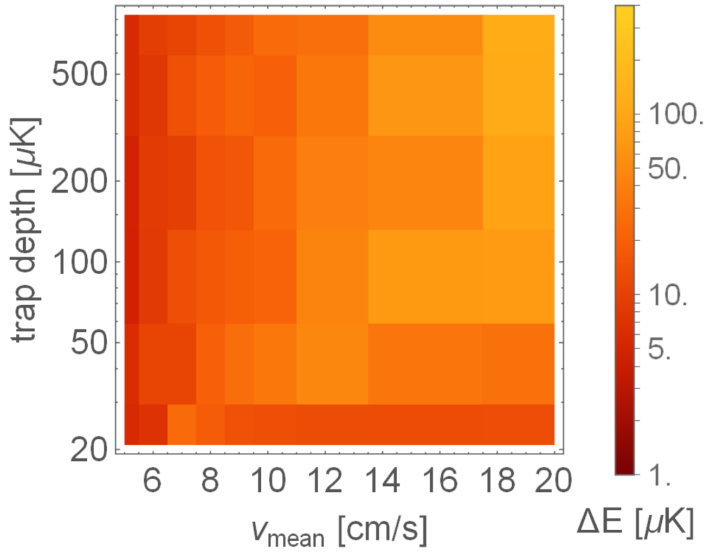

Figure 3.8: Energy increase calculated for the atom subject to a third-grade polynomial motion. The initial conditions are v0=0.03 m/s and $\delta = 0.5 * w_T$.

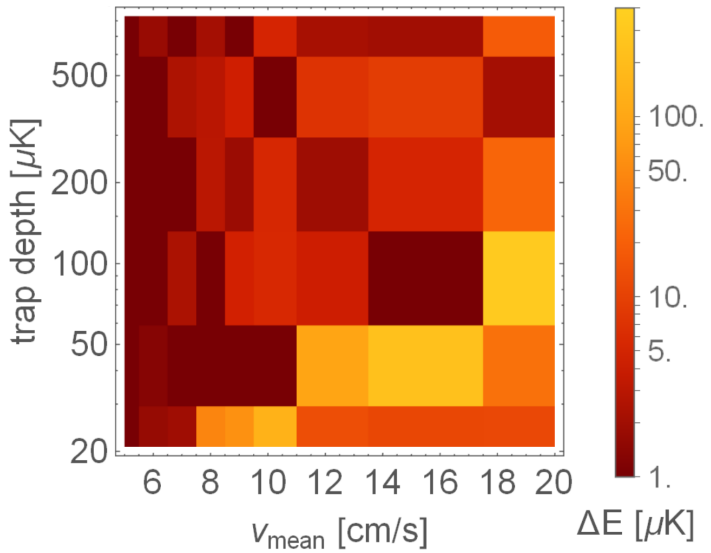

Figure 3.9: Energy increase calculated for the atom subject to a seventh-grade polynomial motion. The initial conditions are v0=0.03 m/s and $\delta = 0.5 * w_T$.

lation run. Another possibility is a particular resonance of the oscillations of the atom in the trap with the initial velocity v0 that results in a much higher energy increase with respect to all the others obtained in the plot.

By comparing the first set of simulations with the second one, we see that the plots obtained for the same tweezer motion are similar, this meaning that the effect of a particular way of transporting the atoms is not much affected by the energy the atom has at the beginning. There are many larger differences among the results of simulations that we obtained using different functions for the motion of the tweezer. The total energy of the atom in the second set of measurements is of course higher because we have to consider the sum of δE and the initial energy (approximately 65 μK). In conclusion, it may be convenient to perform the cooling in the trap after the transport since the available parameter regions are the same in the case of the atom at rest and in that of the moving atom. Moreover, the heating caused by the transport difficultly will be negligible. It is so only in the left side region in figure 3.6 for atoms at rest.

3.2.2 Simulation of a periodic time-dependent Tweezer (Time-Averaged)

In this section we present the simulation of a Sr atom, treated as a classical particle as in section 2.1, that is subjected to a time-averaged potential. This technique exploits the very fast response of the devices in use, the AODs. We start again from the dipole potential in equation (3.10), although this time the modulation is not a time-dependent position of the trap's center, but a periodic function that multiplies the dipole potential. Note that the modulation simulates the periodic switching on/off of the tweezer that jumps over many sites in one period, but it doesn't affect the gravitational potential. Hence, when the tweezer jumps onto a different site, the atom that we are observing starts to fall under the gravitational force. In this set of simulations we want to determine under which parameter values the time-averaged potential trapping works, i.e. the atom remains trapped at times much longer than the modulation period. We quantify the goodness of the results by calculating the energy increase, as done also for the transport of the atom. The dipole potential for the time-averaged potential has an explicit time dependence that is contained in the modulation:

$$U_{\text{timeavg}}(r,z,t) = -\frac{3\pi c^2}{2\omega_0^3}\sum_j\left(\frac{\Gamma_j}{\omega_0-\omega_j}+\frac{\Gamma_j}{\omega_0+\omega_j}\right)\cdot I(r,z)\cdot \text{mod}(t,\nu) \tag{3.24}$$

where I(r,z) is the intensity of the tweezer expressed as function of the radial and axial coordinate and the modulation mod(t,ν) is a function of time for a specific frequency value ν. This frequency value is the one at which the modulation is repeated periodically. Ideally, the modulation would be a square wave that represents a sudden switch of the deflected beam accounting for the switch from one RF frequency to another (and so from one position in the array to the following one). Anyway, the AOD has finite rise and fall times and a square wave does not represent a physical modulation.

The function that we used to represent the modulation was obtained directly from measured signals, as discussed in subsection 4.4.4. In figure 3.10 we anti-

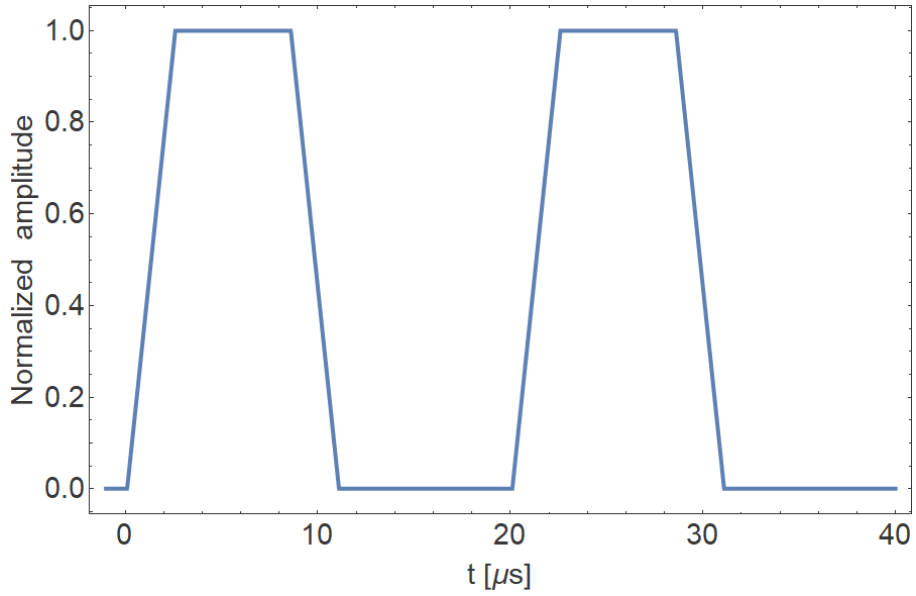

Figure 3.10: Example of the modulation function mod(t,ν) for ν=50 kHz and a rise time of ~ 2.5 μs.

cipate the result of the next chapter to describe this simulation. The modulation is expressed as a piecewise function with two horizontal segments standing for the ON period and the OFF period of the tweezer, and two oblique segments that represent the rise and fall of the signal. The slope of these segments is determined by the finite rise time of the AOD device, as pointed out in chapter 4. As for the example in figure 3.10, the beam size of the laser is around 1 mm and the corresponding rise time is approximately 2.5 microseconds. Note that the duty cycle of the function is 50%, meaning that the modulation mod(t,ν) switches the deflected beam between a single pair of positions[3].

The procedure for this simulation is the same used in the simulations of the transport of atoms. We calculate the force as:

$$\mathbf{F}_{\text{timeavg}} = -\boldsymbol{\nabla} U_{\text{timeavg}}(r,z,t) - mg\hat{\mathbf{z}} = -\boldsymbol{\nabla} U(r,z,t) = (F_x, F_y, F_z) \tag{3.25}$$

where now the contribution of the dipole force is modulated in time by mod(t,ν) and the gravity force is always present. The system of differential equations is the same as equation (3.19), although they obviously differ for the expressions of the force components F_x and F_z. The results of the simulations are plotted in logarithmic color plots where the energy increase ΔE (defined as in (3.21)) is plotted as a function of the power depth of the tweezer and the frequency of the modulation function ν. The energy scale of the plots is converted again in μK. The important difference between the transport simulations and the time-averaged ones is that, while the first ones evaluate numerically the motion equations of the atom for a time of the order of 1 ms, in the second case we want to observe the evolution of the atom for hundreds of ms, making it a more challenging task. In

[3]Actually, the modulation is applied in phase to both the crossed AODs, in such a way that the two tweezer positions over which the dipole trap is shared, can be any couple of points in the plane.

particular, we simulate the time-averaged potential trapping to last 200 ms, that is a typical time for one experimental cycle. The atoms initially loaded randomly in the array (1 ms) are imaged one first time (30 ms) to determine the sequence of moves for the reordering (50 ms). After the reordering a second imaging stage (30 ms) is needed to check whether the reordering worked properly or not. Then the Rydberg excitation takes place and finally a third imaging stage (30 ms) allows for the detection of the atomic state [36]. The overall timescale should then be around 200 ms.

Time-averaged potential for an atom at rest in the center of the trap

The sequence of the simulations is similar to that discussed in subsection 3.2.1. We started to simulate the effect of a time-averaged potential onto an atom characterized by boundary conditions v0=0 m/s and δ=0 m. This is an approximation for a low-energy atom. The size of the laser beam at the position of the AOD considered for this simulation is 1 mm, thus resulting in a rise time of the signal relative to the deflected beam of approximately 2.5 μs. This dependence will be shown in section 4.4. The size of the tweezer in correspondence of the atoms is instead considered to be 1 μm.

We chose a set of switching frequencies ν from 10 kHz to 250 kHz and for each of them we derived a function like the one plotted in figure 3.10 following a procedure that is discussed in chapter 4. Moreover, the simulations are repeated for different power depth values P (see equation (3.11)), from 500 μW to 20 mW. In figure 3.11 we see a clear distinction between two regions of the plot. The red boxes are those for which the atom is lost and essentially falls for 200 ms under the effect of the gravity. The energy increase in these cases is huge and the final kinetic energy is that of a free falling particle. The rest of the histogram with violet, blue and green boxes, is a region of parameters (the trap depth and the frequency of the modulation) for which the atom is kept in the trap for all the time. The energy increase in this case is small, less than 100 nK in many cases. This is a very promising result because, except for ν=10 kHz that is a condition under which the atom is always lost, there is a very large range of parameters that can be exploited to perform a time-averaged potential trapping. The first column in figure 3.11 shows that for ν=10 kHz the modulation is too slow even for an atom at rest, because during the time in which the trap is off the atom has enough time to fall and escape the tweezer. The reason for that is probably that in this case the switching frequency becomes compatible with the trapping frequencies of the atom in the trap (see table 3.1). The red boxes at the top of the histogram indicate us that, for large power values, even the frequencies up to 120 kHz are unsuitable for the time-average method. The reason for that is probably that for increasing power depths the tweezer kicks the atom out of the trap when the potential is quasi instantaneously switched on.

We decided to test this technique also under different experimental conditions. We introduced in the optical path a telescope to reduce the beam waist entering the AODs by a factor of 2. The resulting measured beam waist is around 500 μm, thus providing a faster rise time $\tau \simeq 1.25$ μs, as it will be shown in sub-

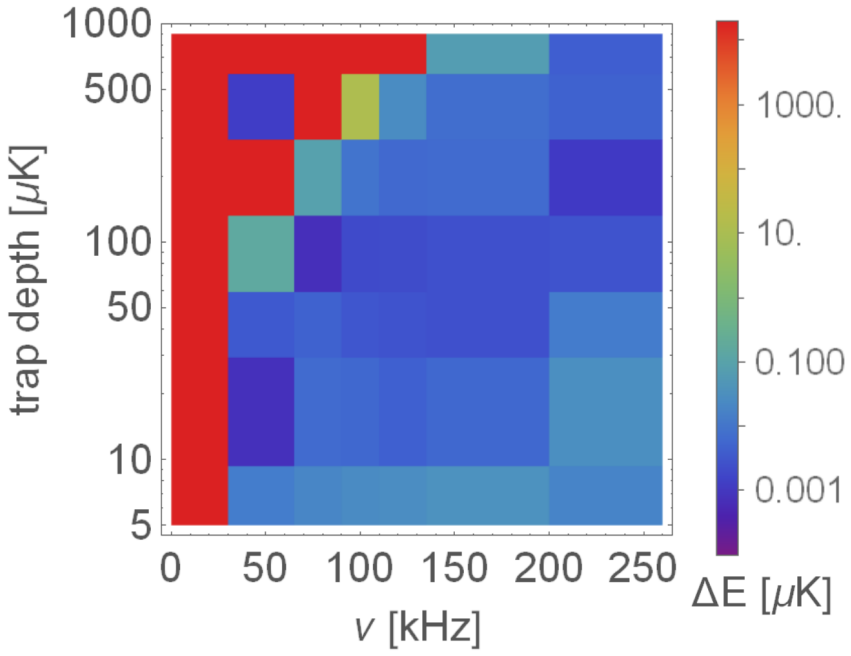

Figure 3.11: Energy increase calculated for the atom subjected to a time-averaged potential. The initial conditions are v0=0 m/s and δ=0 m. The energy scale is converted into a temperature scale (μK).

section 4.4. The size of the tweezer considered at the position of the atoms is 1 μm. Modulation functions similar to that in figure 3.10 were obtained for the reduced beam too, although in this case the slope of the oblique segments is almost doubled because of the faster response times. The results of these simulations are reported in figure 3.12 again in the form of a logarithmic plot. The region of parameters where the atoms are successfully trapped coincides with the region found in the simulation in figure 3.11, and also the numerical values for the energy increase ΔE are quite similar. There is a central region of the histogram (the purple boxes) in which the time-averaged technique proves to be extremely effective, since the energy increase estimated from the simulations is of the order of the nK. Anyway, comparing these two plots we see that they are almost equivalent and the faster dynamics in the AOD in the case of the smaller laser beam does not give large advantages.

Time-averaged potential for a thermal atom

We decided to repeat the scheme used for the simulations of the atom's transport and to perform a new set of simulations with different starting conditions for the atom. The atom is considered to have, at the beginning of the simulation, a velocity v0=0.03 m/s and a displacement $\delta = 0.5 * w_T$, and these parameters are the boundary conditions for the set of coupled differential equations describing the evolution of the particle. The choice of these parameters is motivated following the argument described in subsection 3.2.1. Also in this case, the criterion for

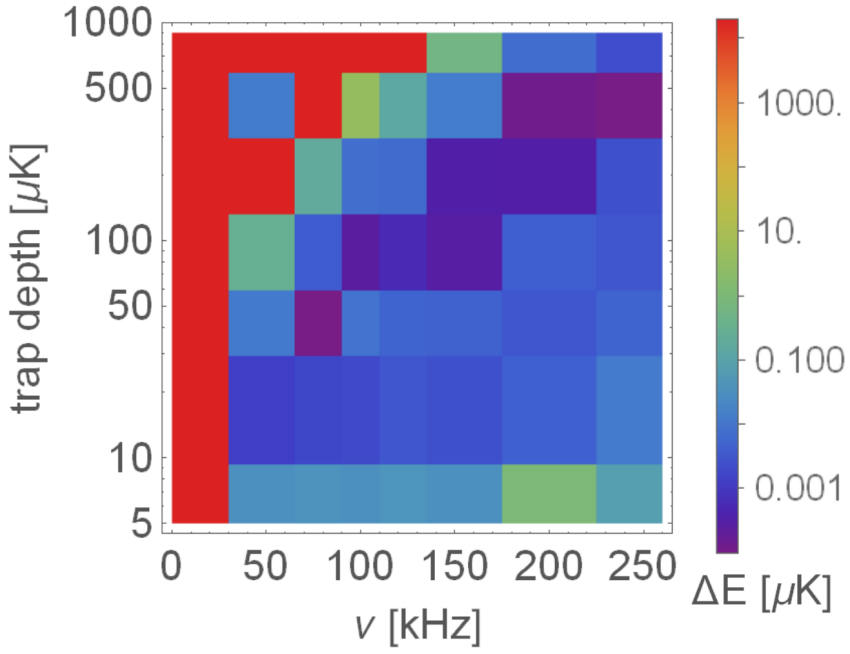

Figure 3.12: Energy increase calculated for the atom subject to a time-averaged potential in the case of a reduced beam waist at the position of the AOD. The initial conditions are v0=0 m/s and δ=0 m. The energy scale is converted in temperature scale (μK).

the goodness of the time-averaged trapping is the value of the final energy, the sum of kinetic and potential energies, subtracted by the initial energy. The sum of kinetic and potential energy at the beginning of the simulation is again $E_i \simeq 65$ μK, so to obtain the total final energy this value has to be added to the energy increase ΔE. Also in this case, we performed the simulation using two different modulating functions, the one derived for the large laser beam (1 mm) and the one for the reduced beam (0.5 mm). The results of these simulations are reported in figure 3.13. Figure 3.13a shows the effect of a time-averaged potential where the modulation is relative to the 1 mm laser beam, while in figure 3.13b we used the modulation for the reduced laser beam. The two plots are presented together to point out the similarities and differences: the region of parameters useful for trapping the atom (blue, purple and green) are quite similar but the reduced beam seems to offer a small advantage. In both the cases switching frequencies ν up to 50 kHz are not useful because the atom is always lost (red boxes). Also in this case high trap powers are unsuitable because the kick the tweezer gives when it is suddenly turned on is too high and the atom can be lost. As for the low trap depths, the simulations relative to the large beam tell us that the minimum power depth for trapping the atom is 1 mW and below this value the atom is lost. In the second case there is only one combination of parameters at ν=80 kHz and ν=90 kHz for which P=0.5 mW is enough. Note that the plot in figure 3.13b is realized performing the simulation also for ν=200 kHz, while in figure 3.13a the last two values were ν=150 kHz and 250 kHz, so the plots appear slightly different only because of the binning realized by the software.

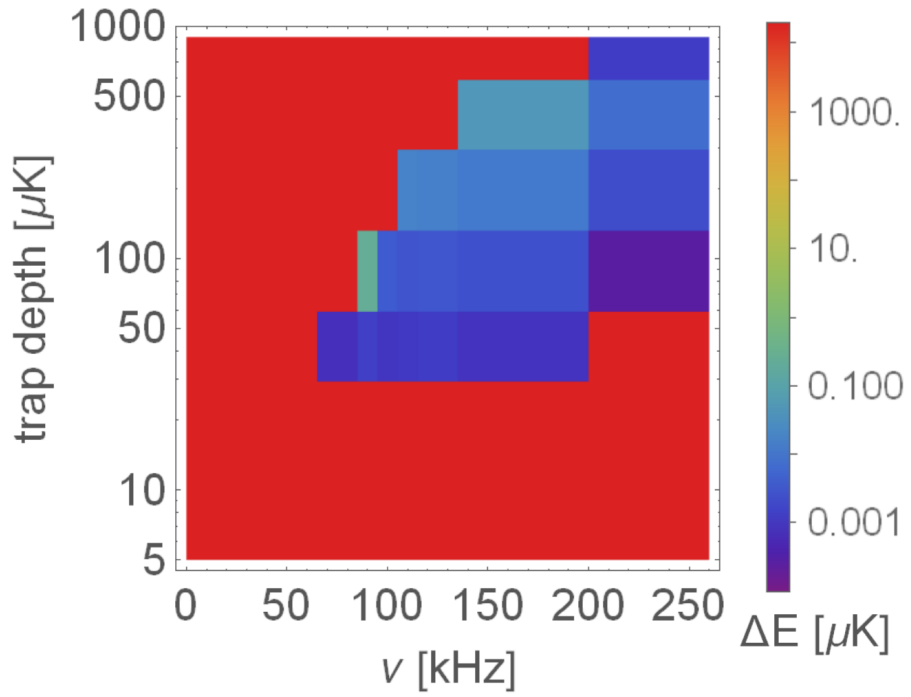

(a) Time-averaged potential using a laser beam of 1 mm waist at the position of the AOD (corresponding rise time of 2.5 μs) and considering the atom with v0=0.03 m/s and $\delta = 0.5 * w_T$.

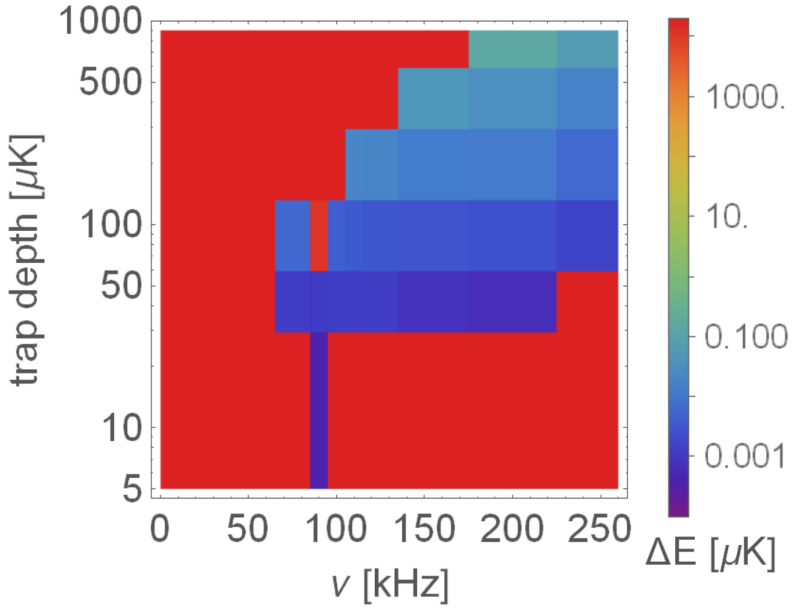

(b) Time-averaged potential using a laser beam of 0.5 mm waist at the position of the AOD (corresponding rise time of 1.25 μs) and considering the atom with v0=0.03 m/s and $\delta = 0.5 * w_T$.

Figure 3.13: Comparison of the time-averaged trapping technique exploiting two different beam sizes of the laser that is deflected by the AODs.

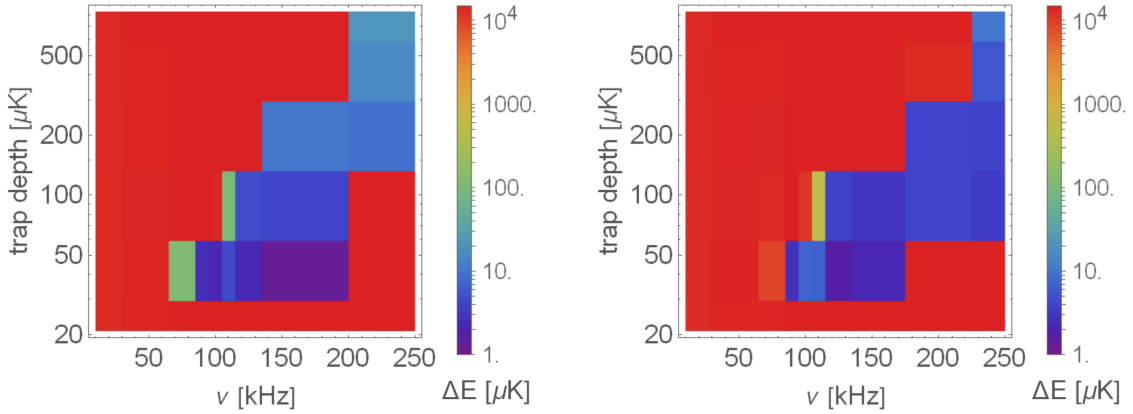

(a) Time-averaged potential using a laser beam of 1 mm waist and considering the atom with v0=0.03 m/s and $\delta = 0.5 * w_T$. The duty cycle of the modulation is 33%.

(b) Time-averaged potential using a laser beam of 0.5 mm waist and considering the atom with v0=0.03 m/s and $\delta = 0.5 * w_T$. The duty cycle of the modulation is 33%.

Figure 3.14: Comparison of the time-averaged trapping technique exploiting two different beam sizes of the laser that is deflected by the AODs.

The results of the simulations are promising because there is still a large region where the heating caused by the time-averaged potential is below 5 μK even for a thermal atom with an initial displacement from the center of the trap.

Time-averaged potential with unbalanced duty cycle

Up to now the simulations of a time-averaged potential all regarded the situation in which the duty cycle is 50% and so it allows to switch the tweezer over just a couple of positions. To conclude this series of simulations, we report the results of the trapping with a time-averaged potential where the modulation function mod(t,ν) is periodic with 33% duty cycle. Differently from the modulation in figure 3.10, for which the on and off time were approximately equal to 50% of the period, in this case we consider the on time to be the 33% of the period. The shape of the piecewise functions used are still the same derived from measured traces for the balanced case. This represents a modulation at the same ν investigated in the previous cases, but now in one period T=$2\pi/\nu$ the tweezer is shared over three different positions. In figure 3.14 the plots related to these simulations are reported, both considering the use of the large beam (figure 3.14a) and the use of the reduced one (figure 3.14b). The range of parameters that allow for the trapping is reduced, and this is consistent with the fact that now the time over which the tweezer is off is doubled with respect to the simulations shown in figure 3.13. The region of good parameters for the large and small beams, in figures 3.14a and 3.14b, respectively, are slightly different but in both the cases combinations of parameters giving ΔE smaller than 10 μK are available. The reduction of the region of parameters suitable for the trapping of atoms in time-averaged optical tweezers suggests that this technique can be applied to small-size arrays only. In particular, the length of the total period over which the time-

averaged tweezer runs across all the sites of the array is limited, since we want the atom to be recaptured at every period. The other important constraint is the finite rise time of the deflected beam, that will be discussed in chapter 4.

3.3 Quantum model

All the previous simulations were classical, because the computational power requested for simulating the evolution of the atom's wavefunction under the action of a Hamiltonian with complex time dependence was too demanding. In this section, we will study the quantum-mechanical evolution in a very simplified case, that of a *release and recapture* process, which is, however, highly relevant to the experimental implementation of Rydberg experiments. In most protocols, the Rydberg dynamics is initiated after releasing the atom from the optical tweezer, i.e. during a free-space evolution of the atom wavefunction, then the trap is switched on again during the detection phase. Of course, it is crucial not to lose the atom during the Rydberg dynamics, i.e. the *recapture* probability must be the closer to 1 as possible. In this context, we simulated the free space evolution of the wavefunction describing the atom and then calculated the probability to recapture it in the tweezer. The eigenstates of the atom in the Gaussian potential were approximated to the eigenstates in a harmonic potential, that we report as a function of the spatial coordinate and the quantum number n.

$$\psi_{\text{h.o.}}(x,n) = \frac{1}{\sqrt{2^n n!}}\left(\frac{m\omega_x}{\pi\hbar}\right)^{\frac{1}{4}} e^{-\frac{m\omega_x x^2}{2\hbar}} H_n\left(x\sqrt{\frac{m\omega_x}{\hbar}}\right) \tag{3.26}$$

H_n is the nth Hermite polynomial, ω_x is the trap frequency along the x direction, m is the mass and $\hbar$ is the reduced Planck's constant. The same expression can be written for the y and z coordinates too. In the following we consider the x coordinate as the radial one and the z as the axial. The two directions differ because the confinement is much tighter in the radial coordinate than the axial. In particular we consider an optical tweezer with power depth P=2 mW and waist $w_T = 1\ \mu$m, corresponding to a trap depth of $-83.3\ \mu$K and trapping frequencies $\omega_x = 2\pi \cdot 25.8$ kHz $\omega_z = 2\pi \cdot 4.7$ kHz. This means that in the harmonic oscillator approximation the radial coordinate has more than 60 energy levels available, while the axial coordinate has more than 300 levels. When the atom is released, we calculate the time evolution in free space using the integral form [44] in equation (3.27):

$$\psi(x,t) = \sqrt{\frac{m}{2\pi i\hbar t}} \int \psi(x',0) e^{-\frac{m(x-x')^2}{2i\hbar t}} dx' \tag{3.27}$$

By applying this propagator to the harmonic oscillator eigenfunctions we get their time evolution. It is important to consider now two distinct cases, the first for a system at zero temperature and the second at finite temperature (in our case we use the MOT temperature T=1 μK). At zero temperature only the ground state of the harmonic oscillator trap will be occupied and we have to calculate just one propagator. After a time t the trap is switched on again and the recapture probability is calculated by projecting the evolved wavefunction to the eigenfunctions

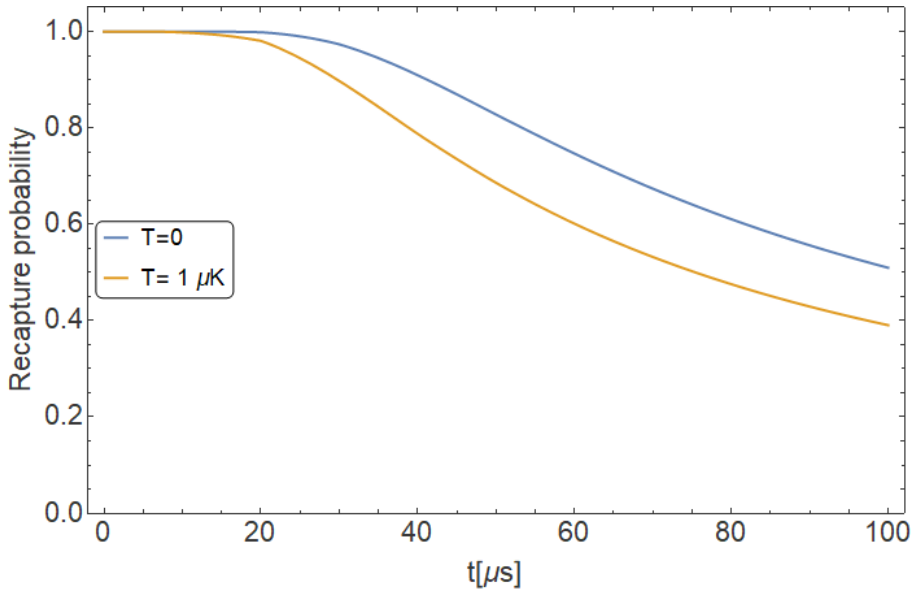

Figure 3.15: Recapture probability as a function of time in the case at zero temperature and finite temperature.

of the harmonic oscillator. As for the radial direction we have approximately 60 levels contained in the trap and we obtain a coefficient c_i for the projection of the evolved wavefunction to all of these levels. The square modulus $|c_i|^2$ gives the probability to find the atom in the i-th energy level, so the total probability to recapture the atom in any of the levels of the trap is given by:

$$P_{\text{recapture}}(T = 0) = \sum_{i}^{N} |c_i|^2 \tag{3.28}$$

We consider here a simplified version of the problem, taking into account the time evolution for just one spatial coordinate. In particular, we consider the evolution for one of the radial coordinates, having a larger trapping frequency.

In the blue plot in figure 3.15 the probability to recapture the atom at T=0 is plotted versus the release time. This plot presents a range of release times up to 20 μs for which the atom is always recaptured. The temperature dependence is nontrival, so we had to repeat the procedure described above for different initial states to calculate the recapture probability for different evolution times.

In the finite temperature case the atom is not only in the ground state of the trap, but it can be found in the excited states as well with a probability given by the Boltzmann distribution:

$$p_n = \frac{1}{Z} \exp\left\{-\frac{E_n}{k_B T}\right\} \qquad E_n = \hbar\omega_x \left(n + \frac{1}{2}\right) \tag{3.29}$$

where p_n is the probability to find the atom in the n-th level whose energy is described by E_n for a harmonic oscillator, and Z is the partition function. For the simulation of the recapture probability at T=1 μK we impose a cutoff to n=5,

hence considering only the ground state and the first five excited states as starting wavefunction. We chose the cutoff to neglect all the initial states with probability $p_n < 2 * 10^{-3}$. The time evolution of the harmonic oscillator eigenstates from n=0 to n=5 are calculated using (3.27) again and each of them is projected onto the trap eigenfunctions to obtain the coefficients c_{ij}, where the j index runs over the six initial eigenstates and i over the final ones. The recapture probability is now a sum weighted by the p_n coefficients:

$$P_{\text{recapture}}(T = 1\,\mu K) = \sum_{j=0}^{5} \sum_{i}^{N} |c_{ij}|^2 \tag{3.30}$$

This probability plotted in yellow in figure falls down faster than in the zero-temperature case. The maximum release time that allows for the recapture with P≃1 is reduced to approximately 10 μs, but the important aspect is that it is still possible to recapture the atom if this is released for a time small enough.

Obviously, in the 3D case the recapture probability will be smaller, because the free-space evolution contributes for all the three coordinates. Assuming a 3D isotropic harmonic oscillator and neglecting the effect of the gravity, the total wavefunction can be factorized:

$$\psi_{0,3D}(x, y, z) = \psi_0(x)\psi_0(y)\psi_0(z) \tag{3.31}$$

Since every one dimensional wavefunction evolves independently following the time evolution described in equation (3.27), also the integral that gives the overlap between the evolved 3D wavefunction and the eigenstates in the harmonic oscillator can be factorized, thus obtaining the product of three equivalent contributions. Following this qualitative argument, the plot of the recapture probability in the 3D case could be obtained by the one in figure 3.15 just by taking its third power. Hence, if the 1D recapture probability were of 90%, the corresponding recapture probability should be this probability cubed, that is the 73%.

Chapter 4

Acousto Optic Deflectors

Acousto Optic Deflectors are devices that make use of the interaction of light and acoustic waves in crystalline materials to deflect an incoming laser beam at an output angle that depends on the frequency of the acoustic wave [45, 46]. An AOD consists of mainly two elements, a piezoelectric transducer and a crystal. These two elements are bonded in such a way that a vibration generated from the transducer propagates along the crystal. A RF signal inputs the piezoelectric transducer via an RF matching circuit thanks to which an electric signal is converted to a sound wave in the medium. The sound wave forms a grating which can diffract an input laser beam. Typically, AODs are constructed in such a way to deflect most of the light in a single order of diffraction, whose output angle is proportional to the frequency of the RF signal. This is the so called Bragg regime for an acousto-optic device, in analogy with Bragg's diffraction in crystals, that occurs when the Klein and Cook parameter Q is much more than 1 [45]. The Q parameter can be expressed as:

$$\mathrm{Q} = \frac{2\pi\lambda_0 \mathrm{L}}{\mathrm{n}\Lambda^2 \cos\theta_0} \tag{4.1}$$

where λ_0 and Λ are the laser and acoustic wavelength respectively, L is the thickness of the crystal medium, n is the refraction index and θ_0 the angle of incidence. The Q value in the case of our AODs, obtained by substituting the parameters of the device taken from the datasheet, is equal to 136. The Bragg interaction between a photon of the optical beam and a phonon of the acoustic wave is conveniently represented in momentum space for which, by imposing energy and momentum conservation, it is possible to express the momentum of the deflected photon $\mathbf{k}_\mathrm{d}$ as the sum of the initial momentum $\mathbf{k}_\mathrm{i}$ and the phonon momentum $\mathbf{K}$:

$$\mathbf{k}_\mathrm{d} = \mathbf{k}_\mathrm{i} + \mathbf{K} \tag{4.2}$$

The amplitude of the phonon momentum is given by

$$\mathrm{K} = 2\mathrm{k}\sin(\theta_\mathrm{B}) \tag{4.3}$$

where the Bragg angle θ_B represents the angle between the momenta $\mathbf{k}_\mathrm{i}$ and $\mathbf{K}$, as described in figure 4.1

$$\theta_\mathrm{B} = \sin^{-1}\left(\frac{\lambda_0}{2\Lambda}\right) \tag{4.4}$$

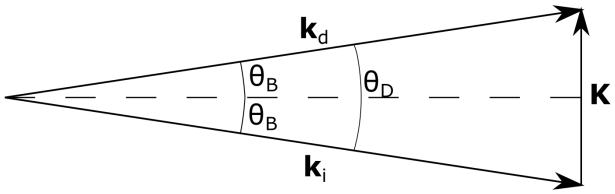

Figure 4.1: Bragg and deflection angles identified by the directions of the momentum vectors.

In the expression 4.4 λ_0 is the optical wavelength in free space and Λ the acoustic wavelength. Considering a laser beam incident on the crystal at the Bragg angle, the angle of the deflected beam will be its double:

$$\theta_{\mathrm{D}} = 2\theta_{\mathrm{B}} \simeq \frac{\lambda_0 \mathrm{f}}{\mathrm{v}} \tag{4.5}$$

where the acoustic wavelength is substituted by the ratio v/f between the sound velocity in the crystal and the RF frequency. The deflection angle is referred to the direction of the zero order beam. Equation 4.5 shows the linear dependence of the deflection angle on the RF frequency f. Three main characteristics of an acousto-optic deflector are the bandwidth, the diffraction efficiency and the time aperture. The angular bandwidth represents the total angular region that can be spanned varying the radio frequency and can be expressed taking into account equation 4.5:

$$\Delta\theta = \frac{\lambda_0 \Delta \mathrm{f}}{\mathrm{v}} \tag{4.6}$$

where Δf is the frequency bandwidth. The resolution angle, instead, is given as a function of the optical aperture (or beam diameter if this is smaller than the aperture) D:

$$\Delta\phi = \frac{\lambda_0}{\mathrm{D}} \tag{4.7}$$

The number of spots that can be resolved simultaneously are thus given by the ratio between $\Delta\theta$ and $\Delta\phi$:

$$\mathrm{N} = \frac{\Delta\theta}{\Delta\phi} = \frac{\Delta \mathrm{f} \mathrm{D}}{\mathrm{v}} = \tau \Delta \mathrm{f} \tag{4.8}$$

Lastly, the frequency resolution is the ratio between the frequency bandwidth and the number of resolvable spots:

$$\mathrm{f_{res}} = \frac{\Delta \mathrm{f}}{\mathrm{N}} = \frac{1}{\tau} \tag{4.9}$$

Bandwidth and time aperture determine the angular span and the resolution of a single spot available for a specific device and are discussed in chapter 5. We characterize the diffraction efficiency of the AODs in the following sections.

4.1 RF source

The Rf signal that is used to drive the piezoelectric actuator can be produced by different sources. We chose to use a programmable device, an Arbitrary Waveform Generator (AWG). All the measurements and characterizations presented in the next section have been performed with an AWG model SDG 6022X manufactured by Siglent. An arbitrary waveform generator is an instrument that can produce a wide range of different waveforms. These arbitrary waveforms are based on stored digital data that describe point-by-point the desired voltage levels of the output signal. The possibility to create an RF signal of arbitrary shape allows for the realization of many patterns diffracted from the AOD, both static and dynamic ones. If the RF signal is composed of one single sine at frequency f, the AOD deflects the input beam into one single deflected beam whose output angle can be calculated with equation 4.5. An AWG can also be used to produce multiple deflected beams to obtain a complex pattern: this device can be easily programmed to produce the waveform corresponding to a sum of multiple sines at the desired radio frequencies such that the AOD deflects one beam for each frequency component of the RF signal. More complicated schemes can be realized by programming the AWG but, in some of the easiest cases, also built-in stored waveforms or modulation can be used successfully. In the following subsections two kind of tests on our RF source are described. We analyze in particular the effect of the finite number of points, that is a common characteristic of all the arbitrary waveforms that can be generated with the device.

4.1.1 Discretization of a sine and a sum of sines

We observed the output of the AWG with a spectrum analyzer in order to gain information about the spectrum of the RF signal. In particular, we used the AWG's software to map sine waves (or sum of sine waves) onto arbitrary waveforms, that are none other than a sequence of discrete digital values sampled from the desired analytic function. We ask ourselves which is the the minimum number of points needed to represent a sine wave in a discrete way. We then draw sine waveforms using a varying number of points describing one period. The waveform is then repeated periodically by the AWG. The discretization of a waveform causes a distortion of it that introduces second harmonics and undesired frequency components in the RF signal. In figure 4.2 I report the frequency spectra of two sine waves at 1 MHz with different number of sampling points per period, in particular 3 points for the blue trace and 100 points for the yellow one. The spectra are measured with a USB-SA44B Signal Hound model spectrum analyzer. Three points is the smallest number of points that we need to sample a period of a sine wave. This causes anyway an undersampling for which the spectrum (blue curve) shows many more frequency components, among which a second harmonic that is just a few dBm lower than the carrier frequency. On the other hand, when the number of samples per period is increased to 100 (yellow trace), the number of spurious frequency components is extremely reduced. Having a high number of frequency components as in the blue spectrum may be detrimental for

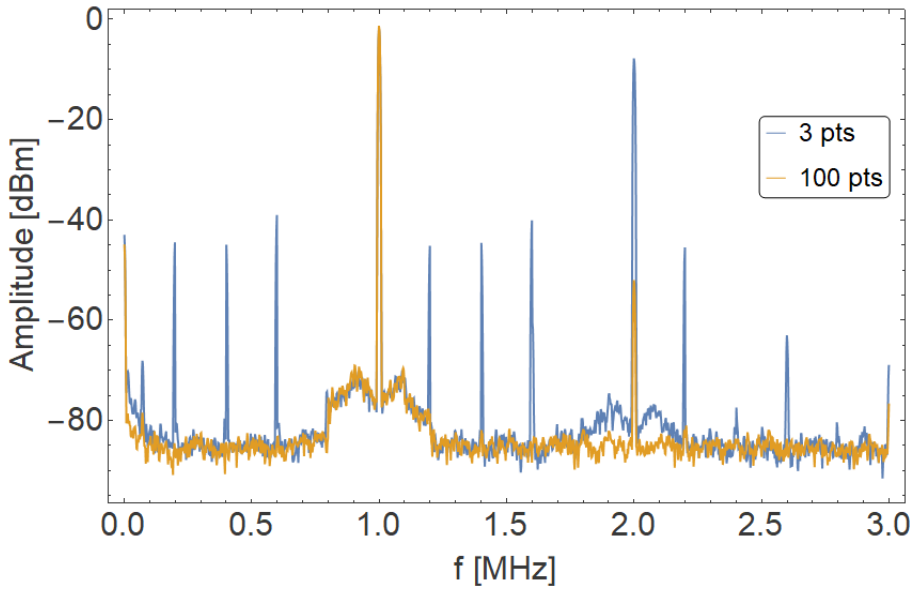

Figure 4.2: Generation of a digitally sampled sine wave: $\sin(2\pi x)$.

the experimental setup. The presence of unwanted frequency components with a power level comparable to the carrier may produce additional undesired deflected beams. In addition, the presence of frequency components with high RF power outside the bandwidth of the matching circuit of the AOD may be harmful to the instrumentation.

If we complicate the waveform produced by the AWG, for example a sum of nine sine waves spaced by ten kHz, we get the spectra reported in figure 4.3. The waveform is the sum of of $\sin(2\pi \cdot 100x)+\sin(2\pi \cdot 101x)$ and so on up to 109. The periodicity of such function is the least common multiple of the periods of each sine wave. During this period, each components oscillates for 100, 101,...,109 times. We compare this time a number of samplings equal to 300 and 1000 per period of the total waveform. This means that every oscillation of each frequency component will be sampled with 3 to 10 points. These complex functions with around 100 oscillations per each frequency component are generated by the AWG with a frequency of 10 kHz, so that the frequency of each sine frequency component is around 1 MHz. Sending such a waveform to the AOD produces nine static deflected beams. In figure 4.3a the spectra for both 300 and 1000 samplings are almost equal, while in figure 4.3b where a wider range of frequencies is shown we notice an important difference, since the signal with 300 sampling points per period is characterized by very high peaks corresponding to the second harmonics of the signal. It's now necessary to scale up these frequencies to match the working range of the AOD. In order to do this, we increase from 10 kHz to 1 MHz the frequency at which the waveform with 9 frequency components and a sampling of 300 samples per period is generated, so that the total frequencies are scaled up to 100,_,109 MHz. As we have seen, with a sampling of 300 points per period the second harmonics are non-negligible. Nevertheless, these frequencies fall above 200 MHz, outside the bandwidth of the AOD, so they introduce no

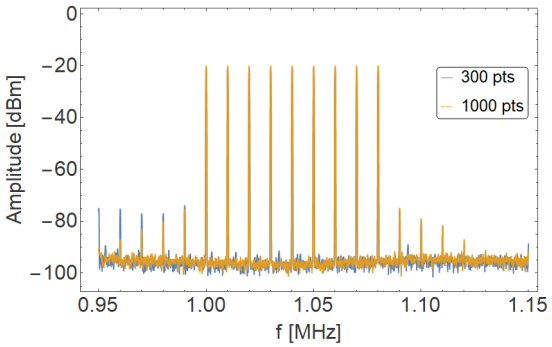

(a) Generation of a digitally sampled sum of sines with frequency components from 1 to 1.09 MHz.

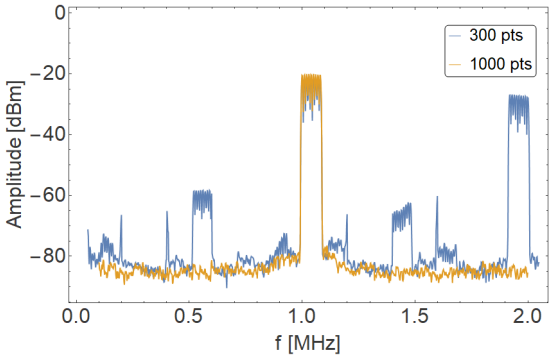

(b) Low sampling rates can cause the presence of second harmonics.

Figure 4.3: Short and wide range spectra for a complex sum of sine waves.

additional unwanted deflected beams. Moreover, the second harmonics can be filtered out with a low-pass filter, which would also avoid to cause damage to the instrumentation due to mismatching with the RF circuits of the AOD.

Generation of time-dependent waveforms

AWGs allow also to generate a time dependent waveform, in which for example two frequencies are alternated during the period of the waveform. We can draw the waveform to produce for half the period a sine wave at frequency f_1 and in the second half a sine wave at frequency f_2. This is the technique that we used to create time-averaged potentials, and consists in a piecewise function with adjustable duty cycles. This technique is very flexible because we can adjust the number of blocks composing the piecewise function and also the duty cycles. Its main downside is the presence of second harmonics, just like in the case in figure 4.3b. In the case of the specific AWG that we employed in our measurements and characterizations, this kind of time dependent function which alternates between two different frequencies can be generated by means of the buil-in FSK modulation (Frequency-Shift-Keying). In figure 4.4 the spectra produced by the custom time dependent modulation versus the FSK one are compared in a wide frequency range. In both the cases the RF frequency component is alternated between 90 and 110 MHz at a frequency equal to 100 kHz. The FSK modulation avoids the presence of second harmonics, that instead are present in the custom waveform spectrum, but can only switch between one single couple of frequencies. The switching among many frequency components or duty cycles different from 50% are achievable with the software generated modulation only.

Figure 4.5a shows instead the peak at 110 MHz with a span of 1 MHz. There is a good agreement between the spectra of the two different methods, with the yellow trace, relative to the custom generated waveform, being approximately 5 dB below the blue trace of the FSK method, due to the presence of second harmonics with respect to the FSK method. Moreover, some key frequencies seem to work better and produce less harmonic distortion in the vicinity of the carrier,

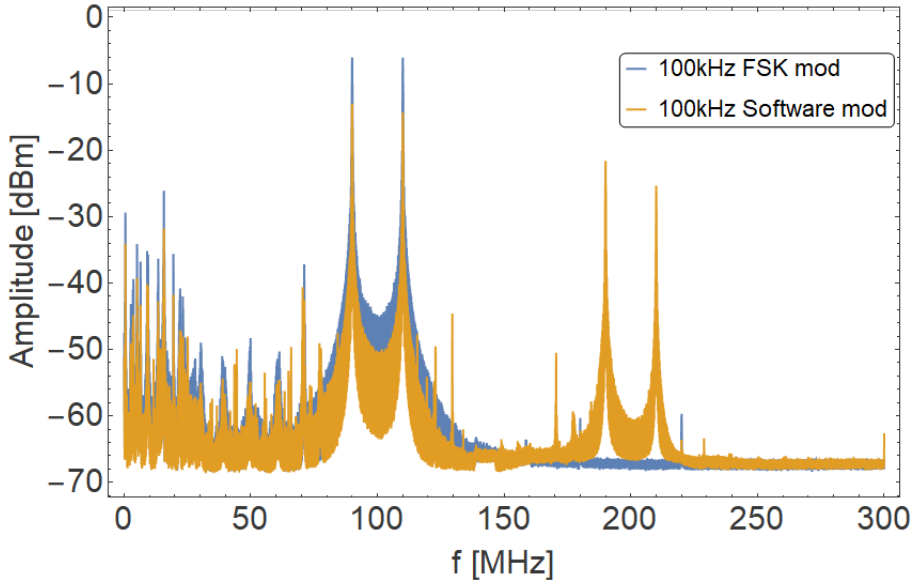

Figure 4.4: Spectra produced by a custom and a built-in modulation of the RF signal produced by the AWG.

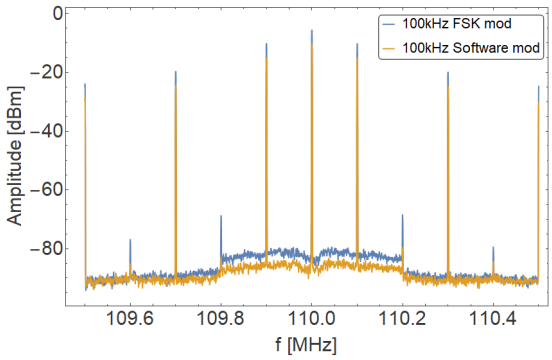

(a) Comparison of the method for a modulation at 100 kHz. The peak observed is the one at 110 MHz.

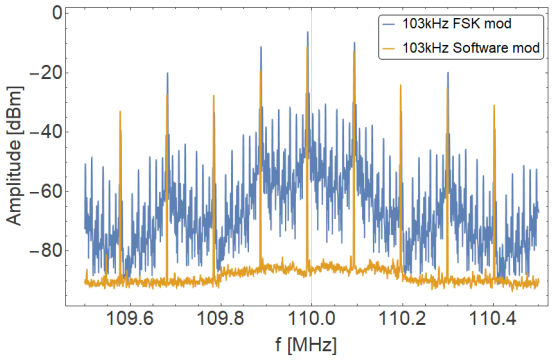

(b) Comparison of the method for a modulation at 103 kHz. The peak observed is the one at 110 MHz.

Figure 4.5: In the vicinity of the carrier frequency the two methods present differences.

while others both change the carrier frequency of a few tens of kHz (the carrier is in the 100 MHz range) and produce much more frequency components, as we can see in figure 4.5b. To conclude, this analysis shows that the FSK modulation is characterized by a a cleaner frequency spectrum, and it is to be preferred if the switching regards two sine frequencies only. The custom waveform, instead, will be used in case a more complex time-dependent waveform is necessary, for example for the switching between more than two frequencies or between arrays of frequencies.

4.2 Static characterization

4.2.1 Diffraction efficiencies of the AODs @813 nm

In this subsection I will describe the characterization of the diffraction efficiency for the two AODs that we use for the generation of optical tweezers arrays. The AODs (DTSX-400-810 manufactured by AA Optoelectronic) are designed to work in a wavelength range around 810 nm with a nominal central frequency of 101.5 MHz. We choose to employ 813.4 nm laser light generated by Matisse Sirah Titanium Sapphire laser for the creation of optical tweezers. This corresponds to the magic wavelength for the $^1S_0 \rightarrow ^3 P_0$ transition of strontium, and this choice will allow for the exploitation of the $^3P_0$ clock state as an additional degree of freedom (see chapter 2) in future experiments. In the final setup the two AODs will work in pair, just like two brothers. For this reason we labeled them with the nicknames *Mario* and *Luigi*, that are the devices used for the horizontal and vertical deflection of the laser beam, respectively. These names will be used in the following part of this thesis to identify the AODs.

We performed the characterization of the diffraction efficiency in several alignment configurations. Each set of measurements was performed tabulating the power measured with a power meter versus the RF frequency injected in the AOD. The "deflected" power was then divided to the power value before the AOD, in order to obtain an efficiency value.

With this measurement we want to characterize the maximum achievable efficiency at each diffraction frequency value. The optimal efficiency for Mario, showed in figure 4.6 largely exceeds the 90% for many RF values, within 83 and 124 MHz, a range compatible with the working range declared in the datasheet. The efficiency curve is slightly asymmetrical and falls down rapidly for frequencies below 80 MHz. The plateau of maximum efficiency is remarkably flat. Very similar results were obtained also for the second AOD, Luigi, as shown in figure 4.7.

The efficiency is strongly dependent on the alignment of the AOD and its tilting had to be changed significantly in order to diffract the laser beam with the maximum efficiency. Since the device will be used in a static alignment configuration, we must determine the best tilting of the AOD.

In the final configuration it will not be possible to adjust the alignment of the AODs for every frequency, so it is necessary to find the alignment condition with the optimal efficiency over the whole bandwidth of the AOD. I then performed

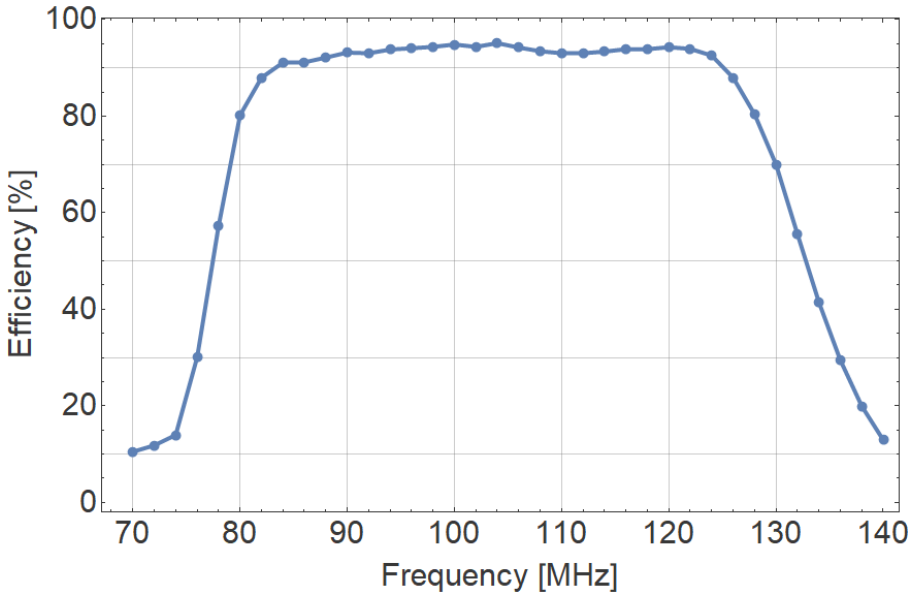

Figure 4.6: Plot of the best diffraction efficiency obtainable as a function of RF frequency for Mario AOD.

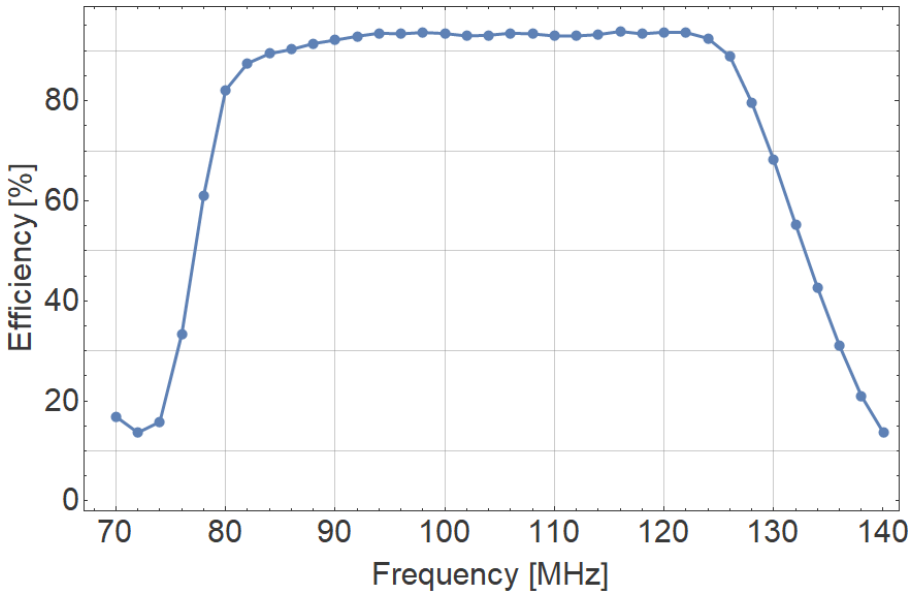

Figure 4.7: Plot of the best diffraction efficiency obtainable as a function of RF frequency for Luigi AOD.

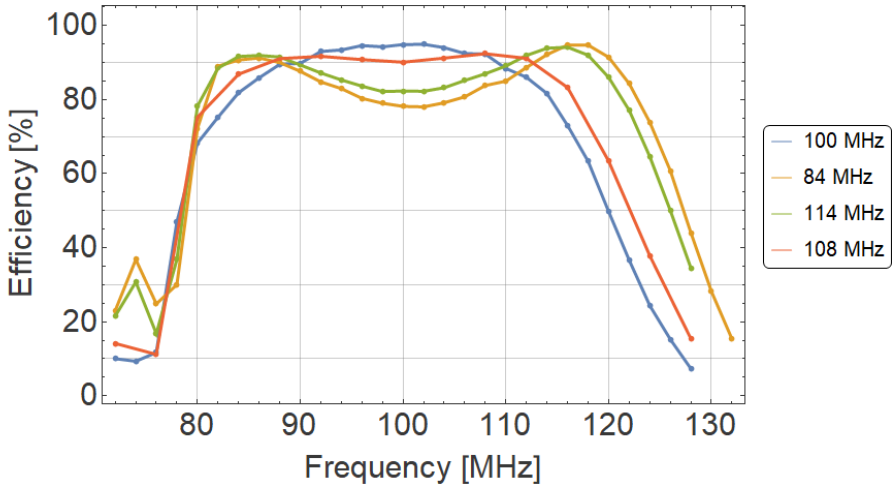

Figure 4.8: Plot of Mario diffraction efficiency obtained for configuration that maximize the diffraction efficiency at particular RF frequencies.

four more sets of measurements with a fixed AOD alignment: before each measurement the alignment and tilting of the AOD was adjusted in such a way to maximize the diffraction efficiency for one particular value of the RF frequency. First of all, the diffraction efficiency was optimized for an RF frequency at the center of the bandwidth of the device (100 MHz). Then, The procedure was repeated for frequencies at the edges of the bandwidth (84-86 MHz and 114 MHz). Finally, I repeated the measurements maximizing the output power efficiency in the configuration of the AOD for an intermediate frequency (108 MHz).

In figures 4.8 and 4.9 the diffraction efficiency curves for Mario and Luigi are reported, respectively. As specified in the plot legends, the plots are referred to four different optimizations performed spanning different RF values within the AOD range. The blue plot configuration (100 MHz) has a maximum efficiency at the center of the range, around 100 MHz. The efficiency of the two configurations in which the two AODs are aligned at the extremes of the bandwidth are plotted in yellow (84 MHz for Mario, 86 MHz for Luigi) and green (114 MHz for both the devices) and, differently from the blue curve, shows two maxima of efficiency at the edges of the range. These two edge configurations guarantee a much wider bandwidth than the previous one but they lack efficiency in the center of the bandwidth. In order to find a compromise capable to grant a large bandwidth with a profile as flat as possible, we tested an intermediate configuration in which the AOD is aligned to maximize the efficiency at 108 MHz. The plots show the same behaviour for both the AODs, so the previous analysis is valid both for Mario and Luigi AODs. Remarkably, all of the curves show a low-frequency cutoff at the same frequency (approximately 76 MHz), while the high-frequency side starts to fall down at rather different turning points. In the set of measurements, the RF amplitude was fixed at the beginning of each set to the value that maximized the deflected laser power at the frequency for which the alignment was optimized. In particular, we set the RF amplitude for Mario measurements to 0.7 dBm for the 100 MHz configuration, while the amplitude

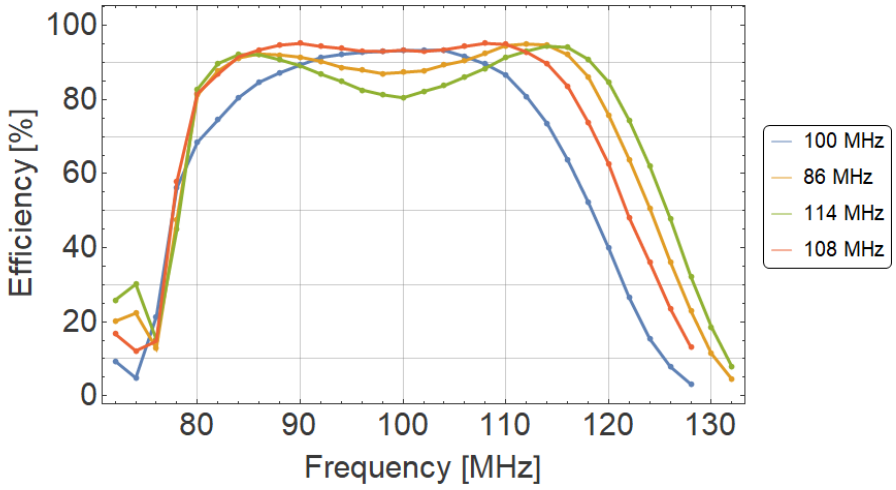

Figure 4.9: Plot of Luigi diffraction efficiency obtained for configuration that maximize the diffraction efficiency at particular RF frequencies.

was 1 dBm for all the other configurations (optimization @ 84 MHz, 108 MHz and 114 MHz). As for Luigi, the RF amplitude was set to 0.5 dBm for th 100 MHz configuration and 1 dBm for the other three.

In the following characterizations of the tweezers we employed the middle ground configuration (optimization for the RF frequency of 108 MHz) because it guarantees uniform diffraction efficiencies above 90% over a range of 20 MHz. This is an important feature in case the AOD driven with a RF signal with multiple frequencies is used to generate an array of optical tweezers. Indeed, the depth of each tweezer will depend on the efficiency at each frequency value, hence a flat efficiency curve is required to obtain an uniform tweezer array. An uniform efficiency curve is then a good starting point for the implementation of feedback procedures, which are anyway required in order to obtain perfectly uniform arrays (see chapter 2).

4.2.2 Efficiency dependence on the RF power

In this subsection the diffraction efficiency of the AODs is studied as a function of the RF amplitude. Mario and Luigi were tested one by one and the measurements were taken in several zones of the bandwidth. In particular we tested them for the central frequency (101.77 MHz for Mario and 102.2 MHz for Luigi) and on the edges of the bandwidth, at 82 MHz and 118 MHz for both the AODs. This kind of measurement is a useful step for the implementation of feedback operations, whose goal is to flatten the efficiency curve for all the frequencies to a desired value.

These measurements are complementary to the the previous characterization: here we fix one particular frequency of the driving RF signal and change the amplitude in a logarithmic scale (dBm), from -20 to 1 dBm. At the same time we measure the output laser power and the input one (after and before the AOD) with a power meter, and calculated the diffraction efficiency as the ratio between

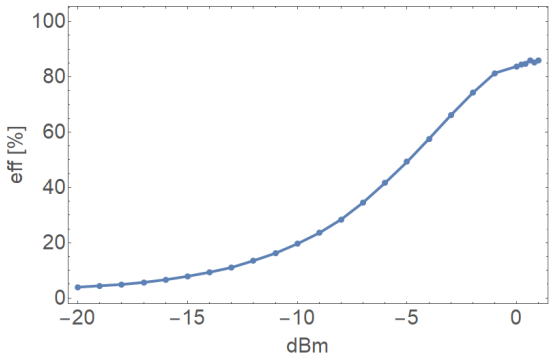

(a) Mario's diffraction efficiency as a function of the RF power.

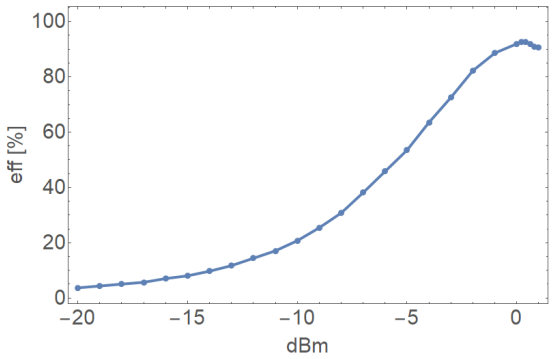

(b) Luigi's diffraction efficiency as a function of the RF power.

Figure 4.10: Diffraction efficiencies in logarithmic scale obtained for both Mario and Luigi in the central frequencies configuration (f_M=101.77 MHz and f_L=102.2 MHz).

these two quantities, as in the previous subsection.

Measured efficiency values are shown in figure 4.10. The efficiency increases for increasing values of RF power up to a plateau, that is reached for RF amplitudes above 0 dBm. These measurements are important because they represent the first step in the implementation of the feedback algorithm. The power amplitude assigned to every RF frequency component can indeed be calibrated using these curves.

In particular, considering a pair of diffracted beams that is generated by an AOD driven by a two frequency components RF signal, it is possible to modulate the amplitude of the frequency component in order to flatten the diffraction efficiencies to a common value, as depicted in figure 4.11. The amplitude of the two deflected beams are measured on a camera. It is possible to act on the RF power of one of the two components to change the efficiency of that specific spot accordingly to figures 4.10. Supposing that both the RF frequency components are generated for the RF power that maximizes the efficiency, increasing further the amplitude of the lower efficient frequency component results in no advantage. Hence, the amplitude of the higher efficient frequency component has to be decreased. In the block scheme reported in figure 4.11, the amplitude of the yellow tweezer is the 70% of the blue one, so the RF power of the frequency component corresponding to the blue spot is decreased in order to decrease the efficiency to 70% the maximum value, exploiting the plots in figure 4.10. The amplitude of the pair of tweezers, measured again onto a camera, should now be approximately the same.

This correction could, in principle, be determined a priori in order to flatten the efficiency curves in figures 4.8 and 4.9 for a wide range of RF frequency components, by exploiting the conversion from efficiency to power amplitude described in the example above. Such a procedure is presented in the scheme in figure 4.12, where the efficiency curve of Mario as a function of the RF frequency in the case of the alignment for 108 MHz is considered. Exploiting the dependence of the efficiency on the RF power, the efficiency curve can be flattened in

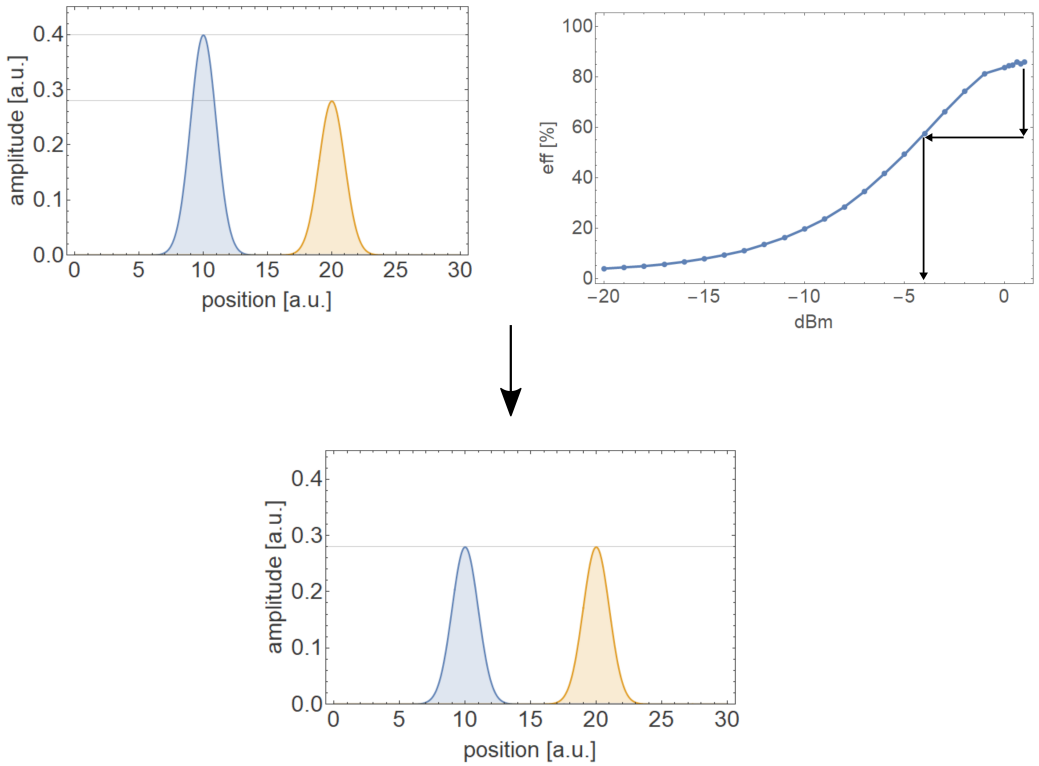

Figure 4.11: Blocks scheme for the realization of the feedback loop on the amplitudes of a pair of deflected beams.

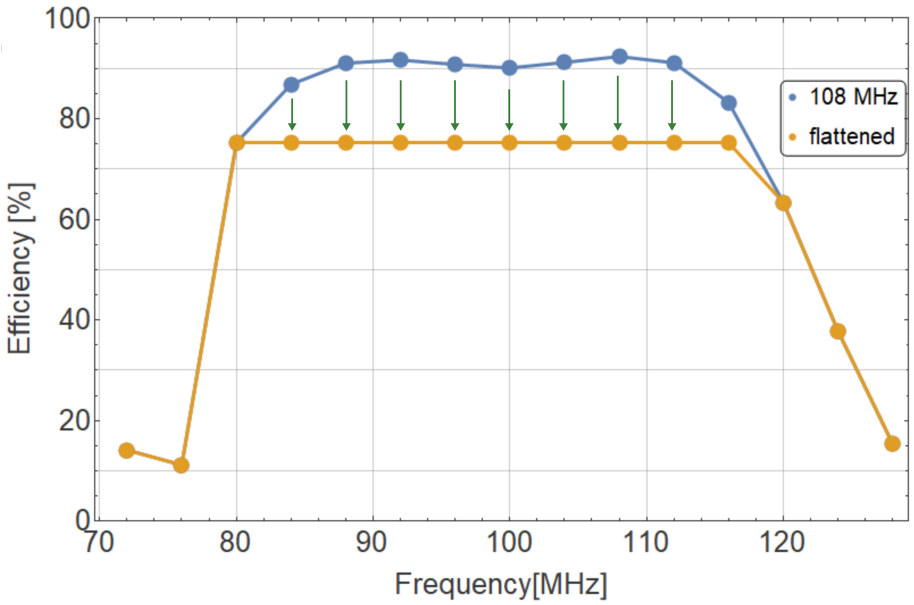

Figure 4.12: Blocks scheme for the realization of an a priori flattening of the diffraction efficiency plot for the range of frequencies from 80 to 116 MHz.

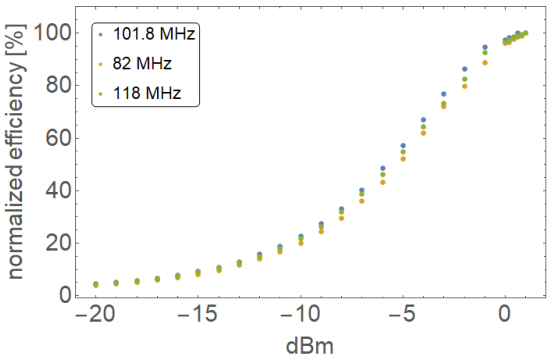

(a) Mario's diffraction efficiency as a function of the RF power for three different configurations.

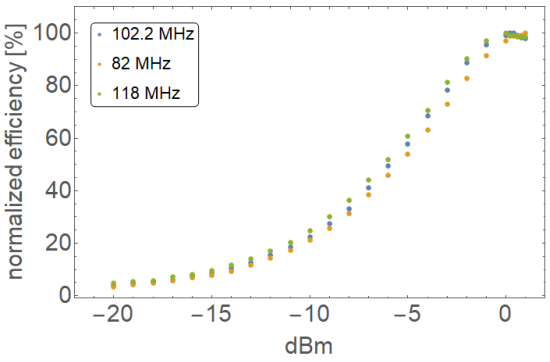

(b) Luigi's diffraction efficiency as a function of the RF power for three different configurations.

Figure 4.13: Diffraction efficiencies in logarithmic scale. Data are normalized to the maximum value of each corresponding set.

principle by using different RF power for each frequency component, taking all the efficiencies in the desired range to the same value. The range of frequency components considered determines the target efficiency, since all the efficiencies in that range have to be decreased to the lower efficiency value, for the reasons explained above. In the case of figure 4.12 the original efficiency curve (blue plot) is converted into a new efficiency curve (yellow plot) for which the diffraction efficiency is constant in the central frequencies region, from 80 to 116 MHz. The larger is the frequency range for which the efficiency has to be flattened, the smaller is the constant target efficiency value.

In the flattening procedure described above, only the power dependence at central frequencies reported in figure 4.10 was considered. In figure 4.13, measurements taken for a few different RF frequency values are shown. The efficiency curves are normalized in order to point out the differences of different curves measured for the same AOD, both for Mario and Luigi. Since the correspondence is not perfect, the flattened efficiency curve will show slightly fluctuations around the constant value. In order to obtain a perfect amplitude correction, the RF power of each frequency component should be corrected using the efficiency curve as a function of the RF power specific for that frequency value. Measuring these curves for every frequency value is too demanding, and typically more complex feedback procedures are exploited in order to get an uniform array. Anyway, this simple method is expected to reduce the discrepancies in the efficiency of different frequency components and it is so a good starting point for the generation of a uniform 1D array of optical tweezers. The procedure described above can be used in case a single AOD is used to generate the array of optical tweezers, i.e. for the generation of linear arrays with arbitrary geometries. Nevertheless, the situation is more complex in case a pair of AODs is used to generate a two-dimensional array. In this case the depth of each OT depends on the efficiency of both the AODs in a nontrivial way, as it will be shown in the following sections. In this case the feedback procedure described above is no longer usable, and a

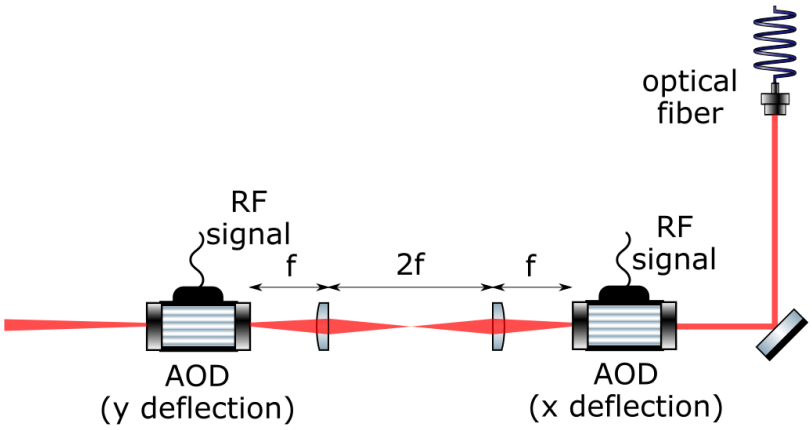

Figure 4.14: Experimental apparatus for the characterization of the diffraction efficiency produced by a pair of perpendicular AODs.

more complex procedure is required.

4.3 Static characterization of two crossed AODs

In this section the case in which a pair of crossed AODs are used to deflect a beam, or multiple beams, in a 2D plane is analyzed. The AODs are placed in the configuration shown in figure 4.14, that is a simplified version of the final setup presented above in figure 3.1. The pair of devices are separated by a 1:1 telescope, whose role is to match the two devices and avoid distortions in the final deflected beam. The first AOD along the optical path is Mario and is oriented horizontally to produce the deflection along the horizontal axis. The second AOD, Luigi, is instead oriented vertically.

The first test is a direct measurement of the efficiency of the couple of AODs for different combinations of frequencies components on the two channels. In particular, I measured the power before the first AOD and after the pair of devices for 36 combination of frequency over the two channels. For each AOD the frequency spans the range 80-130 MHz at 10 MHz steps.

The resulting plot for the first measurement is the 6x6 matrix reported in figure 4.15. The sampling of the frequency values allows us to cover all the working range of the AODs. The diffraction pattern is compatible with the single AOD measurements, in fact the area centered in f_M =100 MHz, f_L =100 MHz is the one with higher efficiency. To create this map both Mario and Luigi were aligned in such a way that the efficiency is maximum for $f_M = f_L = 108$ MHz (see section 4.2).

Since the x and y axes in the histogram in figure 4.15 correspond to the RF frequencies of Mario and Luigi respectively, it is in principle possible to com-

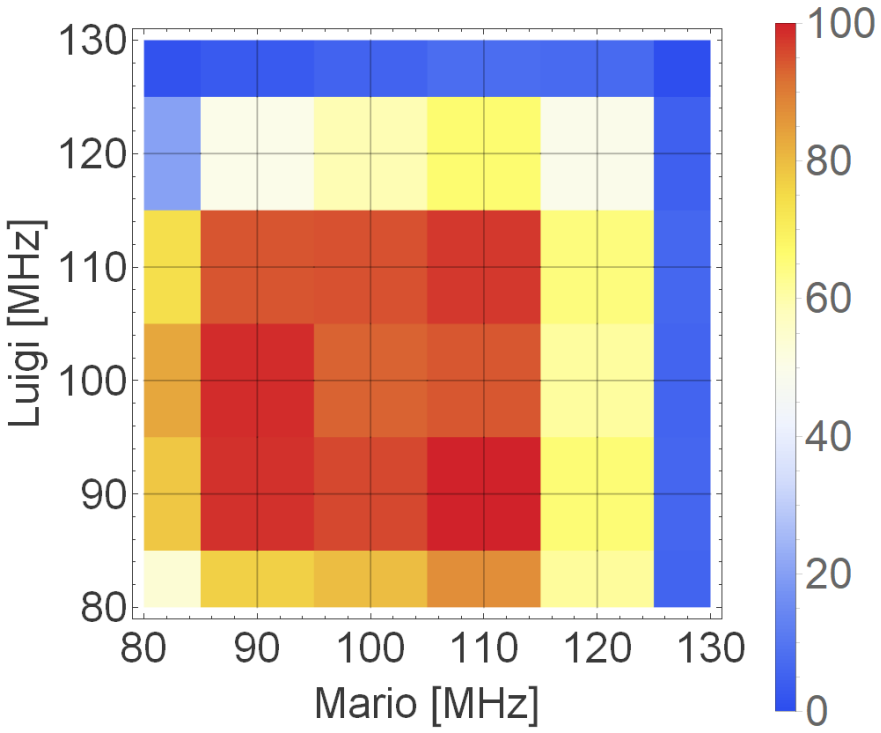

Figure 4.15: 2D diffraction efficiency map.

pare this 2D pattern with the single AOD's efficiency just by selecting one row or column, that will be corresponding to setting on Mario or Luigi one particular frequency value. For example, since the AODs were aligned in the configuration that produces the best efficiency at 108 MHz, we compare Mario's efficiency with the row corresponding to a fixed Luigi frequency, $f_L = 110$MHz, that is the closest tot 108 MHz. We then assume that the six values of diffraction efficiencies of this row are simply the product of the individual efficiencies of the two AODs, in particular the efficiency of Mario at the six different frequency values multiplied by the efficiency of Luigi at 110 MHz, as shown in equation (4.10).

$$\eta(f_M, f_L) = \eta(f_M) \cdot \eta(f_L) \tag{4.10}$$

In this case, the efficiency of Mario can then be retrieved by dividing each value of global efficiency in the row of the 2D map by the efficiency of Luigi at 110 MHz. In a similar way, an efficiency curve of Luigi can be retrieved by considering the column of the 2D map corresponding at 110 MHz on Mario and dividing each value of global efficiency by the efficiency of Mario at 110 MHz. The results of the comparison are shown in figure 4.16 for both Mario and Luigi. The agreement is good but not perfect, and the efficiency of the single AODs in the crossed configuration extrapolated from the 2D map is a little bit lower than the efficiency measured in section 4.2 for the individual AOD configuration. This discrepancy suggests that the behaviour of the coupled AODs cannot be described as the product of two individual AODs. A possible explanation of this behaviour

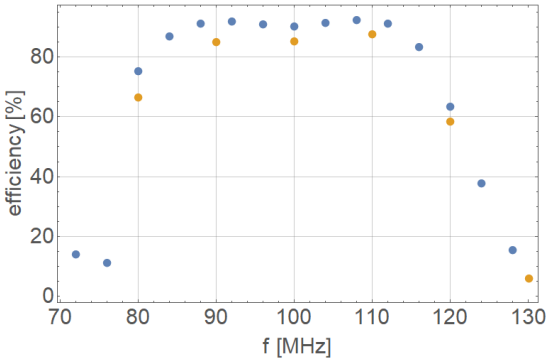

(a) Mario's diffraction efficiency as a function of the RF (blue dots) is compared to the efficiency extrapolated by the 2D histogram (honey dots).

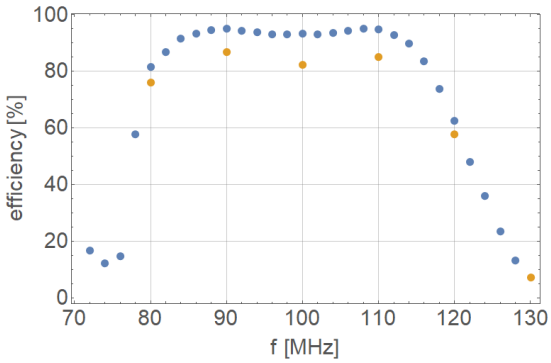

(b) Luigi's diffraction efficiency as a function of the RF (blue dots) is compared to the efficiency extrapolated by the 2D histogram (honey dots).

Figure 4.16: Comparison between single AOD efficiency and extrapolation out of the crossed AODs efficiency.

could be the dependency of each AOD's efficiency on the alignment of the other. The plots relative to single AOD's efficiency in figures 4.8 and 4.9, in fact, were obtained lighting the crystal perpendicularly to its surface, while in this case, especially for Luigi, the incident angle depends on the RF that drives Mario's deflection. The channels are coupled and since the alignment of the devices has relevant effects on the diffraction efficiency, as pointed out in the graphs in figures 4.8 and 4.9. The coupling between the devices, a topic that will be discussed further in the next paragraphs, highlights the importance of characterizing also the crossed AODs configuration as well as the characterization of the AODs alone.

4.3.1 Derivation of a continuous 2D efficiency map

In this subsection the characterization of a 2D efficiency histogram is extended to the whole frequency range of the AODs. For reasons of time, to cover a 60 MHz range in the two axis with 1 MHz steps we cannot measure manually the efficiency of 60x60 points. The technique that we will try to use is to modulate with a continuous linear sweep the driving RF frequency of both the AODs, taking a picture of the square region with a camera. Then we will check the consistency of the method comparing slices of this continuous distribution with efficiencies measured directly for the 2D pattern. Finding a fast method for the measurement of the efficiency of coupled AODs is fundamental because, since the map is dependent on the alignment as pointed out in the paragraphs above, such a characterization has to be done every time that the alignment of the devices is changed, even in the final setup.

The setup used for this measurement, reported in figure 4.17, includes a couple of lenses that are placed between the second AOD and the focusing objective, namely a tube lens and a scan lens. This pair of lenses has an important role as it allows, together with the microscope objective, for the imaging of the beam deflected by the crossed AODs to a CCD camera model DCC1545M man-

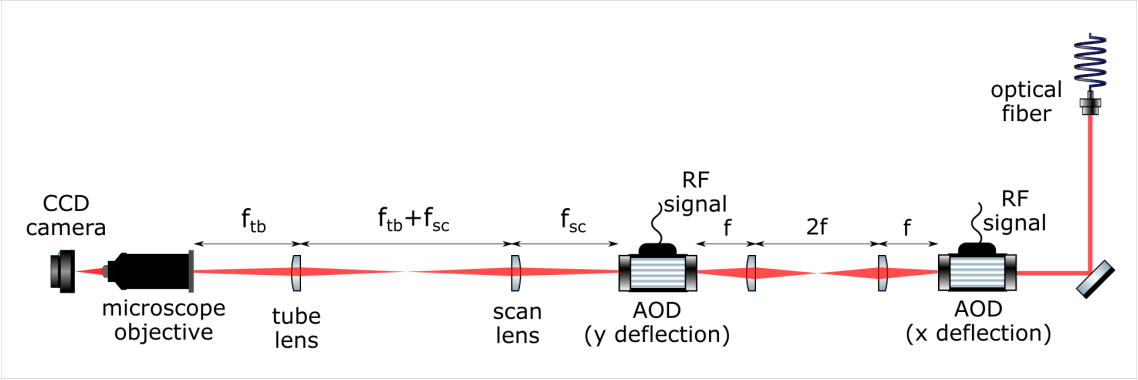

Figure 4.17: Experimental apparatus for the characterization of the diffraction efficiency produced by a pair of perpendicular AODs exploiting sweep modulations to realize a continuous map.

ufactured by ThorLabs. In order to obtain a continuous 2D map of the crossed AODs, we modulate the RF frequency on the two devices with a linear sweep to cover the range from 72 MHz to 132 MHz. To guarantee that the map is traced uniformly, we apply very different sweep rates on the two AODs, in particular 20 kHz on Mario and 30 Hz on Luigi. The *moving* diffracted beam is then projected onto the CCD camera, whose role is to collect a time mediated image of the laser spot spanning a 60x60 MHz square 2D plot. The exposure time of the camera is set to 30 ms, the pixel clock to 5 MHz and the frame rate to the maximum possible (29.7). In order to avoid aliasing or other systematic effects due to the integration time, we finely tuned the sweep time of the modulation on the RF signal of the second AOD. We observed the real-time image captured by the camera and continued tuning the sweep time until the image of the camera presented no artifacts. Such a measurement, as shown in figure 4.18a, provides only information on the number of counts of the camera and it is not a direct measurement of the diffraction efficiency. Moreover, the spatial coordinates are measured in terms of pixels and not in terms of RF frequencies, so they have to be converted into corresponding frequency coordinates. In order to convert the x and y axes into RF frequencies, and the counts of each pixel into diffraction efficiency, we exploited another image taken from the camera in the same configuration of the setup. This image, presented in figure 4.18b, contains four static spots at couples of frequency, with driving frequency coordinates on Mario and Luigi (f_M,f_L) of (90,90)MHz, (90,110)MHz, (110,90)MHz and (110,110)MHz. A fitting procedure on the Gaussian spots allowed us to determine the center (in pixels) of the spots. The difference of these pixel coordinates gives the spatial separation that corresponds to a 20 MHz step. The conversion factor can be then calculated for both the vertical (labelled with L) and horizontal (labelled with M) axes:

$$\mathrm{conv_M} = \frac{96.10}{20}\frac{\mathrm{pixels}}{\mathrm{MHz}} = 4.81\frac{\mathrm{pixels}}{\mathrm{MHz}} \tag{4.11}$$

$$\mathrm{conv_L} = \frac{95.98}{20}\frac{\mathrm{pixels}}{\mathrm{MHz}} = 4.80\frac{\mathrm{pixels}}{\mathrm{MHz}} \tag{4.12}$$

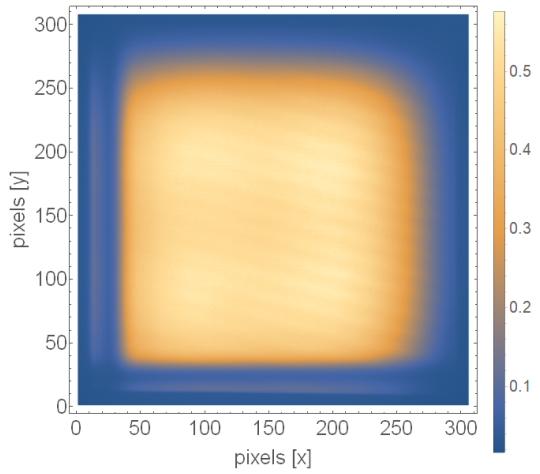

(a) 2D map imaged on a camera. The axes still measure the pixels and the counts of the pixels are not corresponding to an efficiency value.

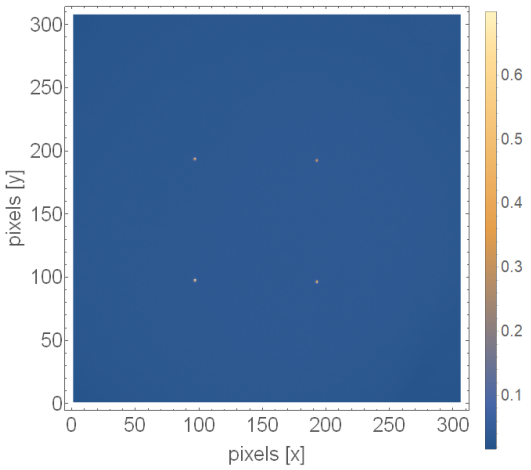

(b) Calibration measurement to determine the conversion of the axes in frequency axes and the counts in efficiencies.

Figure 4.18: Steps for the realization of a continuous 2D efficiency map.

Considering the uncertainty on the spot center due to the pixel size, we assume for both the vertical and horizontal directions the same conversion factor 4.8 pixel/MHz.

The same calibration image can be used for the conversion from number of counts to diffraction efficiency. We measured directly the efficiency in two different position: first we measured with a power meter the diffracted power for all the spots after the two AODs but before the focusing objective, then the same measurement was repeated placing the power meter after the objective too. In this way we are able to refer the final efficiency map to the efficiency after the AODs but before the objective. The counts-to-efficiency conversion factor can be obtained comparing the counts on the 2D map in figure 4.18a for the pixel corresponding to the four combination of frequencies for which the direct efficiency measurements were performed. Figure 4.18b comes in help because the position (in pixels) of the center of the four spots in this picture can be used to identify the position of the four combination of frequencies also in the 2D map in figure 4.18a. Finally, the four values of the conversion factor calculated at each spot are averaged in order to obtain a single value of conversion factor, that is reported in equation 4.13. Actually, four ratios were obtained for each of these factors because four spots were used for this procedure, but since they were very similar I report just the mean of the four values.

$$r_{AOD} = 1.510 \frac{\%}{\text{counts}} \tag{4.13}$$

The conversion factors from pixel to frequencies along x and y and the conversion factor from number of counts to efficiency can now be used to extract a 2D efficiency map from the image captured by the CCD camera of figure 4.18a. The final efficiency map resulting from the conversions is plotted in figure 4.19.

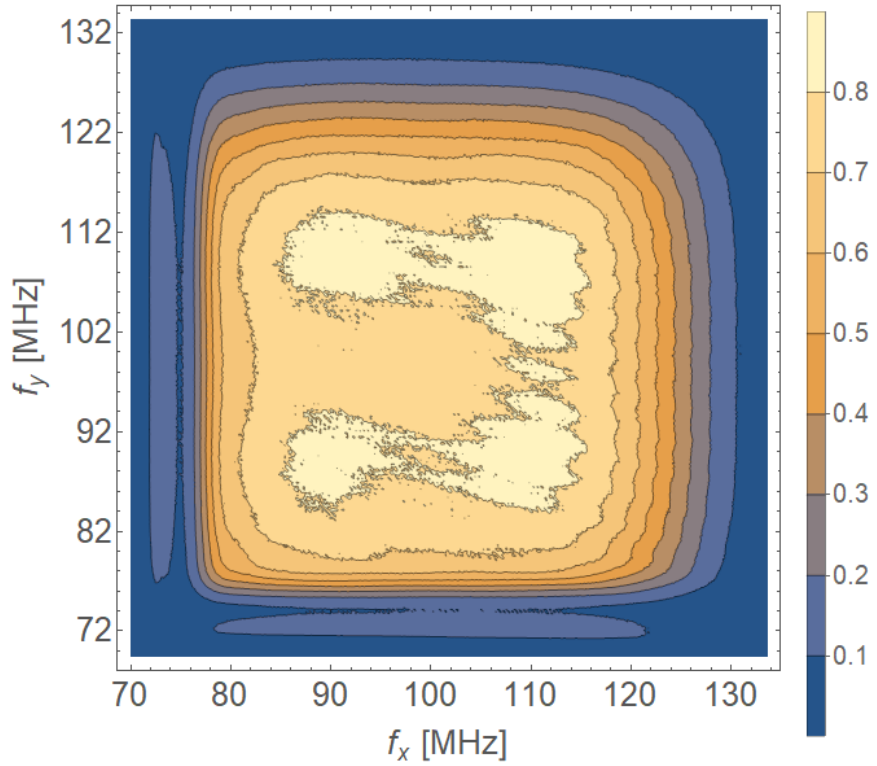

Figure 4.19: 2D efficiency map referred to the position before the AOD.

It is important to notice that such a plane 2D efficiency map is obtained by finely optimizing the AODs alignment using the same criterion described during the single AOD measurements, that is, by maximizing the output power for a 108 MHz signal that drives both the devices.

Validity of the method

Now that we have obtained the 2D map for the diffraction efficiency, we still have to check whether this technique and all the assumptions we did give the correct result. In order to validate the method we compare one single row/column of the map in figure 4.19 with directly measured efficiencies. The direct measurements were performed by fixing the frequency on one AOD and spanning the frequency of the other AOD in the interval from 70 to 130 MHz. For every device we fixed three different values of frequency, 85 MHz, 100 MHz and 115 MHz, while varying the frequency of the other in order to obtain six efficiency curves (each of them with 20 points) that correspond to three rows and three columns of the 2D map. Thanks to the conversion of the axes of the 2D map into frequency axes we are able to identify the rows and columns that correspond to 85, 100 and 115 MHz, that will be compared with the measurements obtained fixing the frequency on the first and the second AOD, respectively.

In figure 4.20 I reported a few of these comparison plots, in particular selecting the two couples related to central frequencies (100 MHZ) for the two posi-

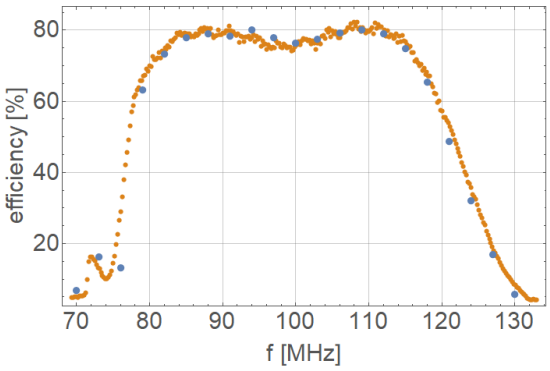

(a) Direct (blue dots) and indirect (honey dots) efficiency measurements fixing Mario's frequency to 100 MHz. Efficiency referred to the position before the objective.

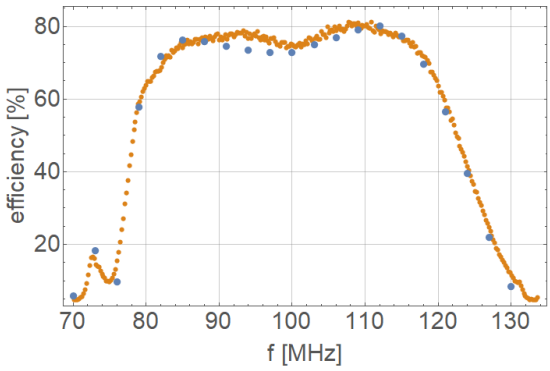

(b) Direct (blue dots) and indirect (honey dots) efficiency measurements fixing Luigi's frequency to 100 MHz. Efficiency referred to the position before the objective.

Figure 4.20: Comparison between direct and indirect efficiency measurements for selected frequencies.

tions. In this case the comparison shows very good agreement, confirming that using frequency sweeps and a camera is a valid method to characterize the efficiency of the crossed AODs. This is an important result because from now on it will be enough to repeat the procedure described in this subsection to draw a 60 MHz x 60 MHz continuous 2D efficiency map without any need to perform time consuming direct measurements of several tens of values of efficiency, but it is enough to measure a couple of them for calibrating the measurement.

Coupling between the channels

To conclude the characterization of the couple of crossed AODs apparatus, I tested the coupling between the two devices. In particular, I compared normalized rows or columns of the map in figure 4.19 for different frequency values. If the channels were decoupled, then the total diffraction efficiency could be determined directly, knowing the single AOD's efficiencies, as described in equation 4.10. Consequently, we could expect that different rows of the 2D map have the same shape, that is only determined by Mario's diffraction efficiency, and they differ just for a scaling factor that is Luigi's efficiency for the particular frequency corresponding to that specific row. This argument is also valid for the complementary situation, when different columns are compared. In figures 4.21a and 4.21b we show four normalized sections, respectively for rows and columns.

Figure 4.21a reports four efficiency curves of Mario at four different fixed frequencies on Luigi. Each trace is then normalized to its value at the center of the trace, for f_M = 100MHz, and analogue argument is repeated for the picture 4.21b in the complementary case in which the frequency driving Mario is fixed.

The shape of these curves is quite similar in the range up to 110 MHz, while beyond this value the sections at 120 MHz are quite different in both the plots. This result can be interpreted as the presence of coupling between the devices. This result is in agreement to what we found in figure 4.16, as some sort of coup-

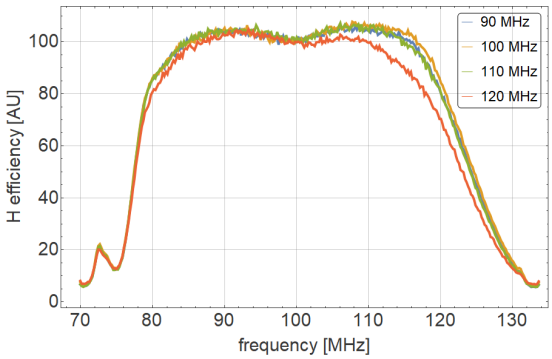

(a) Comparison of different sections showing Mario's diffraction efficiencies for different fixed Luigi's frequencies: 90, 100, 110 and 120 MHz.

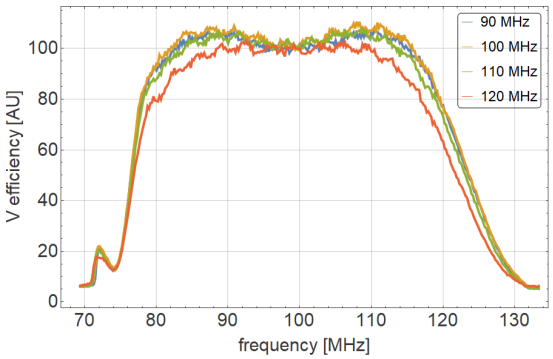

(b) Comparison of different sections showing Luigi's diffraction efficiencies for different fixed Mario's frequencies: 90, 100, 110 and 120 MHz.

Figure 4.21: Test on the coupling of the devices.

ling between the crossed devices is pointed out again. By the way, the presence of coupling, that is the reason why equation 4.10 is not exactly satisfied, is not surprising. During the series of measurements, we noticed that the 2D profile's efficiency is strongly dependent on the alignment of the AODs and it is possible to find configurations in which the coupling is higher than the one used for this measurement, that instead minimized the cross-talks. The fact that the efficiency of one AOD depends on the other one becomes clear if we think that whether we fix the frequency on Mario and observe the total span of Luigi bandwidth or vice versa, there is always a dependence on the incidence angle of the beam deflected from Mario that shines Luigi. Let's consider the case in figure 4.21b, where we consider four different fixed frequencies on the first AOD: each of these values will give a different incidence angle and, since the efficiency depends on the alignment of the apparatus, the total efficiency contribution will be affected.

This is the reason why a feedback procedure to flatten the amplitudes of multiple optical tweezers placed in a 2D array is a much more complicated task with respect to the procedure described in subsection 4.2.2 for a one dimensional problem.

4.4 Dynamic characterization

In this section I will report the characterization of the dynamical properties of the AODs. First of all, we characterize the rise time for different beam sizes and study the role of transient effects. Then, the real time dynamics of a deflected beam is described, with particular attention to the effect of the finite velocity of the acoustic wave in the AOD crystal. To conclude, the analysis of the amplitude modulation of the deflected beam during a fast switching is reported.

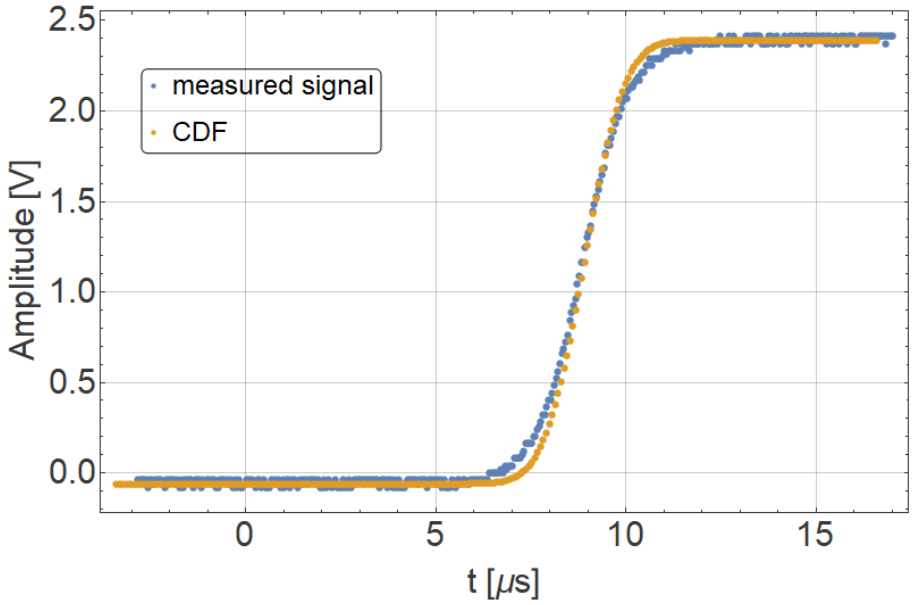

Figure 4.22: Superimposed plots of the measured signal and the Gaussian cumulative distribution function calculated for a 1 mm beam waist and v_s=650 m/s.

4.4.1 Rise time and transient effects

The first dynamic characterization of the AODs regards the rise time of the signal of a deflected beam. The RF signal driving the AOD is suddenly switched on, thus producing a deflected beam at a certain angle. Since the propagation of the acoustic wave in the AOD crystal takes place at a finite velocity of v_s, we study the dynamics of the switching on of the deflected signal by recording it on a photodiode that is connected to an oscilloscope. In particular, our AODs are based on a TeO_2 crystal for which the sound velocity provided by the datasheet is v_s =650 m/s. The sensor of the photodiode, a PDA36A2 manufactured by ThorLabs, is larger than the size of the beam, in such a way that the measured signal corresponds to the whole beam. In particular we implemented a laser beam of approximately 1 mm, while the sensor is a square with 3.6 mm sides. The photodiode integrates the signal of the deflected Gaussian beam over the spatial coordinates. The function describing the spatial integral of the intensity of a Gaussian profile can be approximated to the cumulative distribution function of the Gaussian beam [47]. In figure 4.22 the cumulative distribution function (CDF) of the Gaussian beam, calculated for a beam waist of 1 mm, is superimposed to the trace captured on the oscilloscope. The yellow trace, corresponding to the CFD of a Gaussian profile in the time domain, is then obtained by converting the original space domain CDF using the velocity of the acoustic wave in the crystal. This conversion to the time domain assumes that the motion equation of the sound wave in the crystal is a uniform motion at constant speed v_s=650 m/s. The yellow curve is in good agreement with the measured data in the blue plot, suggesting that the hypothesis of a sound wave propagating in the crystal at constant velocity is a good approximation of the real physical behaviour.

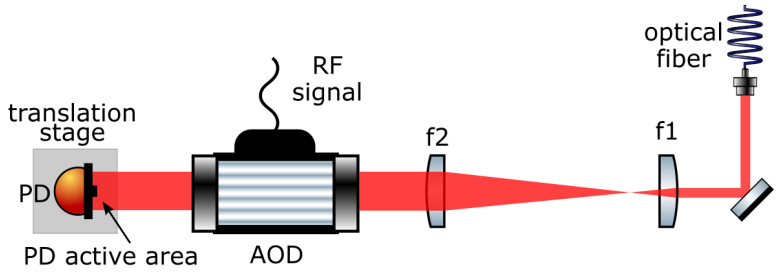

Figure 4.23: Apparatus used for the dynamic characterization. A photodiode (PDA8A2) is placed onto a translation stage that allows us to move the sensor and observe different portions of the beam. The pair of lenses f1 and f2 placed before the AOD allow us to change the dimensions of the beam entering the AOD. Different pairs of lenses are used to obtain the different beam sizes exploited for the measurements described in this chapter.

We now investigate the dynamical behaviour of the AOD for different sizes of the laser w[z] of 1 mm, 2 mm, 0.5 mm, 0.25 mm and 0.1 mm, measured at the position of the AOD. Figure 4.23 shows the experimental apparatus used for this set of measurements: a telescope allows us to change the size of the laser beam that passes then through the AOD which deflects it, and the light is collected with a photodiode. For every beam size measurement we place a telescope in the optical path, measure the waist of the beam with a camera and then we place the AOD in the position corresponding to the waist. Then, we use a photodiode with a large active area (PDA36A2, manufactured by ThorLabs) to measure the risetime of the signal of the deflected beam in such a way that the whole beam is contained in the sensor. After that, we exploit the photodiode represented in figure 4.23 (PDA8A2, manufactured by ThorLabs) that has a small sensor, to collect the signal of just a portion of the laser beam. The photodiode is placed onto a translation stage and can be moved perpendicularly to the propagation axis (z) of the beam to observe different portions of it. In this second part of the measurement we record the delay time between a time reference and the time in which the signal of the particular portion of the beam observed rises. This delay time will be compared with the spatial displacement of the photodiode on the translation stage in order to retrieve the shape of the laser beam inside the AOD. The delay time is measured considering the time at which the signal reaches half of its maximum. The RF signal that drives the AOD is a sine waveform at $f_{RF} = 110$MHz modulated with a square wave at 100 Hz that is generated by an arbitrary waveform generator (AWG). The reference time used for the delay time measurements is the time at which the square wave modulation switches its value.

First of all, we present the measurements relative to the rise time of the deflected beam signal for different beam sizes. In general the rise time corresponds to the time necessary to the signal to go from the 10% to the 90% of the maximum amplitude. The signal recorded by the photodiode is then the cumulative distribution function of the Gaussian beam intensity, hence the rise time corresponds to the time necessary for the sound wave to travel from the position for which

the CDF is the 10% to the position in which the CDF is the 90%. The distance between these two points, d, can be calculated for all the different beam sizes. It is possible to estimate the expected rise time considering the ratio between d and the sound velocity in the crystal.

$$\tau \simeq \frac{d}{v_s} \tag{4.14}$$

In table 4.1 we report the measured beam waist both along the x and y directions, the rise times expected from equation 4.14 and the measured ones. The sound velocity used for the conversion takes the usual value v_s=650 m/s, taken from the datasheet. The measured rise times are in good agreement with the estimated

Waist (x) [μm]	Waist (y) [μm]	d [μm]	Exp. rise time [μs]	Meas. rise time [μs]
1229±4	1146±4	1657±5	2.549±0.008	2.56±0.10
2219±4	2028±5	2929±6	4.506±0.009	4.54±0.10
540±5	537±5	771±7	1.186±0.011	1.17±0.10
288.3±0.5	269.4±0.5	445.1±0.7	0.6848±0.0011	0.55±0.10
115.1±1.2	96.5±1.2	215±2	0.331±0.003	0.26±0.10

Table 4.1: Rise times for different beam waists

ones for the three larger beam waists. The rise time values measured for the small laser beams are smaller than the expected ones. Nevertheless, the measurement for the 0.1 mm is still consistent with the predicted value. On the other hand, the measurements for the 0.250 mm beam are not consistent.

4.4.2 Study of transient times for different beam sizes

In this subsection we describe the second part of the measurements introduced above, the ones regarding the delay times. Delay time measurements are used to give an indirect measurement of the beam waist size in the position, along the propagation axis, where the AOD is placed. We measure the delay time as the time difference between a given starting point (in our case the time in which the AWG's square wave modulation switches from zero signal to a sinusoid at 110 MHz) and the time at which the signal measured on the photodiode rises. The photodiode can be moved perpendicularly to the propagation axis of the beam and has a small active area, in such a way that we can observe different portions of the deflected beam. The value of the sound velocity taken from the datasheet, v_s=650 m/s, is used to transform the time delays into spatial coordinates. In this way it is possible to reconstruct the beam profile inside the AOD. By plotting the maximum amplitude of the signal against its corresponding delay time for different displacements of the photodiode on the translation stage it is possible to perform a Gaussian fit. The fit performed after the conversion of the time delay coordinate into a spatial coordinate gives us an indirect measurement of the beam waist. In figure 4.24 a couple of these Gaussian fits are reported for the beams with 2 mm and 0.1 mm waist. The indirectly measured beam waists are shown in table 4.2 where they are compared with the values measured directly with a camera. The agreement between direct and indirect estimate is good. The

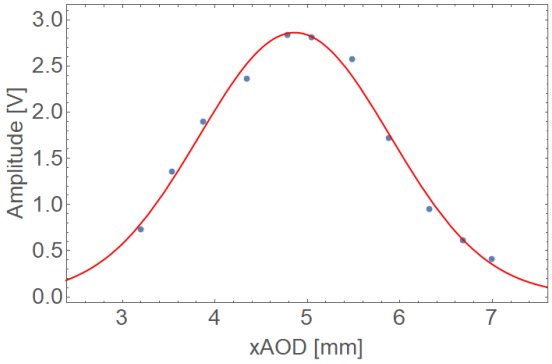

(a) Gaussian fit for 2 mm beam waist.

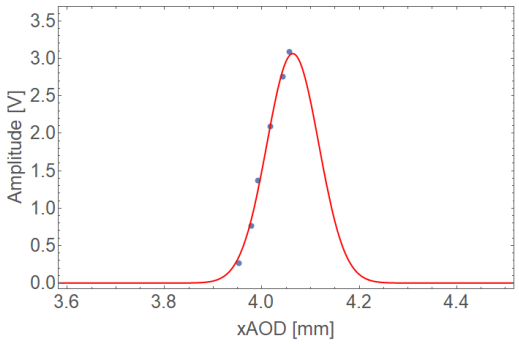

(b) Gaussian fit for 0.1 mm beam waist.

Figure 4.24: Gaussian fit on the amplitudes data plotted against the spatial converted coordinate.

	Measured waist (x) [μm]	Extrapolated waist (x) [mm]
1000 μm beam	1229±4	1.26±0.09
2000 μm beam	2219±4	2.06±0.19
500 μm beam	540.3±5	0.53±0.08
250 μm beam	288.3±0.5	0.20±0.10
100 μm beam	115.1±1.2	0.11±0.04

Table 4.2: Comparison between waists determined with different methods: in the second column the directly measured values are reported while in the third column we present the waist values obtained by converting the time delay measurements.

indirect measurements are reported in mm because the error obtained from the fit is larger. For little beam sizes the second method gives worse results, because the delay time is not a monotone function of the displacement of the photodiode. In particular, for large beam sizes the time delay increases going from one edge of the beam to the center and then continues to increase going towards the other edge. For small beams instead, in the second half of the beam the time delay decreases again. In other words, the hypothesis that different sections that are hit by the acoustic wave in the crystal at consecutive times propagate without ever mixing falls down. In figure 4.24a the Gaussian function is fitted to all the points of the data set, because the delay times increase monotonically with the spatial displacement. In the plot relative to the 0.1 mm beam waist reported in figure 4.24b the Gaussian function is indeed fitted to just one half of the data. Such an effect is probably due to the high divergence of the highly focused Gaussian beam. Despite this problem, the Gaussian fit over just a part of the data gives a good result.

In order to investigate in detail the behaviour of the time delay, in figure 4.25 the oscilloscope traces at different positions of the photodiode are plotted both for a large (2 mm) and small (0.1 mm) beam sizes. The traces are labelled in the legends with the corresponding displacement of the photodiode used for the measurement. In figure 4.25a a Gaussian distribution is superimposed to the traces. This curve is not a fit, but it is obtained using the real parameters meas-

ured for the system (w=2119 μm) and the sound velocity of the acoustic wave allows us to draw it in the time domain. This curve is a guide for the eye to point out the different time delays and to underline its physical meaning.

Figure 4.25b shows the analogue graph for a 0.1 mm beam waist, for which the time delay is no more appreciable, and it does not present a monotone behaviour. The expected total delay time for this beam size would be around 300 ns.

Dependence on the position along the propagation axis

In figure 4.26 the same traces that were represented in figure 4.25b are reported introducing a fictitious delay time to separate them. The two effects that we would like to understand is the apparently absence of a delay time and the presence of a spike that is more evident in fainter signals and seems to be asymmetric. One possible explanation for the absence of the delay time is that when the incident beam is small and focused, the delay time accumulated by every "slice" of the beam profile compensates. The absence of a clear time delay could be explained considering that the AOD is placed exactly in the focus of the laser beam. In such a configuration, different portions of the beam reverse and the time delay compensates, in such a way that the time delay accumulated by each ray is the same and it is not distinguishable from all the others. This inversion does not happen if the AOD is placed away from the focus. In addition, if the ripple that is visible especially in the signals of one side of the beam is due to the presence of the actuator (that is indeed closer to one side of the beam than the other and may induce an asymmetric behaviour), we expect to see it on the photodiode in different sides of the beam depending on whether the AOD is placed before or after the position of the waist. If the AOD is positioned after the focus, the side ray that is closer to the actuator will remain on that side, while if this ray is first deflected and then travels through the beam waist it will switch its position and will be observed on the opposite side.

To test this hypothesis we performed a few more measurement on a laser beam whose size in the beam waist is $w_x = 102\mu$m. We captured the traces of the rise up of the signal placing the AOD in different position along the propagation axis, and for every position three traces were taken, two at the sides of the beam and one in the center. First of all we tried to place the AOD in the z coordinate corresponding to the beam waist, then we moved it 16.4 cm back and forth. Because of the high focusing of the laser beam, its divergence is very fast and we have to measure again the size of the beams in the second and third position. In all the three pictures 4.27 the blue, yellow and green traces are related respectively to the left, center and right side of the beam profile observed with the photodiode placed on a translation stage, thus allowing us to distinguish them and to point out possible different behaviour among the measurements. Furthermore, the time scale is different in the three images so the distance between the traces is different and depends on how close the AOD was positioned. We can extract two important pieces of information from these pictures: first of all the hypothesis of inversion between the sides of the beam profile is confirmed since the measurements before and after the beam waist show the ripple in opposite positions: the

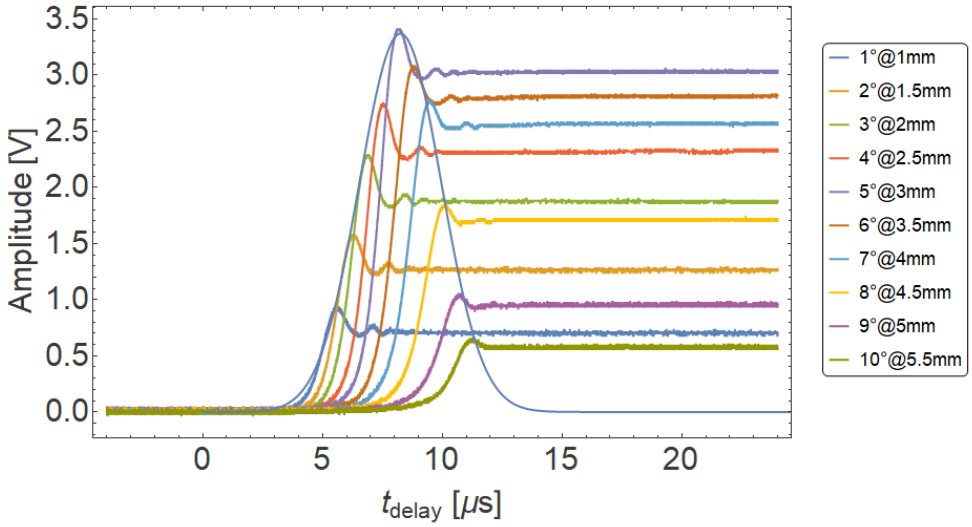

(a) Different portions of the deflected beam show different delay times for 2 mm beam waist.

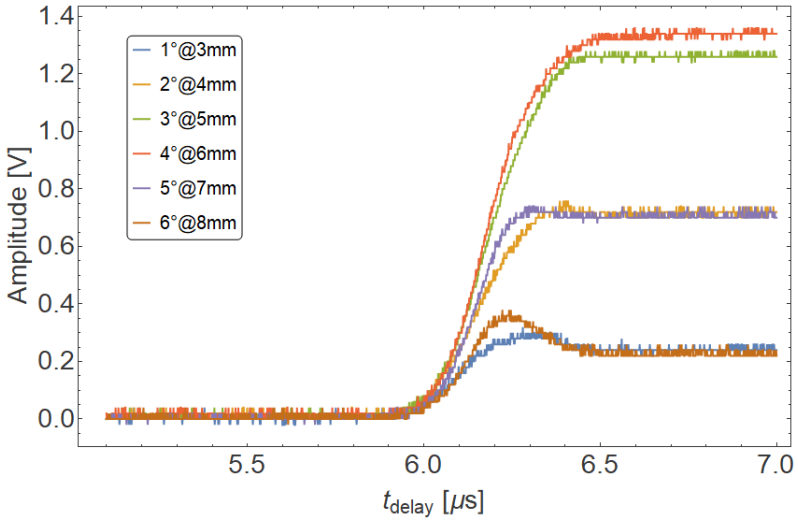

(b) Different portions of the deflected beam have approximately the same delay time for 0.1 mm beam waist.

Figure 4.25: Time-delay dynamics observed for two different beam sizes. The delay introduced due to the finite propagation of the sound wave is clearly visible for a large beam (2 mm), while it is not for a small beam (0.1 mm).

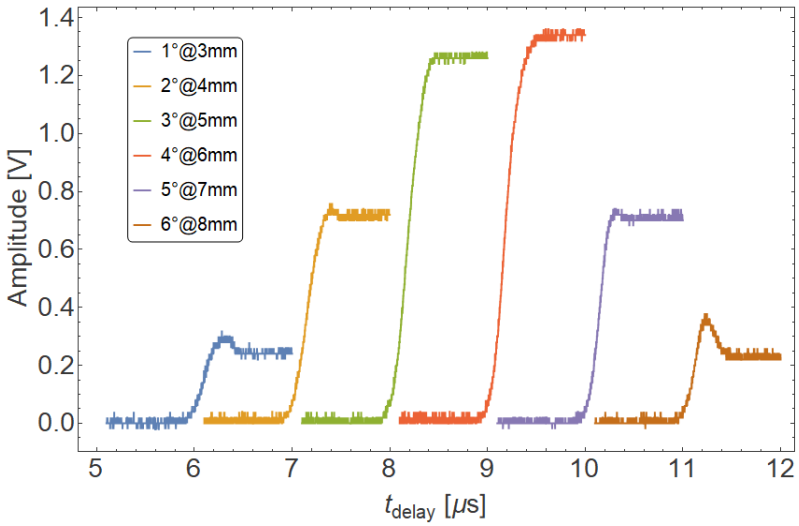

Figure 4.26: Traces measured for different positions of the photodiode artificially shifted to show their shape.

green trace in figure 4.27b shows the ripple and presents lower delay time than the yellow and blue traces, while in figure 4.27c the green one has the higher delay time and the ripple is shown by the blue trace. Since the ripple in the measurement after the beam waist (figure 4.27b) shows up in the right tail of the beam profile, this transient effect can be attributed to the acoustic wave investing the first part of the beam encountered (the piezoelectric actuator in the AOD is on its right side). In figure 4.27c the side that we identify as the "right side" of the beam does not present the ripple, this meaning that in AOD's crystal that was on the opposite side with respect to the actuator and passing through the beam waist the sides got inverted. As for the remaining picture (4.27a), the ripple appears in the right tail, suggesting that the crystal position along the propagation axis was still slightly beyond the beam waist. The difference between the two situations is that in the picture 4.27a the AOD is very close to the beam waist position.

We can convert the measured delay time again into a spatial distance thanks to the sound velocity and compare this distance with the measured sizes of the laser beams. Figure 4.27b corresponds to the AOD placed 16.4 cm after the beam waist, where the measured size of the beam is $w_x = 505\mu$m. The total delay time between the two sides of the beam is approximately $\Delta\tau = 780$ns that corresponds to a spatial size of 507 μm (using 650 m/s for the conversion). Figure 4.27c corresponds instead to the AOD placed 16.4 cm before the beam waist, where the measured size of the beam is $w_x = 371\mu$m. The total delay time between the two sides of the beam is approximately $\Delta\tau = 550$ns that corresponds to a spatial size of 358 μm (using 650 m/s for the conversion). The agreement is good, even though just three points were considered for both the measurements. This is valid also for small sizes of the laser beam unless the AOD is placed exactly in the position corresponding to the beam waist. The 0.1 mm beam waist, in fact, is subject to some sort of mixing of its parts that do not propagate in parallel anymore.

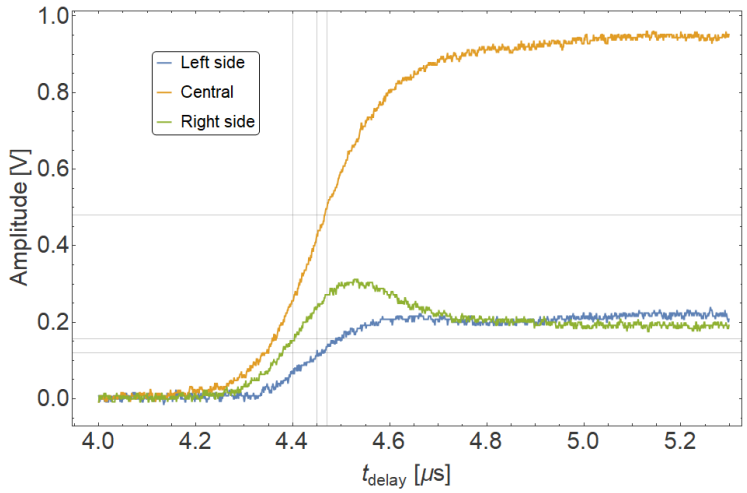

(a) AOD is placed in the position corresponding to the beam waist.

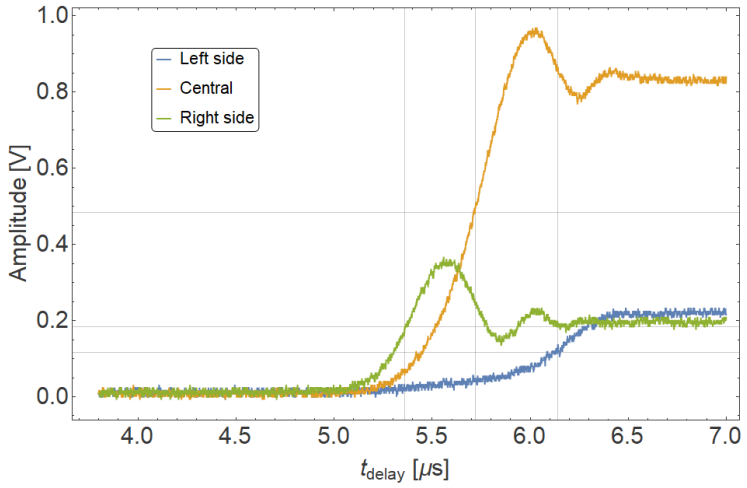

(b) AOD is placed 16.4 cm after the position corresponding to the beam waist along the propagation axis.

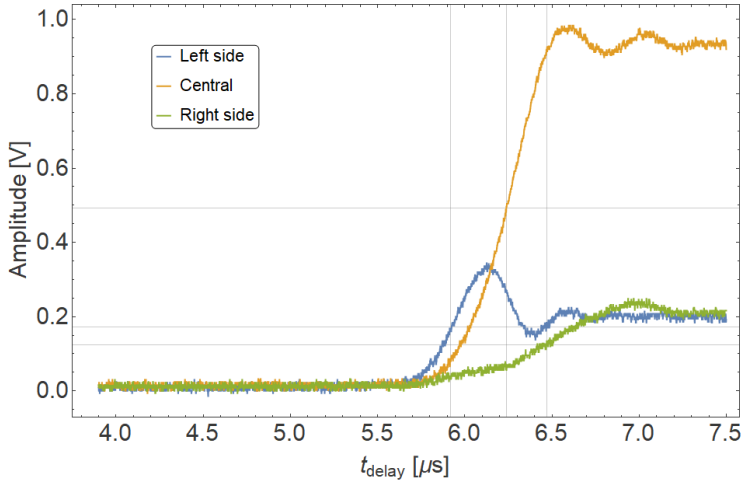

(c) AOD is placed 16.4 cm before the position corresponding to the beam waist along the propagation axis.

Figure 4.27: Delay times compensate only when the AOD is close to the beam waist.

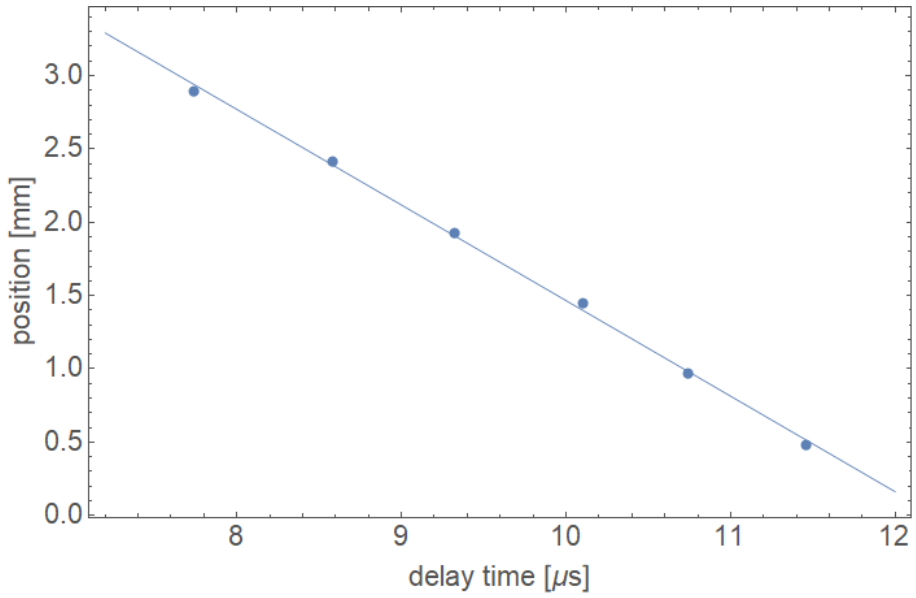

Figure 4.28: Linear fit superimposed to the measured photodiode displacement plotted versus the measured delay times.

4.4.3 Sound velocity in the crystal

In this subsection we exploit the dynamical effects of the AOD to measure directly the sound velocity of the acoustic wave in the AOD's crystal. In order to measure the sound velocity we send an RF signal, that is suddenly switched between two frequencies, to the AOD. The rise time of the RF signal is negligible (< 10 ns), but since the acoustic wave propagates at finite velocity, it takes a few μs to travel on a lengthscale of a few millimiters, compatible with the size of the laser beam waist. A photodiode with a small sensor (PDA8A2) with a 0.8 mm diameter is used to collect the light deflected by the AOD[1]. The photodiode can be moved perpendicularly to the propagation axis of the deflected laser beam and collects the light coming from different zones of the beam that were deflected at different times, due to the finite sound velocity in the medium. This allows us to measure the time delay between the moment in which the signal of the photodiode rises and a common reference time (the switching time of the RF signal) as a function of the displacement of the photodiode on the translation stage. The sound velocity can be obtained performing a linear fit of the position of the photodiode versus the delay time. The delay times were measured directly for different positions of the photodiode. The linear fits on these data are reported in figure 4.28, and the resulting estimated sound velocity (the slope of the line) is $v_s = (-0.652 \pm 0.013) \frac{\text{mm}}{\mu\text{s}}$. In figure 4.28 we see that the acoustic wave first hits one side of the beam, the one closer to the actuator, and then crosses the whole beam. The slope of the fitted line is consistent with the expected sound velocity equal to 650 m/s. Other

[1] The experimental apparatus is the one presented in figure 4.23 using equal focal length lenses f1 and f2.

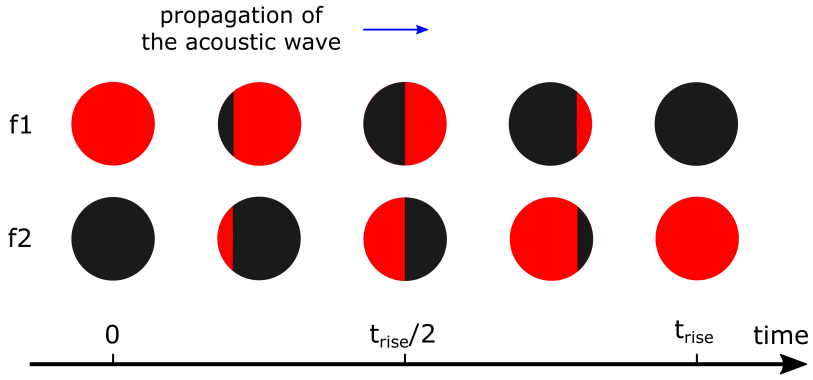

Figure 4.29: An AOD driven by an RF signal that switches periodically between two frequencies f1 and f2 produces two deflected beams at the angles corresponding to the frequency values. The dynamical behaviour during transients is well described by an eclipse model, where the acoustic wave determining the deflection angle propagates through the laser beam from one edge to the other.

similar tests were performed, in particular measuring the delay time from the reference to the falling down of the signal instead of the rising, for which similar results were obtained. The importance of these observations is that they validate an eclipse-like model for the dynamics of the switching of frequencies, that is shown in figure 4.29.

4.4.4 Modulation in a fast periodic switching

In this subsection we want to characterize the shape of the modulation of the signal relative to the beam deflected by the AOD when this is guided by an RF signal that is switched between two frequencies. The signal, observed with a photodiode (PDA8A2) that is connected to an oscilloscope, will be characterized by a finite rise time, as described in the previous subsections. This characterization is useful for the simulations in chapter 3 that regard the time-averaged potential. In particular, we study the time dependence of the power of the deflected beam as a function of the period over which the RF driving signal alternates between two frequencies. We used an AWG to drive a pair of crossed AODs with a FSK (frequency-shift keying) modulation on the carrier RF signal. This kind of modulation allows us to alternate the carrier frequency between two values, that we set to 90 MHz and 110 MHz, at desired key frequency (the frequency at which the modulation is carried out). We chose for the key frequency values of 10, 50, 80, 90, 100, 110, 120, 150 and 250 kHz. The modulation is performed in phase on both the AODs in such a way that the laser beam is deflected to the (90, 90) MHz spot for half of the time and (110, 110) MHz for the second half of the period. This is just the ideal case, because the transition between one frequency and the other is limited by the rise/fall time of the signal, that is in turn limited by the size of the beam in the crystal. Transient effects produce the unwanted *ghost*

spots, whose study and characterization is carried out in chapter 5. We placed a photodiode on the path corresponding to the (110, 110) MHz spot in order to measure on an oscilloscope the traces related to these modulations. The light is focused on the photodiode with a lens that guarantees that the whole laser beam is contained in the sensor. The signal is recorded with an oscilloscope and for each key frequency we capture a trace. We take also the trace for key frequency equal to 0, namely for a static beam, that will be the amplitude reference for all the other signals.

The characterization of the modulation profile is performed both for the standard beam size ($\sim$ 1 mm) and for a reduced size ($\sim$ 0.5 mm). These two configurations are the ones for which we performed the simulation implementing a time-averaged potential in chapter 3. For the smaller beam size one more key frequency was added to the measurement, namely 200 kHZ.

In figure 4.30 the measured traces for the modulation of the amplitude of the deflected laser beam at different key frequencies are reported, in the case of the 1 mm beam. To make the plots understandable the measurements are reported in two different pictures. The modulation is a square wave for low key frequency (10 kHz), while it gets smoothed at higher key frequencies. The blue trace represents the deflected power for a static beam and we notice that the dynamic modulations reach this value for key frequencies up to 90 kHz. At higher key frequency instead, the signal does not reach the value of the not modulated beam, because the period becomes compatible with the rise time of the signal and there is not enough time to reach the maximum amplitude. Anyway, the modulation maintains its characteristic shape up to 150 kHz, while for 250 kHz key frequency it gets also distorted. In figure 4.31 we see the advantage of using a smaller beam waist: the traces reach the maximum amplitude for key frequencies up to 150 kHz (the green, orange and purple traces in figure 4.31b even seem to overcome the static amplitude, but this may be ascribed to long-term fluctuations of the laser source emission power) and high key frequency modulations are less distorted than in the 1 mm beam waist case.

An analytic expression of such modulations is important, because the time modulation of the trapping potential implemented in all the time-averaged simulations performed in chapter 5 is based onto this kind of equation. A simple analytic expression offers a huge simplification in the time-averaged potential simulations. In order to derive an analytic expression, we used a simplified scheme and approximated a period of the modulation with a trapezium. The parameters needed for this simplified expression are the key frequency that determines the period length, the rise time of the signal that gives the slope of the rising and falling sides of the trapezium, and the time for which the modulation stays at constant value. An example of such a modulation compared with the measured signal is reported in figure 4.32. For every key frequency I determined the best set of parameters that can be used to exemplify the modulation of the deflected power.

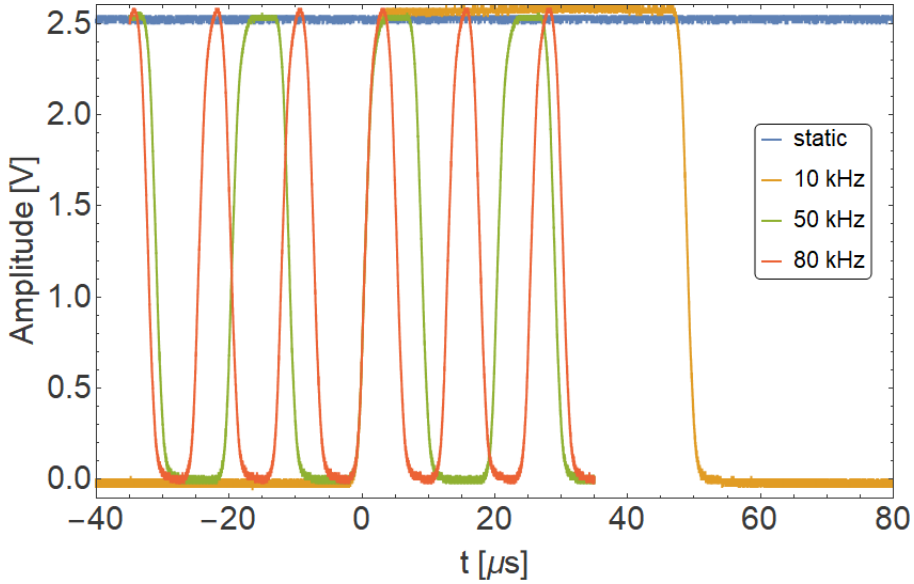

(a) Static beam compared with dynamically tuned at different key frequencies.

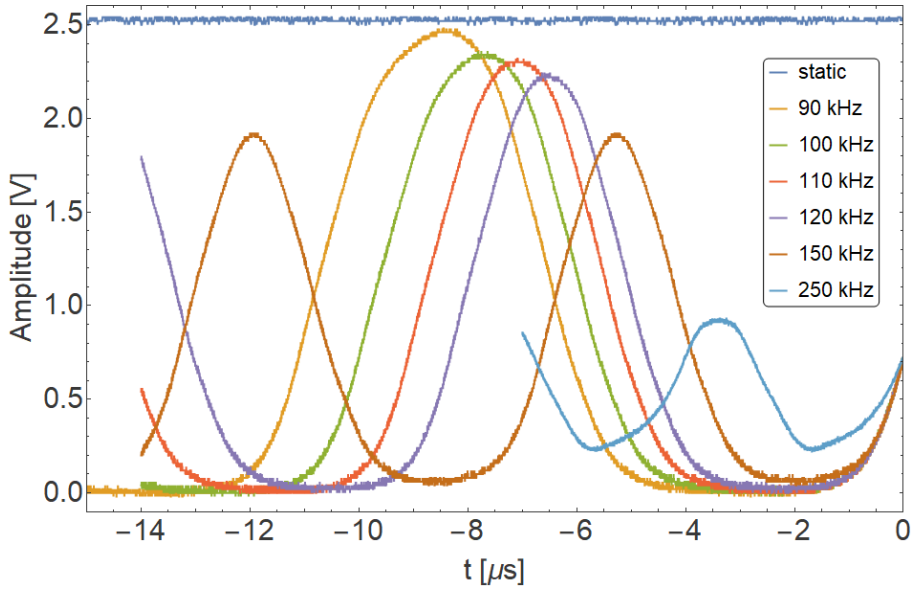

(b) Static beam compared with dynamically tuned at different key frequencies.

Figure 4.30: Amplitude modulation for the deflected beam at different key frequencies.

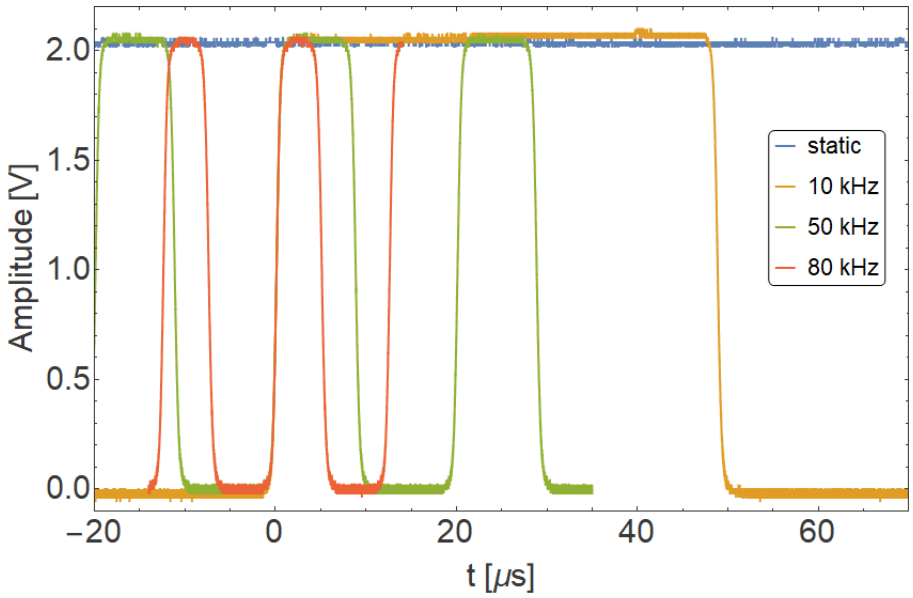

(a) Static beam compared with dynamically tuned at different key frequencies.

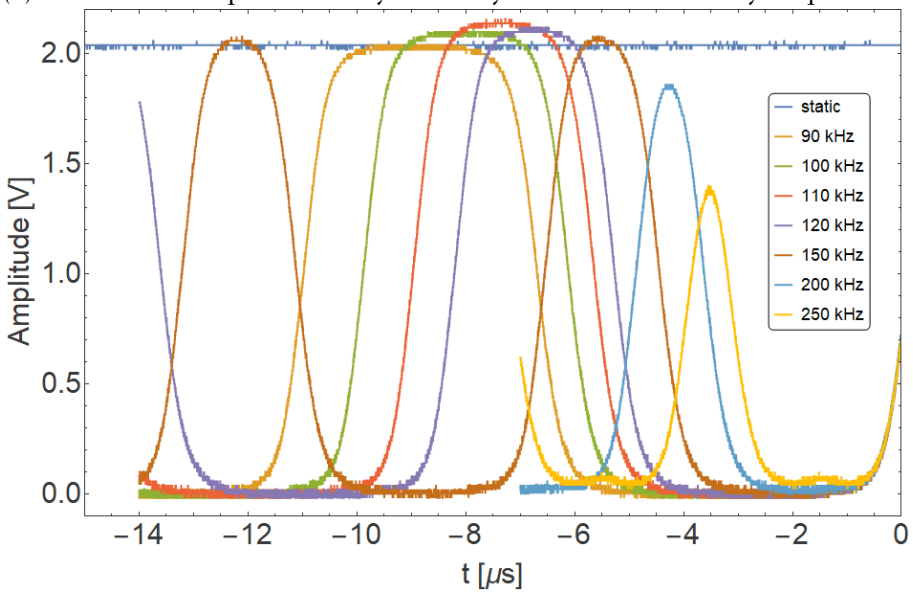

(b) Static beam compared with dynamically tuned at different key frequencies.

Figure 4.31: Amplitude modulation for the deflected beam at different key frequencies.

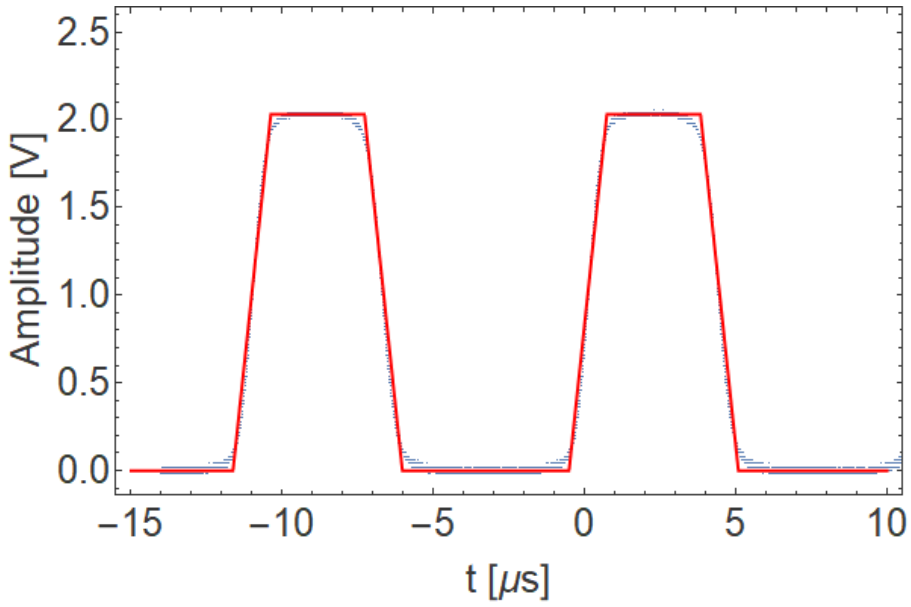

Figure 4.32: Example of the simplified modulation superimposed to the 100 kHz signal for a 1 mm beam.

Considerations about the shape of the modulation

In the following paragraphs we describe the shape of the analytic modulation depicted in figure 4.32, with particular attention to its duty cycle. Since the FSK modulation operates with 50% duty cycles, we would expect the modulation of the deflected power to show equal time intervals in which the signal is on and off. These intervals are instead unbalanced as we can see in figure 4.32, where the flat segment representing the signal to its maximum value is clearly shorter than the zero amplitude one. This effect is more evident for high key-frequencies, for which the rise time and the static phase of the AOD are comparable. If the beam is deflected by two AODs, the modulation is given by two in-phase modulations. To confirm that the modulation that we see is really given by the product of two symmetric modulations in-phase, we measured the trace relative to the modulation on one single AOD at once (for 1 mm beam waist) and compared the square modulus of such modulation with the traces in figure 4.30. In figure 4.33 the traces related to the modulation on a single channel and on two channels are reported. The two channel modulation is extremely similar to the square modulus of the single channel modulation. Such an unbalanced modulation (for two channels) is thus just the straightforward result of the product of two symmetric effects on the two AODs. As it will be described in chapter 5, the physical reason for which the power of the beam deflected by a couple of AOD is smoothed during transient times is that the time-averaged potential modulation gives rise to additional spots, that we called ghost spots, that are produced during the transient times. Hence, the overall laser power is distributed not only between the two spots that are expected for an ideal time-averaged potential with zero rise time, but a part of the light is also deflected in the additional ghost spots.

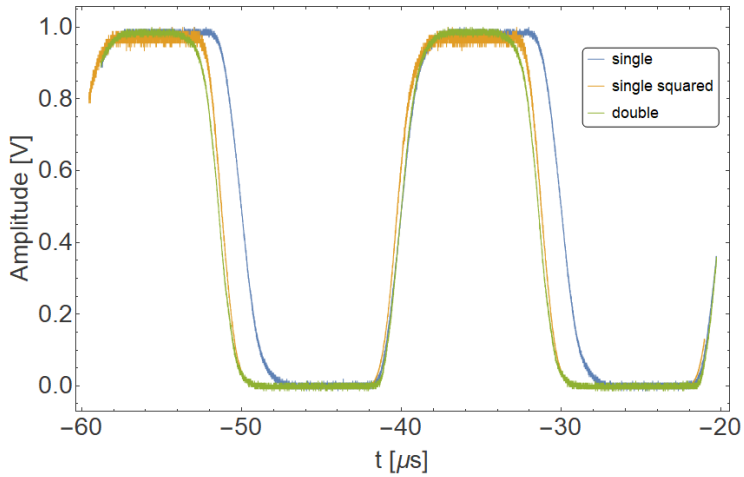

(a) Single and double channel modulation at key frequency equal to 50 kHz.

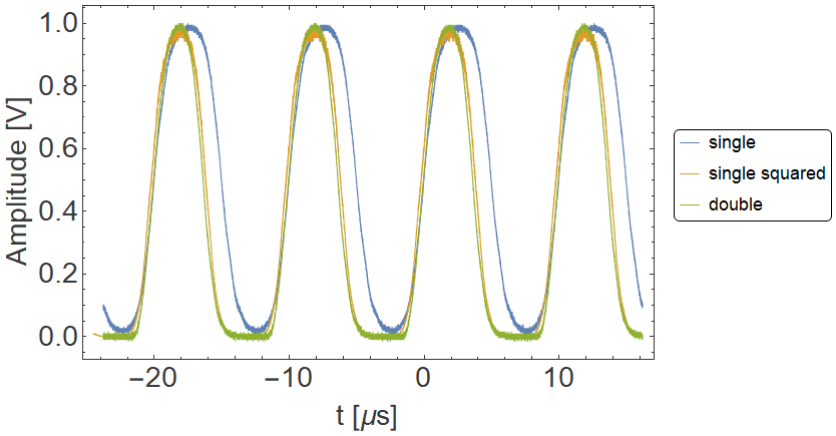

(b) Single and double channel modulation at key frequency equal to 100 kHz.

Figure 4.33: The two channel modulation (green trace) can be obtained as the square modulus (yellow trace) of the single channel modulation (blue trace).

Chapter 5

Generation of tweezers pattern

In this chapter I will present the experimental realization of arrays of optical tweezers. The setup is based on a couple of crossed AODs and both static arrays and dynamic ones, exploiting the time-averaged technique, were realized. I also discuss the resolution and the bandwidth of the apparatus, comparing the measured values with the theoretical ones introduced in chapter 4. The experimental setup is presented in figure 5.1 and includes the acousto-optic deflectors that create the multiple beams pattern, a telescope and a microscope objective. The tweezers created by the AODs and focused by the objective are imaged onto a CCD camera whose position can be adjusted using a translation stage. The objective used for these measurements is a Plan Fluor 10x/0.30 manufactured by Nikon. The effective focal length of this objective is 50 mm and its numerical aperture is 0.30. The AODs are driven by two RF signals generated by the two outputs of an arbitrary waveform generator (AWG). The radio frequency components of this signals determine the number and the deflection angles of the deflected beams, following the equation (4.5). The two AODs are separated by a 4f optical system. A second telescope is placed between the second AOD and the microscope objective. This telescope is composed by a scan lens and a tube lens, introduced in chapter 3 and can be leveraged to change the beam size before

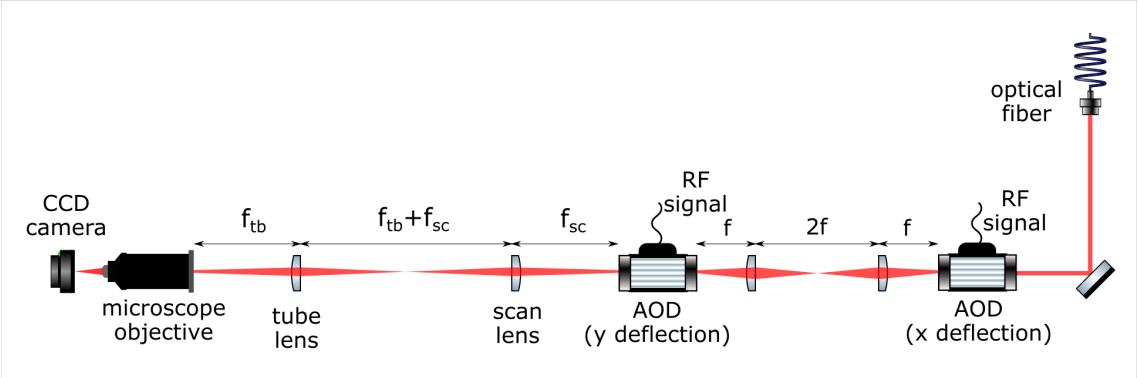

Figure 5.1: Experimental apparatus used for the creation of all the tweezer arrays presented in this chapter.

the objective to change the dimensions and the separation between tweezers (see equations (3.14) and (3.15)). To conclude the optical setup, a microscope objective focuses the array of deflected beams to the micrometer lengthscale and the array of optical tweezers is imaged by a camera. The camera is placed exactly at the working distance of the microscope objective, in the position where the atoms in the final experiment will be trapped. Differently from the schematic apparatus depicted in figure 3.1, in which the tweezers are focused in the glass cell by the objective, and the camera used for the imaging is placed after a second microscope objective, now the CCD camera is placed directly after the first objective in order to observe the tweezers.

5.1 Static patterns

We present now the realization and imaging of a static pattern of optical tweezers made up of 100 sites, presented in figure 5.2. The pattern is a square array, and the acousto-optic deflectors are used statically, and the spots are equally spaced by Δf=4 MHz in such a way that a wide range of the bandwidth of the devices is covered, from 84 to 120 MHz. The Rf signal is generated by an AWG as a sum of ten sine functions for these frequency values and it is the same for both the AODs. The image is captured with the camera that is placed after the microscope objective, as described in figure 5.1. In figure 5.2, the spot at the top right is corresponding to f_{RF}=84 MHz on both the AOD dedicated to the horizontal deflection and the one dedicated to the vertical deflection, while the spot at the left bottom is the combination of f_{RF}=120 MHz for both the devices. Before capturing this image, we optimized the efficiency of the 2D deflection system, following the procedure described in section 4.3. The final result is a large array with uniform amplitudes, except for a slight lack in efficiency for the largest radio frequency values. Moreover, the array is a regular square array and all the spots are well focused, meaning that the microscope objective and all the lenses are well aligned and the camera is placed correctly at the working distance of the objective.

In the context of the generation of static patterns it is important to determine the resolution limit of an experimental apparatus like the one presented in figure 5.1. We performed a measurement in which five equally spaced tweezers are generated in a row. In order to verify the scaling of the distance between tweezers and their waist as a function of the ratio between focal lengths f_{scan}/f_{tube}, following equations (3.15) and (3.14), a scan lens and a tube lens with different focal lengths were considered. In particular, we chose f_{scan} = 200 mm and f_{tube} = 500 mm, in such a way that the beam waist of the laser, whose size in the position of the AOD is w_{AOD}=1 mm, is scaled to $w_i \simeq$0.4 mm between the tube lens and the microscope objective. The 1D pattern is reported in figure 5.3, where the frequency separation between the spots is equal to 1 MHz. Note that under these experimental conditions we are exploring the resolution limit of the optical system. The Rayleigh criterion for resolving two spots generated at wavelength λ,

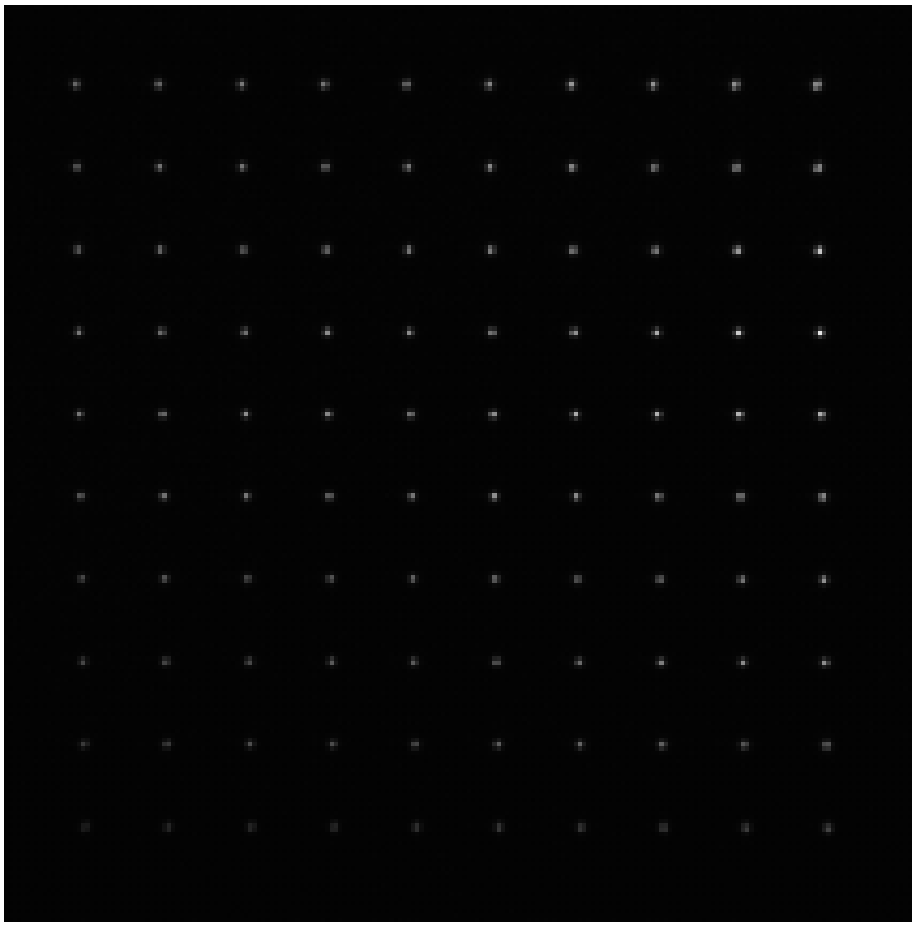

Figure 5.2: Square array composed of 10x10 spots equally spaced by 4 MHz.

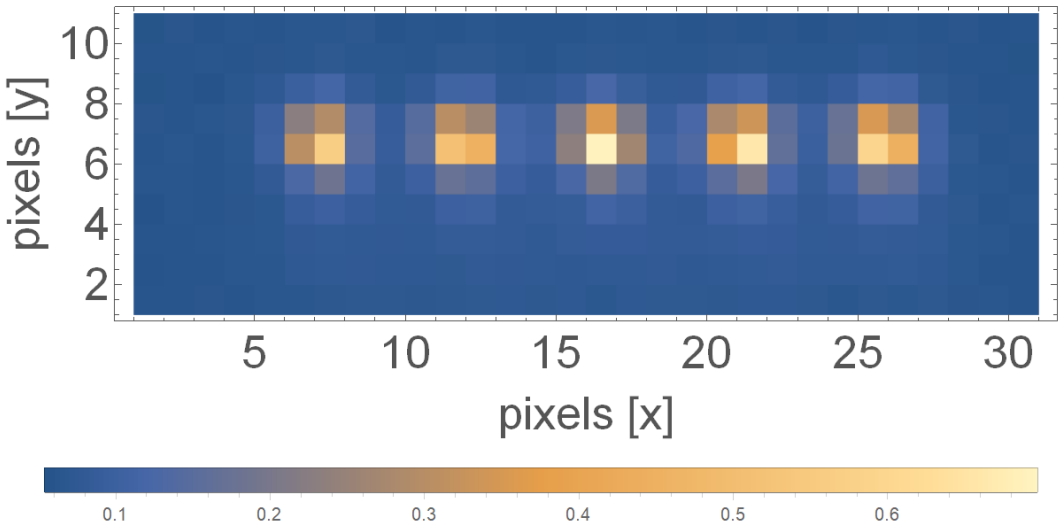

Figure 5.3: 1D pattern obtained at the resolution limit of the apparatus.

passing through a circular aperture D is the following:

$$\Theta_0 = 1.22\frac{\lambda}{D} \tag{5.1}$$

Recalling the expression for the angular separation $\Delta\theta$ (equation (4.6)) between a pair of tweezers generated for RF frequencies that differ for an amount Δf, we can express the Rayleigh limit as a function of the radio frequency separation. Imposing that $\Delta\theta > \Theta_0$, we get:

$$\Delta f > 1.22\frac{v}{D} \tag{5.2}$$

In our case the diameter of the laser beam, that can be approximated with twice the waist of the beam before the objective, is $2w_i$=0.8 mm. Since the back aperture of the objective is much larger, above 20 mm, the dimension of the aperture D in equation (5.2) can be identified with the diameter of the laser beam. Substituting the experimental parameters in (5.2), in particular considering the datasheet value for the sound velocity in the crystal v=650 m/s, we obtain that Δf >1 MHz, that is exactly the frequency separation for which the pattern is obtained.

We then fitted a sum of five Gaussian profiles to the data, obtaining the parameters reported in table 5.1. The waists of the five spots and the separation between sites are reported first in pixels, as they are obtained from the fit, and are then converted to lengths considering that the side of the camera pixel is equal to 5.2 μm. Finally, we can compare the measured parameters of the tweezers

	Size (pixels)	Size [μm]
w1	1.6 ± 0.3	8.5 ± 1.6
w2	1.9 ± 0.3	9.9 ± 1.6
w3	1.6 ± 0.2	8.5 ± 1.0
w4	1.9 ± 0.3	9.7 ± 1.6
w5	1.8 ± 0.3	9.5 ± 1.6
d_{12}	4.6 ± 0.3	23.8 ± 1.6
d_{23}	4.6 ± 0.3	23.9 ± 1.6
d_{34}	4.7 ± 0.2	24.4 ± 1.0
d_{45}	4.6 ± 0.3	23.8 ± 1.6

Table 5.1: Waist and distance between neighbouring tweezers reported with fit errors both in pixels and in μm

with the expected ones. Note that this measurement was carried out exploiting a laser wavelength λ= 786 nm. Substituting our parameters in equations (3.14) and (3.15), we obtain:

$$w_{theo} = 5.01\,\mu m = 1\,pixel \qquad d_{theo} = 24.2\,\mu m = 4.7\,pixels \tag{5.3}$$

While the measured tweezer separation are in good agreement with the theoretical value, the size of the spots are not. It is possible that, since the tweezer occupies just two pixels (the diameter of the tweezer is twice its waist), the fit

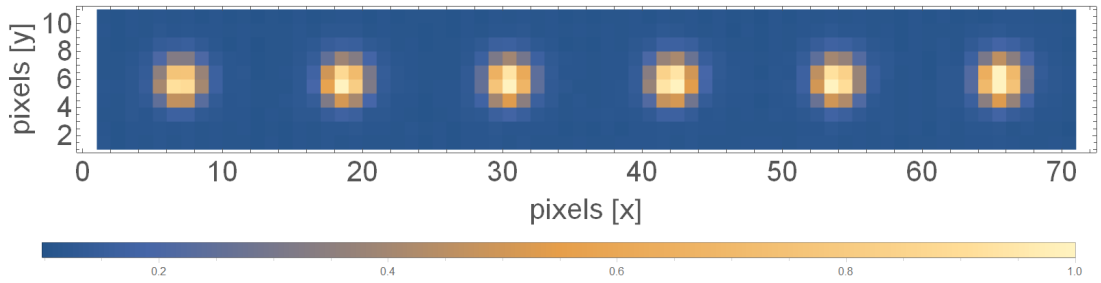

Figure 5.4: 1D pattern composed of six equally spaced tweezers.

is not able to give a good estimate of the tweezer's waist. Another possibility is that the camera was not positioned exactly on the focal plane of the microscope objective and then the measured size of the spots is not at its minimum.

We then performed one more measurement of this kind, by changing the tube and the scan lenses. We generated now a linear pattern made up of just three equally spaced spots. The experimental parameters are now f_{scan}=200 mm, f_{tube}=200 mm, Δf= 1 MHz and λ= 786 nm. The image of the pattern is show in 5.4: The procedure followed for the image analysis is the same of the previous measurement. We fit a sum of six Gaussian profiles to the data and report the waist and distance parameters in table 5.2. Comparing these values with the

	Size (pixels)	Size [μm]
w1	2.06 ± 0.12	10.7 ± 0.6
w2	2.10 ± 0.11	10.9 ± 0.6
w3	2.13 ± 0.11	11.1 ± 0.6
w4	2.11 ± 0.10	11.0 ± 0.6
w5	2.07 ± 0.10	10.8 ± 0.5
w6	2.15 ± 0.10	11.2 ± 0.5
d_{12}	11.73 ± 0.11	61.0 ± 0.6
d_{23}	11.72 ± 0.10	60.9 ± 0.5
d_{34}	11.71 ± 0.10	60.9 ± 0.5
d_{45}	11.70 ± 0.10	60.8 ± 0.5
d_{56}	11.72 ± 0.10	60.9 ± 0.5

Table 5.2: Waist and distance between neighbouring tweezers reported with fit errors both in pixels and in μm

theoretical ones obtained again from equations (3.14) and (3.15), we have:

$$w_{theo} = 12.5\,\mu m = 2.4\,pixels \qquad d_{theo} = 60.5\,\mu m = 11.63\,pixels \tag{5.4}$$

In this case just the distance between tweezers is consistent with the theoretical ones. On the other hand, the measured tweezer waists are all smaller than the predicted size. A possible issue that could cause this discrepancy is a non perfect alignment of the camera with respect to the microscope objective. Furthermore, the size of the tweezers is comparable with the pixel size, so the fit procedure may not be able to determine its dimensions properly. The correct estimate of the

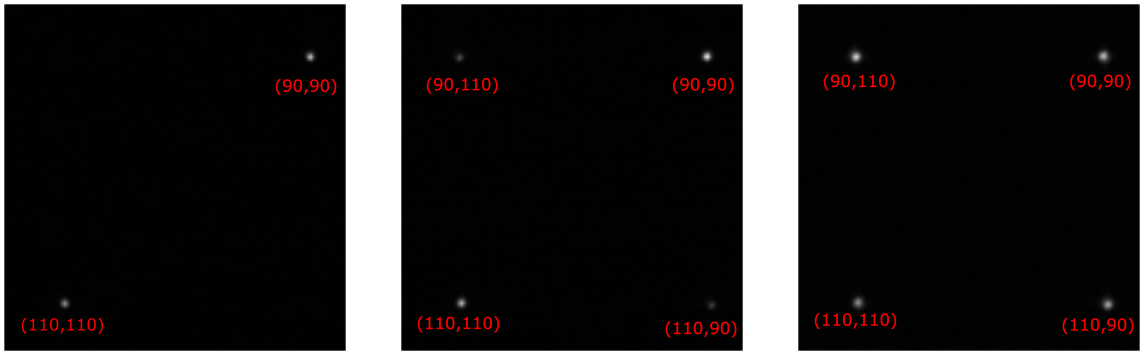

(a) Tweezers generated via a time-averaged potential for ν=10 kHz.

(b) Tweezers generated via a time-averaged potential for ν=100 kHz.

(c) Tweezers generated via a time-averaged potential for ν=250 kHz.

Figure 5.5: Tweezers generated via a time-averaged potential for different ν values. The camera's exposure time is longer than the period of the modulation and allows us to all the spots, labelled with the RF frequency components (f_M,f_L), simultaneously.

distance between tweezers confirms the agreement with the geometrical optics equation (3.15).

5.2 Time-averaged patterns

In this section we introduce the realization of arrays of optical tweezers exploiting the time-averaged technique described in the previous chapters. First of all, we implemented this method in the easiest case, where the RF signal generated by the AWG is modulated periodically using the built-in FSK modulation mentioned in section 4.1 between a couple of frequencies, namely 90 MHz and 110 MHz. The same signal is sent in phase to both the acousto-optic deflectors that produce two spots, the first at 90 MHz on both the devices and the second at 110 MHz. The experimental setup used for the focusing and imaging of the tweezers is that of figure 5.1, and the size of the laser beam inside the AODs is 1 mm. Like in the simulations of the time-averaged trapping potential, we produced this two-spots pattern at different switching frequencies ν (see equation (3.24)). In figures 5.5a, 5.5b and 5.5c, the 110, 110 MHz spot is the one at bottom left of the image, while the spot at top right is the 90, 90 MHz one. These pictures are captured by a camera that is integrating the pattern for an exposure time much larger than the period of the modulation, in such a way to visualize the pair of spots simultaneously. While for slow modulations (ν ~10 kHz) the time-averaged potential works correctly and just the two desired tweezers are visible, for higher modulating frequencies two more spots show up and become comparable with the original ones for ν ~250 kHz in figure 5.5c. These "ghost" spots (that will be also called simply *ghosts* in the following) appear in correspondence of the two other vertices of the square array, as a combination of an RF frequency of 90 MHz on one AOD and 110 MHz on the other one. The presence of such spots can be understood recalling the behaviour of an AOD subjected to a periodic fast

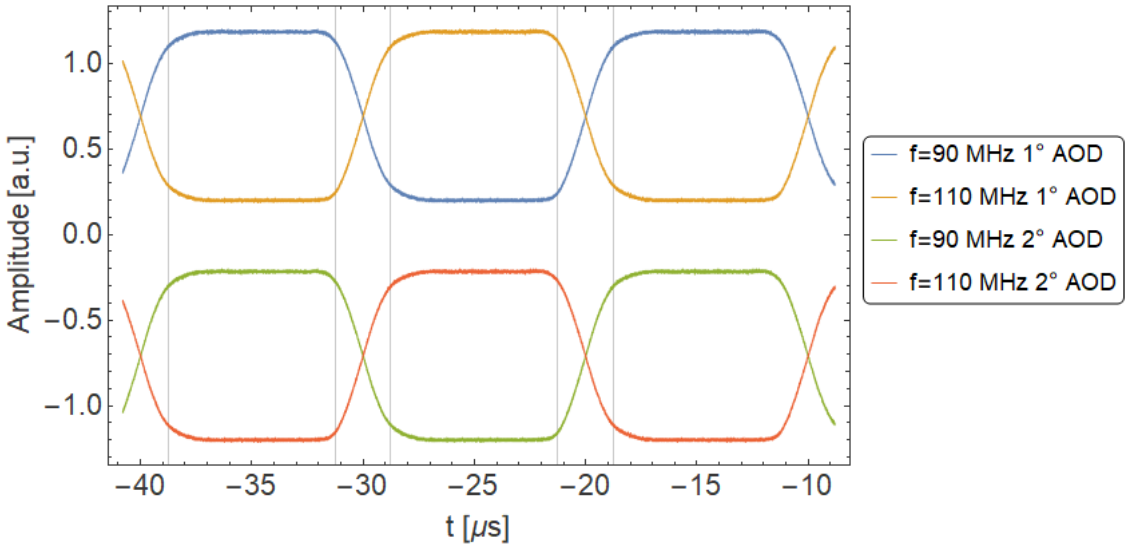

Figure 5.6: Measured amplitudes of a deflected beam that is subject to the frequency switching (ν= 50 kHz) of a single AOD. The traces are shifted vertically for a better visualization and the negative time values are referred to the set point of the oscilloscope. The blue and yellow traces represent the time-dependent amplitude modulation generated by the first AOD, while the green and red ones are related to the second AOD.

switching discussed in subsection 4.4.3 and shown in figures 4.30 and 4.31 for a beam waist in the position of the AOD equal to 1 mm and 500 μm, respectively. In these figures, in the case of small switching frequencies ν, the transient times are much smaller than the time during which the AOD works with each fixed frequency. The signal of the fotodiode appears indeed as a square wave on the oscilloscope. For higher switching frequencies, instead, the transient times becomes more compatible with the time of single frequency in the AOD. During transients the two RF frequencies are present at the same time on both the AODs, hence the devices deflect on two frequencies instead of one, causing the presence of ghosts. Since these ghost spots appear only during transient times, as it will be discussed further in the following, for small switching frequencies the time during which the ghosts are present is much less than time during which the *real tweezers* are produced, hence they are not visible on the camera, that integrates the counts for a long time. Increasing the switching frequency, the time during which the ghosts are deflected becomes larger with respect to the time for which the real tweezers are generated, thus becoming more and more visible on the camera.

In figure 5.6 the power amplitude modulations due to single AODs are plotted. A 1 mm laser beam in the position of the AODs is considered, thus resulting in a rise time of approximately 2.5 μs. In the first row the modulation for the first AOD are plotted in blue (90 MHz) and yellow (110 MHz), while the second row represent the same modulations for the other AOD. As seen in figure 4.33, when we consider RF signals that are in phase on the couple of AODs, the final amplitude modulation of the laser beam deflected by both the devices is the

product of the modulations on a single channel. Thanks to the scheme in figure in figure 5.6 we show what happens to the deflected beams during one complete period. Consider the combination of blue and green traces: these are in-phase amplitude modulations that account for the spot corresponding to 90 MHz RF frequency on both the AODs. Their product gives the maximum amplitude of the signal in the first half of the period and is zero in the second half. Similarly, the yellow and orange traces produce the spot at (110, 110) MHz for which the amplitude is zero in the first half of the period and it's maximum in the second half. These are the two desired spots at (90,90) MHz and (110,110) MHz expected in the case of an ideal time-averaged modulation with no transient time and instantaneous switching between the two RF frequencies. Nevertheless, the traces in figure 5.6 have nonzero transient times of approximately 2.5 μs, making the modulation non perfect. Taking into account the combination of out-of-phase signals, the blue and orange traces and the yellow and the green ones in figure 5.6, we see that their product is nonzero during the transient, differently from an ideal square wave modulation with zero rise time for which the product would be always zero. For example, during transient the blue trace and the orange one have simultaneously nonzero amplitudes. This means that while the first AOD is switching the RF frequency from 90 MHz to 110 MHz and two diffracted beams are present (one at 90 MHz and the other at 110 MHz), also the second AOD is switching from 90 MHz to 110 MHz and it is diffracting two beams instead of a single one. This combination will also introduce a beam at the combination of frequencies for the first and the second AOD of (90,110) MHz in addition to the desired beams at (90,90) MHz and (110,110) MHz. The same mechanism stand also for the yellow and green traces, that during the transient combine to produce an additional spot at (110,90) MHz. Note that the periodicity of the ghost spots, generated during the transient times, is doubled, since the combination of out-of-phase signals happen every half of the original period.

Now we can plot the product of two out of phase modulations to understand the shape of the modulation of the spots that come out of the transient effects described above. Consider for example the figure 5.7, where the blue trace is the amplitude modulation of the 90 MHz beam produced by the first AOD and the yellow trace is the amplitude modulation of the 110 MHz produced by the second. The green trace is obtained as the product of the blue and yellow ones and represents the amplitude modulation of the additional spots rising from transient effects, that we named *ghosts*. The ghosts are visible in figure 5.5 and become more relevant for high switching frequencies ν if compared to the original tweezer spots. The higher is ν, the shorter is the period of the modulation and, since the slopes of rising and falling signals are fixed by the dimensions of the laser beam, transient effects become more and more important as the period decreases.

We repeated the measurement in figure 5.5 reducing the beam waist to 500 μm for different key frequency values. The tweezers pattern are reported in picture 5.8. The reduced beam waist results in a smaller rise time and, since the ghost spots are generated during the switching time, their amplitude decreases for smaller rise times, as we can see in figure 5.8. In particular, in the case of

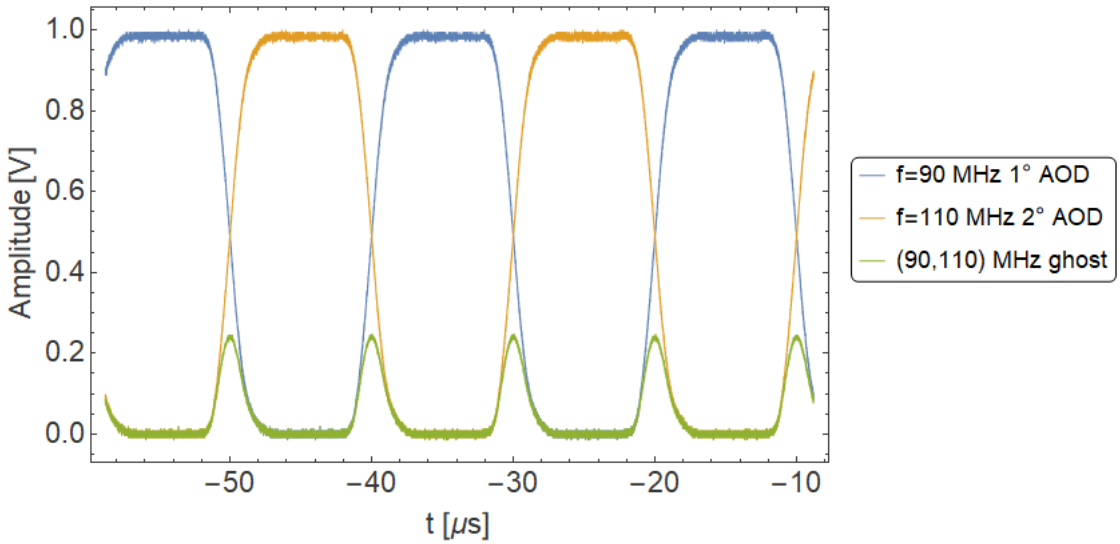

Figure 5.7: When two RF signals are out of phase there is still a superposition due to the finite rise and fall times in the AODs.

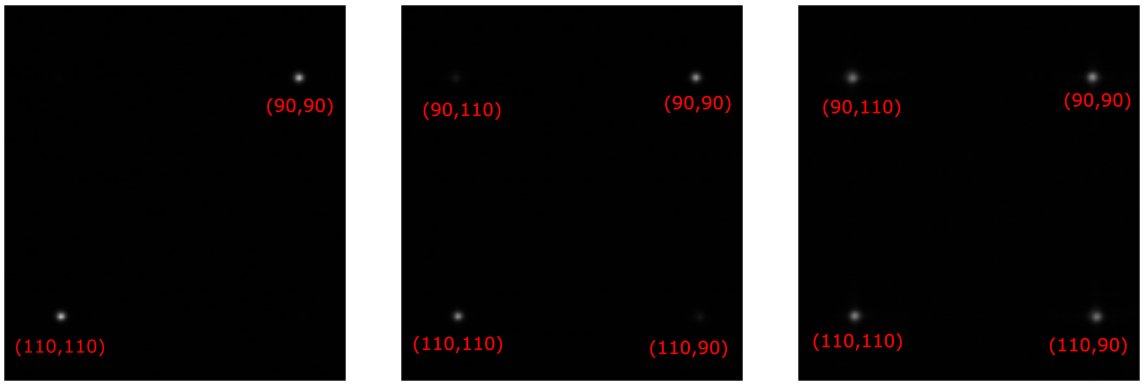

(a) Tweezers generated via a time-averaged potential for ν=10 kHz for the smaller beam waist.

(b) Tweezers generated via a time-averaged potential for ν=100 kHz for the smaller beam waist.

(c) Tweezers generated via a time-averaged potential for ν=250 kHz for the smaller beam waist.

Figure 5.8: Tweezers generated via a time-averaged potential for different ν values and a beam waist reduced to 500 μm. The camera's exposure time is longer than the period of the modulation and allows us to all the spots, labelled with the RF frequency components (f_M,f_L), simultaneously.

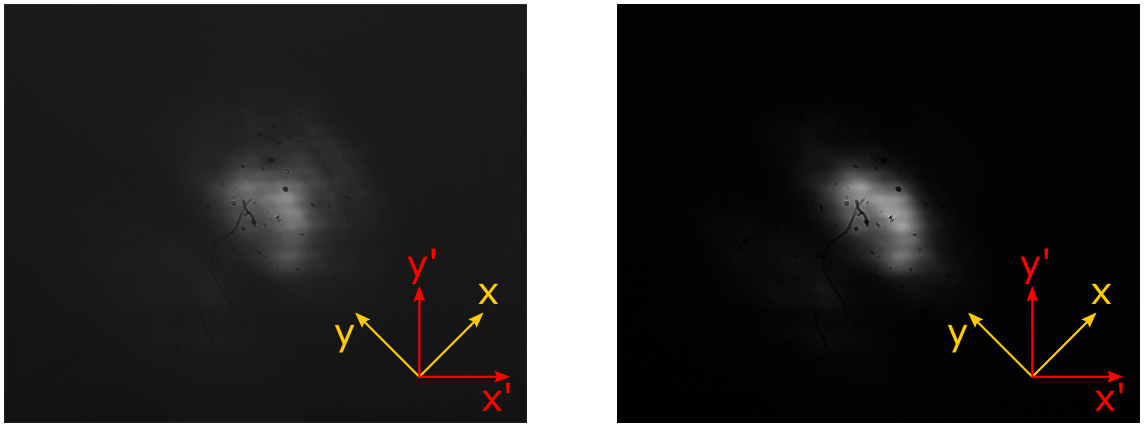

(a) Ghost observed for a modulation at ν=10 kHz for a 1 mm beam waist.

(b) Ghost observed for a modulation at ν=250 kHz for a 1 mm beam waist.

Figure 5.9: Ghost spots measured at different switching frequency values. The spot is warped and presents two lobes.

ν=100 kHz the ghost spots are no more visible, differently from the previous case where we considered a 1 mm beam waist. In order to understand the geometrical properties of the additional ghost spots, we observe directly both the tweezer and the ghost spots with a camera, placed before the objective.

5.2.1 Imaging of ghost spots

A ghost spot obtained for a laser beam waist equal to 1 mm is reported in figure 5.9 for two different switching frequency values, 10 and 250 kHz. The camera is placed before the objective in order to observe the beam on the millimiter lengthscale, instead of a micrometer one. The spot is clearly warped diagonally and it seems to be composed of two different lobes. The warping of the spot is even worse for high switching frequencies. For completeness, the image of the beam deflected at the position of the tweezer, captured before the objective, is reported in figure 5.10 for the same pair of switching frequencies. The ordinary spot is distorted too for high frequencies and a Gaussian shape for the optical tweezer cannot be assumed anymore. Under these extreme conditions the tweezers, warped by the fast modulation of the time-averaged technique, are not suitable for trapping the atoms because the properties of the trap, in particular the trapping frequencies, cannot be assumed to be uniform among all the spots. Furthermore, the trapping frequencies will strongly depend on the switching frequency value since the distortion of the spot is different for different frequencies. The distortion of the spots is diagonal because the spots generated by the time-averaged potential are positioned at two opposite vertices of a square geometry. The ghosts appear to be squeezed diagonally in the central part of the spot, while the real spots present a whole in the center due to the appearance of the ghost. For high switching frequencies the central part of the beam contributes mainly to the ghost spot, while the edges are present mainly in the conventional spot. This is particularly bad, because in this regime the real spot becomes similar to a

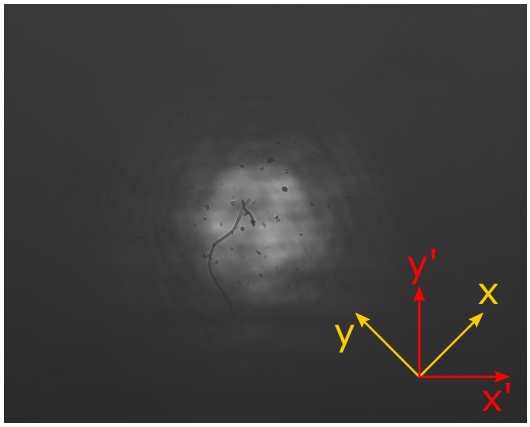

(a) Spot deflected in the position of a tweezer observed for a modulation at ν=10 kHz for a 1 mm beam waist.

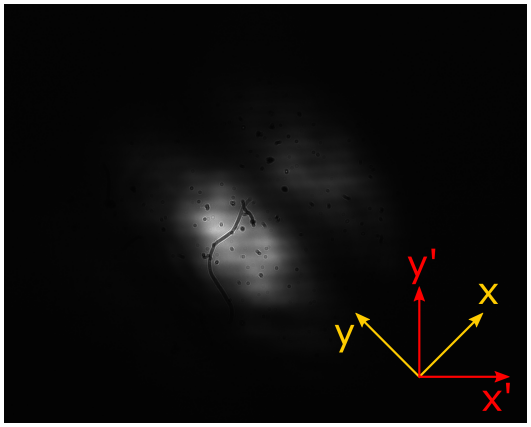

(b) Spot deflected in the position of a tweezer observed for a modulation at ν=250 kHz for a 1 mm beam waist.

Figure 5.10: Spot deflected in the position of a tweezer measured at different switching frequency values. The spot is initially symmetric for low switching frequencies but is distorted for high frequencies.

double well trap.

We quantified the deformation of both the ghosts and the standard tweezers by calculating the skewness of the distribution. The skewness is a measure of asymmetry of a probability distribution about its mean value, and can assume negative, positive or zero value [48]:

$$\tilde{\mu}_3 = \left\langle \left(\frac{X - \mu}{\sigma} \right)^3 \right\rangle \tag{5.5}$$

where X is the random variable considered with mean value μ and standard deviation σ and the brackets stand for the expectation value. The skewness is zero if the distribution is symmetric (for example a perfect Gaussian beam) and it is negative/positive if the left/right tail is longer than the opposite one. In particular, since we observe a diagonal distortion, we first rotate the image by 45 degrees clockwise and then evaluate the skewness. The plot in figure 5.11 shows the skewness evaluated for the marginal probability distributions along the horizontal (x) and vertical (y) axes in the rotated frame. At low ν the only asymmetric distribution is the horizontal direction of the ghost spot. Increasing the switching frequency, the vertical distributions remain unaffected, while the horizontal distribution of the tweezer spot becomes distorted for ν above 100 kHz. The skewness of the vertical distributions can be used as a reference to evaluate *how much* the distributions get warped.

A similar analysis has been carried out also for the smaller beam with 500 micron waist. In figure 5.12 we show the imaging of a tweezer and a ghost captured for 250 kHz switching frequency. Both the spots are distorted by the fast modulation, but the effect is less dramatic than in the case of the 1 mm beam waist, even though the potential is modulated at high switching frequency. The

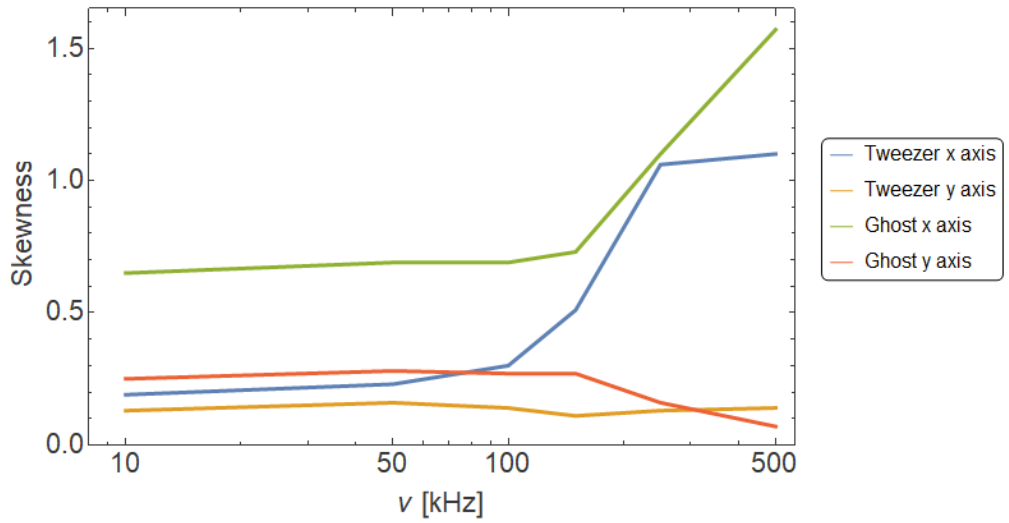

Figure 5.11: Skewnesses calculated for the vertical and horizontal distributions both for the ghost and the tweezer spots.

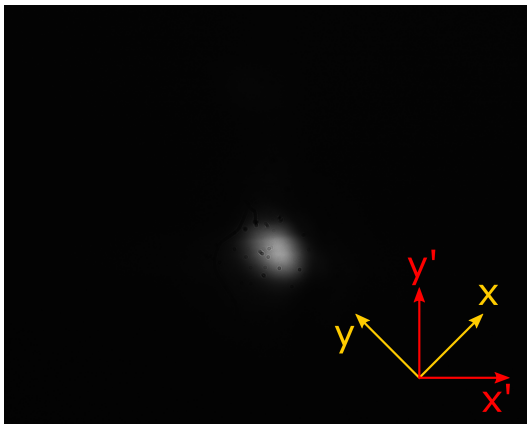

(a) Tweezer observed for a modulation at ν=250 kHz for a 500 μm beam waist.

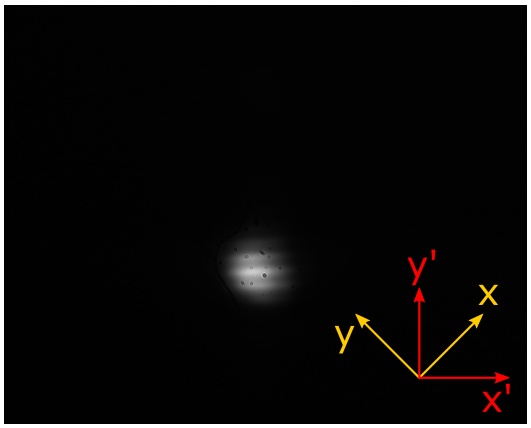

(b) Ghost observed for a modulation at ν=250 kHz for a 500 μm beam waist.

Figure 5.12: Tweezer and ghost spots measured at 250 kHz switching frequency. The spots are slightly warped.

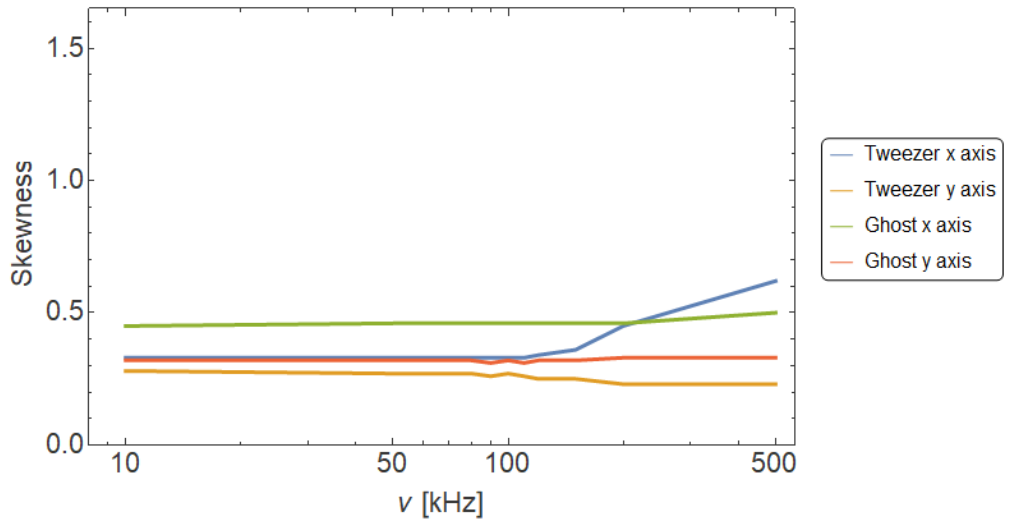

Figure 5.13: Skewnesses calculated for the vertical and horizontal distributions both for the ghost and the tweezer spots for the smaller beam waist (500 μm).

skewnesses of the probability distributions are calculated in this case as well, and they are plotted in figure 5.13. In this case we see that the skewness for the ghost spot is slightly higher than the tweezer's one, but the same value is maintained for all the ν range. The tweezer, instead, increases its asymmetry as the switching frequency increases. Anyway, the skewness values in the case of the 0.5 mm beam are smaller than the ones evaluated in the previous case. Hence, exploiting a smaller beam waist for the time-averaged potential technique seems to offer better conditions with respect to the 1 mm beam.

To conclude the description of the ghost spots we want to understand if atoms in the Magneto Optical Trap can be trapped in such a spot. In order to do that, we simulated the classical motion equations of a Strontium atom under the effect of gravity and a trapping potential that is time modulated, similarly to the simulations in subsection 3.2.2. The modulation of the potential implemented is an analytic function obtained as the product of two out of phase single-AOD modulations, following the model described above. Data are plotted in logarithmic color plots, like in the simulations of the trapping of atoms in the conventional tweezers. In particular, in figure 5.14 the simulations regarding an atom with initial velocity $v_0 = 0$ m/s and displacement with respect to the center of the tweezer δ=0 m are reported. In figure 5.14a we show the results of the simulations in the case of a 1 mm beam waist and hence a rise time $\tau \simeq 2.5$ μs, while in figure 5.14b the 500 μm case is presented. We report here again the results of the simulations performed in chapter 3 in the case of a real tweezer spot to simplify the comparison, in the case of an atom at rest for both the large (1 mm) and small (0.5 mm) beam sizes. It is useful to compare the figures 5.14 and 5.15 pairwise. The figures on the left are relative to the solutions of the simulations carried out in the case of the 1 mm beam waist, while the ones on the right are relative to the small beam (0.5 mm). Since the ghost spots are not symmetrical and are not suitable for trapping the atoms, the goal of the comparison is to identify a region of para-

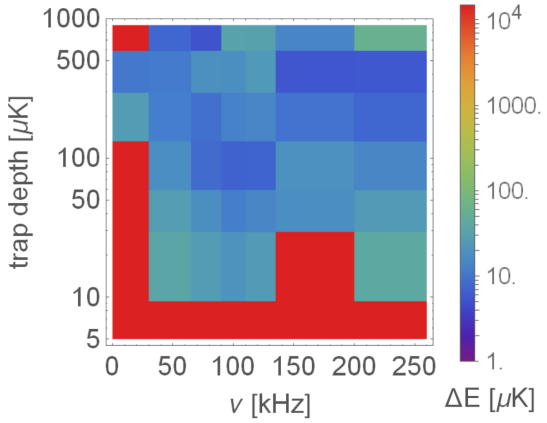

(a) Energy increase map as a function of the trap depth and the switching frequency. The energy values are converted in temperature (μK).

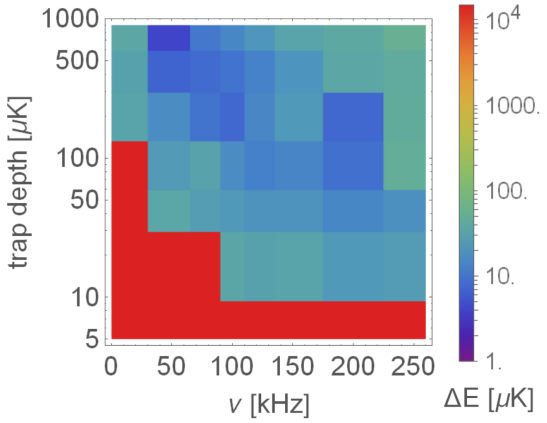

(b) Energy increase map as a function of the trap depth and the switching frequency. The energy values are converted in temperature (μK).

Figure 5.14: Simulations of the trapping of an atom at rest in a **ghost spot** generated by the time-averaged dynamics, using $v_0 = 0$ m/s and δ=0 m as starting conditions for the atom. The simulation is performed considering both 1 and 0.5 mm waists at the position of the AOD.

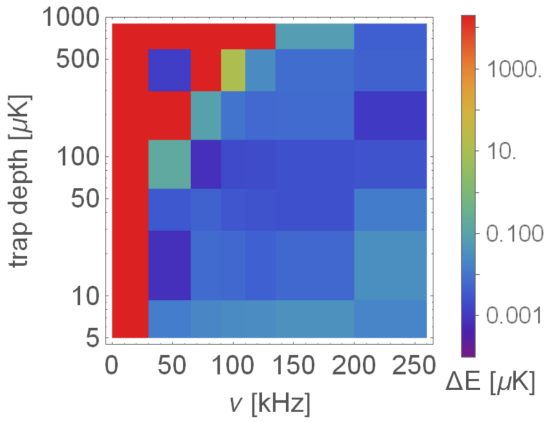

(a) Energy increase map as a function of the trap depth and the switching frequency. The energy values are converted in temperature (μK).

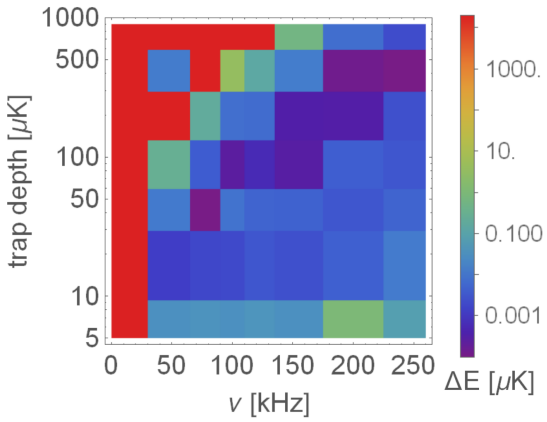

(b) Energy increase map as a function of the trap depth and the switching frequency. The energy values are converted in temperature (μK).

Figure 5.15: Simulations of the trapping of an atom at rest in a **real tweezer spot** generated by the time-averaged dynamics, using $v_0 = 0$ m/s and δ=0 m as starting conditions for the atom. The simulation is performed considering both 1 and 0.5 mm waists at the position of the AOD.

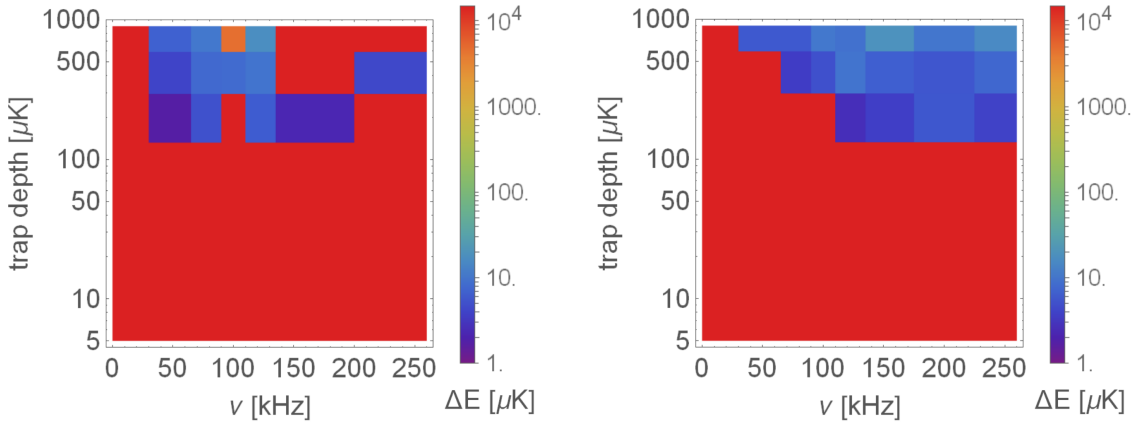

(a) Energy increase map as a function of the trap depth and the switching frequency. The energy values are converted in temperature (μK).

(b) Energy increase map as a function of the trap depth and the switching frequency. The energy values are converted in temperature (μK).

Figure 5.16: Simulations of the trapping of an atom at rest in a **ghost spot** generated by the time-averaged dynamics, using $v_0 = 0.03$ m/s and $\delta = 0.5 * w_T$ as starting conditions for the atom. The simulation is performed considering both 1 and 0.5 mm waists at the position of the AOD.

meters in which the ghost spot loses the atom while the real tweezer traps it. In both the cases we see that for high trap depths the atom is trapped equivalently in the real tweezer spot (figure 5.15) and in the ghost spot (figure 5.14). For low trap depths, below 10 μK, instead, the real tweezer is more efficient and traps the atom for all the switching frequencies above 50 kHz, while the ghost spot always loses the atom. This comparison suggests that the time-averaged technique can be exploited for low power depths only if we want to neglect the presence of the ghost spots. Anyway, it is important to observe that the simulations reported above take into account uniform modulations of the symmetric Gaussian trapping potential and the asymmetry of the ghost spots are not considered here. It is possible that implementing in the simulations a beam with strong asymmetries, especially for the ghost spot that is distorted for all the switching frequency values, the trapping efficiency is reduced. In that case the region of parameters suitable for the time-averaged potential technique would be larger.

We consider now the simulations performed for different initial conditions for the atom, in order to verify if the region of experimental parameters for which the real tweezers trap the atoms while the ghost spots lose them is a universal set or not. The situation is quite different when we consider an atom with $v_0 = 0.03$ m/s and $\delta = 0.5 * w_T$ that is the situation analogous to that discussed in subsection 3.2.2. We recall here, in figure 5.17 the plots from chapter 3 to give a direct comparison with figure 5.16. Also in this case, the real tweezer can be trapped in a region of parameters that extends to trap depths lower than the trapping in the ghost spots. For many switching frequency values the real tweezer traps the atoms for trap depths above 40 μK, while the ghosts require trap depths higher than 100 μK, both for the large beam (plots on the left) and small beam (plots on

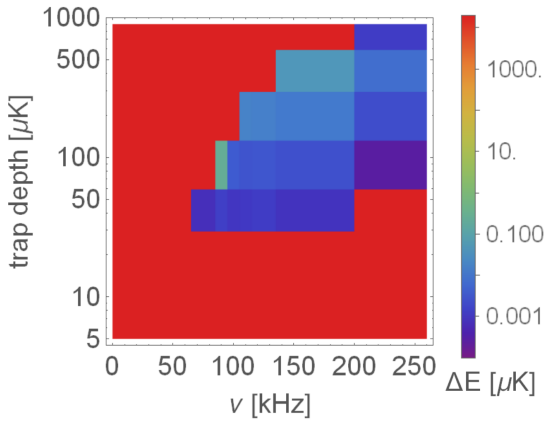

(a) Energy increase map as a function of the trap depth and the switching frequency. The energy values are converted in temperature (μK).

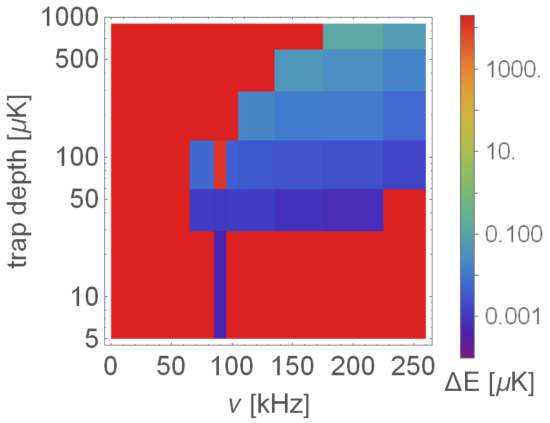

(b) Energy increase map as a function of the trap depth and the switching frequency. The energy values are converted in temperature (μK).

Figure 5.17: Simulations of the trapping of an atom at rest in a **real tweezer spot** generated by the time-averaged dynamics, using $v_0 = 0.03$ m/s and $\delta = 0.5 * w_T$ as starting conditions for the atom. The simulation is performed considering both 1 and 0.5 mm waists at the position of the AOD.

the right). The problem is that, except for one single combination of parameters for the small beam (U~5 μK, ν=90 kHz) the region of suitable parameters in this case, considering an atom with nonzero initial energy, is not compatible with the region of parameters suitable for the time-averaged technique. This means that the choice of a specific combination of trap depth and switching frequency selects a class of atoms that have a certain initial energy, both potential and kinetic. For example, choosing a trap depth U=5 μK would allow us to trap the atoms in the real tweezer and not in the ghost, but only the coldest ones in the thermal distribution. On the other hand, a 50 μK trap depth would allow for the trapping in the tweezers of hotter atoms too, but in turn it would enable the ghost spots to trap a few cold atoms too. In order to understand the possible range of applicability of the time-averaged method, the simulations have to explore further the phase space of the atoms of the MOT thermal distribution.

To conclude, the advantage of the time-averaged potential technique is the capability to generate and rearrange an arbitrary geometry array. On the other hand, the presence of ghost spots, distorted traps that in general cannot be exploited for trapping the atoms, limit the range of suitable power depths to very low values, below 10 μK. Moreover, the time-averaged potential can support only a few spots, due to the time constraints on the period of the switching, hence only small arrays can be produced. In case a large array is considered, the simulations of the transport of an atom performed in chapter 3 showed that high power depths are preferable, because the atoms are less affected by the motion. Hence, the range of trap depths suitable for the time-averaged potential is opposite to that of the transport of atoms, making it difficult to implement both on the same apparatus. One possibility is to design an apparatus with two different

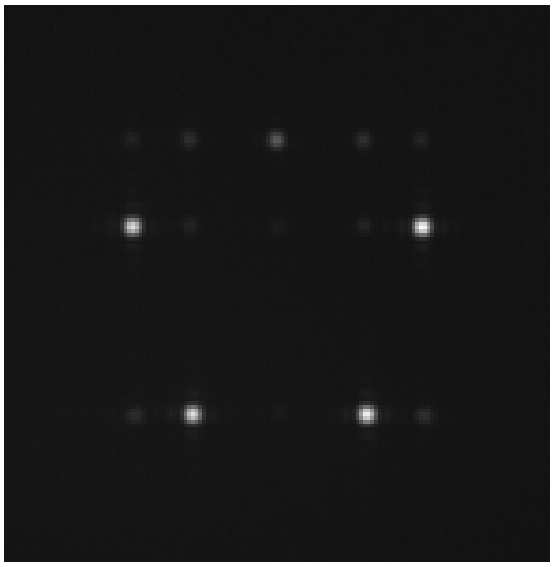

(a) A pentagonal pattern created by a 33% duty cycle waveform generated by an AWG.

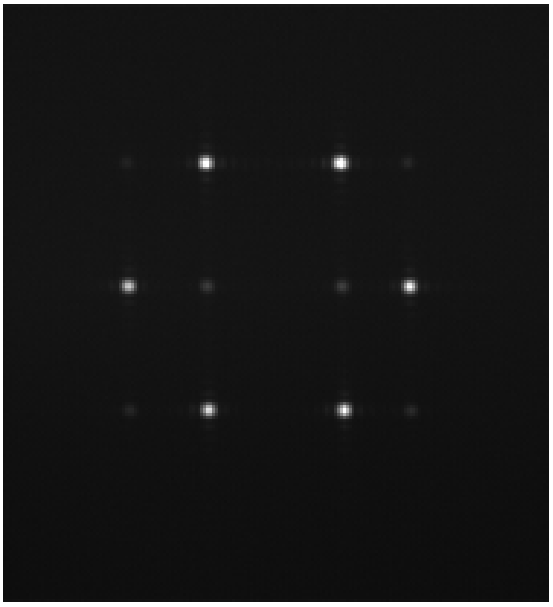

(b) A hexagonal pattern created by a 33% duty cycle waveform generated by an AWG.

Figure 5.18: Realization of elaborated arbitrary geometry patterns exploiting the time-averaged technique.

optical paths, one devoted to the rearrangement of the array for which the size of the beam waist is as large as possible, and a second dedicated to time-averaged techniques that can be leveraged for fast operations on the array.

5.2.2 Time-averaged generated arbitrary patterns

In the following paragraphs we show a couple of applications of a time-averaged potential technique for the creation of an arbitrary geometry pattern. As discussed in chapters 3 and 5, this technique presents many constraints, mainly regarding the timescale over which the beam deflected by the AODs completes one period of the time-averaging over all the positions of the array. We know from the performed simulations that a typical switching frequency that allows for the trapping of atoms in conventional time-averaged tweezers is $\nu \sim$100 kHz, that means a period of approximately 10 μs. Hence, we realized pentagonal and hexagonal patterns using a time-averaged potential modulated at 100 kHz. The second constraint regards the duty cycle of the period: we saw in the simulations in figures 3.14a 3.14b that increasing the number of subperiods it is still possible to trap the atoms but the accessible region of suitable parameters is reduced. In particular, leveraging a tweezer with power depth equal to 1 mW, it is possible to create time averaged patterns even switching each channel among three different RF frequencies for ν=100 kHz. We then realized a pentagonal pattern and a hexagonal one making use of an elaborated time-averaged potential, as shown in figures 5.18a and 5.18b, respectively. Instead of generating the whole array with a single deflected beam that is periodically deflected over all the desired spots,

we decompose the plane figures into rows in order to minimize the number of switches. One AOD is used to run periodically over the rows, switching between sinusoidal RF frequencies. The other AOD, instead, is switched between multi-frequency tones, having the number of frequency components equal to the number of spots in each specific row. For the pentagon, for example, in the first third of the period the vertical AOD identifies the lower row, while the horizontal one produces two different beams. During the second part of the period, the second line is produced. Finally, the vertical AOD switches to the top row and the horizontal AOD produces one single spot at the pentagon vertex. A similar procedure is followed for the creation of the hexagonal pattern too. The plane figures have to be parametrized in Cartesian coordinates, then the spatial coordinates are converted into frequency coordinates that are the RF frequency components that the AWG is fed with.

In both the patterns in figures 5.18a and 5.18b the ghost spots are visible in a situation more complicated than the simple pair of spots for which the ghosts were described in the previous paragraphs. In an elaborated pattern the ghosts arise for every combination of frequencies that change from one part of the waveform's period to the next one. Despite the presence of the ghost spots, in both the patterns the amplitude of the real tweezers is almost uniform over the whole array.

Conclusions

In this thesis I carried out an extensive study of the techniques for the generation of arrays of optical tweezers exploiting a pair of acousto-optic deflectors. In the first part of the thesis I presented the results I obtained for two set of simulations of different AODs configurations. In the first set of simulations I studied the transport of an atom in a moving optical tweezer. In particular, I have shown that it is possible to minimize the energy increase of the atom with a proper choice of the function describing the motion of the tweezer in which the atom is trapped. Implementing this function in the simulations, we obtained that for most of the combinations of the experimental parameters considered, spanning both the trap depth U and the mean velocity of the transport v_{mean} in a wide range of values, the atom is heated by less than 10 μK. This is a good result since it is a value compatible with the typical tweezers trap depths.

In the second set of simulations I explored the possibility of exploiting a time-averaged potential technique for the generation of arbitrary-geometry arrays of optical tweezers. The free parameters of the simulation are in this case the trap depth of the tweezer U and the frequency ν at which the time-dependent trapping potential is periodically moved over all the spots of the array. The simulations prove that with this technique it is possible to trap the atoms over a wide range of U and ν in case the tweezer is switched over two or three different positions. A higher number of positions leads to a loss of atoms from the tweezer, thus the application of this technique is limited to small-size arrays.

In chapter 4 I tested the static and dynamic properties of a pair of acousto-optic deflectors in order to understand if the requirements resulting from the simulations in chapter 3 can be satisfied by the tested devices. I characterized the efficiency of the two devices as a function of RF driving frequency and amplitude for different alignment conditions, and found a strong dependence on the efficiency curves on the alignment. I then studied the efficiency of a pair of coupled AODs in crossed configuration. I implemented a method for a rapid characterization of a 2D efficiency map of the crossed AODs and tested its validity by comparing it with a set of individual efficiency measurements. In the context of the dynamic characterization of the AODs, I studied the response time of the device subjected to a fast switching RF driving signal, pointing out the dependence on the size of the laser beam inside the AOD.

Chapter 5 is dedicated to the generation of arrays of optical tweezers. After having verified the magnification properties of the imaging setup by using simple linear arrays, I implemented a simple time-averaged array consisting in two sites

in diagonal configuration. The technique produces a set of additional spots that we call *ghost spots* or simply *ghosts* that are consequence of transient effects taking place during the switching between a pair of different frequencies in the RF signal. I carried out additional simulations to determine the range of U and ν parameters over which the ghost spots are capable to trap the atoms and compared it to the results obtained in chapter 3 for an "ordinary" time-averaged optical tweezer. The results are not promising, as there are only small regions of parameters over which the atoms are trapped in the ordinary spots and are unaffected by ghost spots and there is a strong dependence on the initial conditions of the atomic motion. For this reason, the time-averaged technique needs a further investigation, spanning several different combination of parameters in the phase space of the problem, to find out if a universal set of parameters can be found to produce an efficient trapping in the tweezer spots while losing the atoms in the *ghosts*.

The characterizations and predictions obtained in this thesis about the generation and manipulation of optical tweezers for trapping Strontium atoms will be important in the experimental realization of the system. In particular, I verified that the features of the pair of AODs are suitable for the direct implementation of 1D and 2D optical tweezer arrays. Moreover, the results of the simulations from chapter 3 represent a good starting point for the implementation of rearrangement procedures, that will be important especially when considering large tweezers arrays generated via other kind of devices (e.g. Spatial Light Modulators). For small-sized arrays, instead, the time-averaged trapping technique could offer the possibility to generate and rearrange the array of optical tweezers using a pair of AODs. This technique will be tested on the atomic sample directly in order to verify its range of applicability.

Bibliography

[1] Richard P Feynman. Simulating physics with computers. *International journal of theoretical physics*, 21(6/7):467–488, 1982.

[2] Iulia Buluta and Franco Nori. Quantum simulators. *Science*, 326(5949):108–111, 2009.

[3] Ehud Altman. Quantum simulators: Architectures and opportunities. *PRX Quantum*, 2(017003), 2021.

[4] I. Bloch. Ultracold quantum gases in optical lattices. *Nature Physics*, 1:23–30, 2005.

[5] Christian Gross and Immanuel Bloch. Quantum simulations with ultracold atoms in optical lattices. *Science*, 357(6355):995–1001, 2017.

[6] Roos C. Blatt, R. Quantum simulation with trapped ions. *Nature Physics*, 8:277–284, 2012.

[7] J. I. Cirac and P. Zoller. Quantum computations with cold trapped ions. *Phys. Rev. Lett.*, 74:4091–4094, May 1995.

[8] Markus Greiner, Olaf Mandel, Tilman Esslinger, Theodor W Hänsch, and Immanuel Bloch. Quantum phase transition from a superfluid to a mott insulator in a gas of ultracold atoms. *Nature*, 415(6867):39–44, 2002.

[9] Giacomo Roati, Chiara D/'Errico, Leonardo Fallani, Marco Fattori, Chiara Fort, Matteo Zaccanti, Giovanni Modugno, Michele Modugno, and Massimo Inguscio. Anderson localization of a non-interacting Bose-Einstein condensate. *Nature*, 453(7197):895–898, June 2008.

[10] J. K. Chin, D. E. Miller, Y. Liu, C. Stan, W. Setiawan, C. Sanner, K. Xu, and W. Ketterle. Evidence for superfluidity of ultracold fermions in an optical lattice. *Nature*, 443(7114):961–964, Oct 2006.

[11] Joseph W. Britton, Brian C. Sawyer, Adam C. Keith, C.-C. Joseph Wang, James K. Freericks, Hermann Uys, Michael J. Biercuk, and John J. Bollinger. Engineered two-dimensional ising interactions in a trapped-ion quantum simulator with hundreds of spins. *Nature*, 484(7395):489–492, Apr 2012.

[12] J. Zhang, G. Pagano, P. W. Hess, A. Kyprianidis, P. Becker, H. Kaplan, A. V. Gorshkov, Z.-X. Gong, and C. Monroe. Observation of a many-body dynamical phase transition with a 53-qubit quantum simulator. *Nature*, 551(7682):601–604, Nov 2017.

[13] A. Fuhrmanek, R. Bourgain, Y. R. P. Sortais, and A. Browaeys. Light-assisted collisions between a few cold atoms in a microscopic dipole trap. *Phys. Rev. A*, 85:062708, Jun 2012.

[14] Brian J. Lester, Niclas Luick, Adam M. Kaufman, Collin M. Reynolds, and Cindy A. Regal. Rapid production of uniformly filled arrays of neutral atoms. *Phys. Rev. Lett.*, 115:073003, Aug 2015.

[15] Manuel Endres et al. Atom-by-atom assembly of defect-free one-dimensional cold atom arrays. *Science*, 354(6315):1024–1027, 2016.

[16] Daniel Barredo et al. An atom-by-atom assembler of defect-free arbitrary two-dimensional atomic arrays. *Science*, 354(6315):1021–1023, 2016.

[17] Wang T.T. Levine H. et al. Ebadi, S. Quantum phases of matter on a 256-atom programmable quantum simulator. *Nature Physics*, 595:227–232, 2021.

[18] Schuler M. Williams H.J. et al. Scholl, P. Quantum simulation of 2d antiferromagnets with hundreds of rydberg atoms. *Nature Physics*, 595:233–238, 2021.

[19] Alexandre Cooper, Jacob P. Covey, Ivaylo S. Madjarov, Sergey G. Porsev, Marianna S. Safronova, and Manuel Endres. Alkaline-earth atoms in optical tweezers. *Phys. Rev. X*, 8:041055, Dec 2018.

[20] Y. Bao S. Burchesky W. Ketterle Kang-Kuen Ni J. M. Doyle L. Anderegg, L. W. Cheuk. An optical tweezer array of ultracold molecules. *Science*, 365(6458):1156–1158, 2019.

[21] Eckner W.J. Milner W.R. et al. Young, A.W. Half-minute-scale atomic coherence and high relative stability in a tweezer clock. *Nature*, 588:408–413, 2020.

[22] Koki Ono, Jun Kobayashi, Yoshiki Amano, Koji Sato, and Yoshiro Takahashi. Antiferromagnetic interorbital spin-exchange interaction of yb171. *Physical Review A*, 99(3), Mar 2019.

[23] Antoine Browaeys and Thierry Lahaye. Many-body physics with individually controlled rydberg atoms. *Nature Physics*, 16(2):132–142, Jan 2020.

[24] L. Béguin, A. Vernier, R. Chicireanu, T. Lahaye, and A. Browaeys. Direct measurement of the van der waals interaction between two rydberg atoms. *Physical Review Letters*, 110(26), Jun 2013.

[25] Harry Levine, Alexander Keesling, Giulia Semeghini, Ahmed Omran, Tout T. Wang, Sepehr Ebadi, Hannes Bernien, Markus Greiner, Vladan Vuletic, Hannes Pichler, and Mikhail D. Lukin. Parallel implementation of high-fidelity multiqubit gates with neutral atoms. *Phys. Rev. Lett.*, 123:170503, Oct 2019.

[26] L.I.R. Gil, R. Mukherjee, E.M. Bridge, M.P.A. Jones, and T. Pohl. Spin squeezing in a rydberg lattice clock. *Physical Review Letters*, 112(10), Mar 2014.

[27] Matthew A. Norcia, Aaron W. Young, William J. Eckner, Eric Oelker, Jun Ye, and Adam M. Kaufman. Seconds-scale coherence on an optical clock transition in a tweezer array. *Science*, 366(6461):93–97, Sep 2019.

[28] P. M. Chaikin and T. C. Lubensky. *Principles of Condensed Matter Physics*. Cambridge University Press, Cambridge, 1995.

[29] S. Blundell. *Magnetism in Condensed Matter*. Oxford Master Series in Condensed Matter Physics. OUP Oxford, 2001.

[30] F. Robicheaux and J. V. Hernandez. Many-body wave function in a dipole blockade configuration. *Phys. Rev. A*, 72:063403, Dec 2005.

[31] H. Bernien et al. Probing many-body dynamics on a 51-atom quantum simulator. *Nature*, 551(7682):579–584, Nov 2017.

[32] M. Morgado and S. Whitlock. Quantum simulation and computing with rydberg-interacting qubits. *AVS Quantum Science*, 3(2):023501, Jun 2021.

[33] Jack Wilson, Samuel Saskin, Yijian Meng, Shuo Ma, Rohit Dilip, Alex Burgers, and Jeff Thompson. Trapped arrays of alkaline earth rydberg atoms in optical tweezers, 2019.

[34] Aaron W. Young, William J. Eckner, William R. Milner, Dhruv Kedar, Matthew A. Norcia, Eric Oelker, Nathan Schine, Jun Ye, and Adam M. Kaufman. Half-minute-scale atomic coherence and high relative stability in a tweezer clock. *Nature*, 588(7838):408–413, Dec 2020.

[35] Ivaylo S. Madjarov, Alexandre Cooper, Adam L. Shaw, Jacob P. Covey, Vladimir Schkolnik, Tai Hyun Yoon, Jason R. Williams, and Manuel Endres. An atomic-array optical clock with single-atom readout. *Physical Review X*, 9(4), Dec 2019.

[36] Ivaylo Madjarov. *Entangling, controlling, and detecting individual strontium atoms in optical tweezer arrays*. PhD thesis, California Institute of Technology, Pasadena, California, 2021.

[37] Harold J. Metcalf and Peter van der Straten. *Laser Cooling and Trapping*. Springer-Verlag, New York, 1999.

[38] D.A. Steck. *Quantum and Atom Optics*. 2007.

[39] O. Svelto. *Principles of Lasers*. Springer US, 2010.

[40] M. Born, E. Wolf, et al. *Principles of Optics: Electromagnetic Theory of Propagation, Interference and Diffraction of Light*. Cambridge University Press, 1999.

[41] Yenny Natali Martinez. Studies of the 5s2 1s0 - 5s5p 3p1 transition in atomic strontium, 2008.

[42] V. Martikyan, D. Guéry-Odelin, and D. Sugny. Comparison between optimal control and shortcut to adiabaticity protocols in a linear control system. *Physical Review A*, 101(1), Jan 2020.

[43] Yongcheng Ding, Tang-You Huang, Koushik Paul, Minjia Hao, and Xi Chen. Smooth bang-bang shortcuts to adiabaticity for atomic transport in a moving harmonic trap. *Physical Review A*, 101(6), Jun 2020.

[44] J.J. Sakurai and J. Napolitano. *Modern Quantum Mechanics*. Cambridge University Press, 2017.

[45] Dennis R. Pape Akis P. Gouzoulis. *Design and fabrication of Acousto-Optic devices*. Marcel Dekker, New York, 1994.

[46] AA Opto-Electronic. Application Notes [Online]. http://www.aaoptoelectronic.com/wp-content/uploads/documents/AA-THEORY-NOTES.pdf.

[47] G. Cowan. *Statistical data analysis*. Oxford University Press, USA, 1998.

[48] J.F. Kenney. *Mathematics of Statistics*. Number v. 2 in Mathematics of Statistics. Van Nostrand, 1946.